Study on Analytical Modeling of Antenna Arrays for Implementation of Efficient Design Procedure

May   2000

Hiroaki Miyashita

Acknowledgments

i

Abstract

The scope of the present study is implementation of efficient design procedure in practical applications of the antenna array for communications and radar systems. Throughout the study, the analytical modeling of hardware is investigated for developments of newly proposed antennas, analysis of the feeding structure, and the mutual coupling problems.

The first objective is a proposal of a new type of collinear antenna array called the electromagnetically coupled coaxial dipole array antenna. The key feature of the antenna is a novel use of an electromagnetically coupled feed for the radiating element. The structural simplicity of the new antenna overcomes difficulty in manufacturing of conventional antenna. Analyses of the input impedance and the radiation pattern, and a method of matching are described in detail, where simple useful formulas developed help design procedure. Fabrication and measurement of a prototype array antenna support the theory.

The second objective is implementation of analytical modeling of parallel plate region with an application to the circular iris. Any analysis of the circular iris has not been reported so far, and the present study attacks the problem for the first time. A simple approximately closed form formula is obtained for the equivalent susceptance. The effect of the curvature of the circular iris appears to be a correction factor to the previously known expression of the linear iris. The correction factor goes to unity if the radius of the curvature is very large compared with the operating wavelength. Verification of the approximate formula is given through comparison with numerical solution by an exact integral equation formalism.

The third objective is a proposal of the radial line planar monopulse antenna. The key feature of the antenna is use of multiple port feed of a radial line and it gives a new function of synthesizing monopulse patterns which was not achieved by related conventional antennas. By an analysis of the mutual coupling between probes in the radial line with simple resultant expression of formulas, the mechanism of monopulse pattern synthesis is

made clear. A design procedures are developed for the uniform aperture field distribution, where fabrication and measurement of a prototype antenna support the design procedure.

The fourth objective is to develop a method to analyze antenna couplings between arrays on a polyhedron structure. The present study attacks the problem for the first time. To compute efficiently a large number of pairs of the radiating elements, an approximately closed form formula is developed for the mutual admittance between microstrip antennas separated by a wedge with the aid of the geometrical theory of diffraction. Experimental verification of the theory is given. Through several numerical simulations, it is concluded that sidelobe level of the antenna array in the direction of the wedge gives significant contribution to the coupling. Therefore, null beam forming or low sidelobe operation in that direction is applicable to obtaining good isolation characteristics.

The fifth objective is to develop a general scheme for the analysis of the mutual coupling between radiating elements. The new feature of the study is unification of the previously known Fresnel approximation of mutual impedance and admittance integrals into simple and general forms including its extension to the high frequency geometries for the first time. The expression allows a physical interpretation as a product of radiation patterns multiplied by a propagator of the environment and divided by the voltages or the currents at the feeding points of the two antennas, and gives an approximate first order universal relationship between antennas of arbitrary shape placed in the far field. For the application of the theory, two cases of microstrip antennas on a ground plane and on a polyhedron structure are given with experimental verification.

The hardware and methods developed in the present study are considered to have wide applicability for communications and radar systems.

Contents

List of Figures

Chapter 1

Introduction

1.1   Background of study

The antenna array is composed of plural number of radiating elements with feeding structures. Each radiating element is excited simultaneously by appropriate amplitude and phase so as to synthesize desired radiation patterns. At the initial stage of the design for a particular application, the radiation characteristics are readily predicted by using the array factor argument [1]. However, for realization of the hardware, implementation of design procedure is needed based on the knowledge of electromagnetics. The procedure has several stages of analysis as follows:

- the radiating element,

- the feeding structure,

- the mutual coupling between radiating elements, and

- the farm scattering.

As the hardware has a large number of parameters to be determined, identification of dominant parameters is important with the aid of physical insight. Analytical modeling is suited for the purpose because the characteristics of antennas are described by the

solution of the Maxwell's equations. If a simple analytical modeling is achieved with explicit mathematical relation between the parameters, it can be a source of efficient design procedure because the relation gives a guideline for optimization of parameters. Even if one desires more accurate results through numerical or experimental means, the relation acts as a powerful tool to minimize the time-consuming efforts. In the following, a summary of each stage of the analysis is given with representative methods of the simple analytical modeling.

The analysis of the radiating element determines the input impedance and the radiation pattern for a single element. The analytical modeling is focused on treatment of the radiating element as a set of equivalent currents of simple forms [2][3]. The ElectroMotive Force (EMF) method [4][5] has wide class of applicability. The equivalent currents are determined by empirical or theoretical means. For example, a half wavelength dipole is modeled by a sinusoidal electric current. In this case, the empirical argument may be applicable to choose the shape of the current. To accommodate the modeling with some theoretical foundation, the Kirchhoff approximation [2][3] for aperture fields is often used. Modeling of waveguide horn antenna [1] is an example. The aperture fields are approximated by incident wave from the feed waveguide. The vector products between the aperture fields and the normal vector of the aperture surface give the electric and magnetic equivalent currents. A related example is the cavity model [6] of the MicroStrip Antenna (MSA) [7], where the antenna is modeled by the equivalent magnetic currents at the edge. After the equivalent currents are determined, the radiation field is calculated by using the radiation integral. The far field approximation [2][5] of the integral gives the radiation pattern. The complex radiation power including reactive contribution is calculated by surface integrals with the observation points of the radiation integral chosen at the surface of the equivalent currents. The input impedance is calculated by division of the complex radiation power by absolute square of amplitude of current at the feeding

port of the antenna.

The analysis of feeding structure is carried out to obtain desired excitation distribution of the antenna array. If each radiating element is attached directly to an active module by using a single feeding line, neglect of detailed analysis is possible for the feeding structure. The approximation is widely used and adequately applicable to the active phased array antenna [8]. On the other hand, appropriate modeling and analysis are needed in the case that plural radiating elements are excited by passive Beam Forming Networks (BFN) which govern the excitation distribution. The network formalism [2][3][9] in microwave theory is applicable. The modeling is achieved by use of the equivalent circuit, where each discontinuity in guiding structure is treated by appropriate introduction of local parameters of the circuit. The array excitation distribution is obtained from amplitude and phase at the port of the circuit where the radiating element is attached. Precise modeling is possible if the circuit parameter is supported by the solution of the boundary value problem [3]. For example, consider the waveguide slot array antenna [10]. The equivalent circuit is described as series connection of shunt admittance of each slot. A variational expression [11] is obtained by using an integral equation with respect to equivalent currents on the surface of the slot. Use of a sinusoidal current as the trial function gives simple expression of the shunt admittance.

The analysis of the Mutual Coupling Between the Radiating Elements (MCBRE) determines actual performance of the antenna array under operation. MCBRA sometimes gives significant degradation of performance such as ripple in active element pattern, large variation of active impedance during the scanning of the beam, ...etc. Two approaches are known for the analysis: the Finite Array Approach (FAA) – or Element by Element Approach (EEA) – and the Infinite Array Approach (IAA) [1][8][12]. FAA treats the antenna array as finite set of radiating elements. Each feeding point of the radiating element is modeled by a port of a circuit with impedance matrix of the antenna array [1].

The interaction is treated element by element through the mutual impedance between the ports. The EMF method is a representative example, where the mutual impedance is calculated in an analogous way of the self impedance. On the other hand, IAA positively utilizes the periodic structure of the antenna array. If the total number of radiating elements is very large, each radiating element is treated as if it is located in an infinite periodic structure. Application of the Floquet theorem [3] reduces the problem to the case of a single radiating element. All the effects including MCBRE in infinite array environment are automatically contained in the Floquet mode expansion of the fields. The active element pattern and active impedance are calculated from the active reflection coefficient [1][12] obtained by the theory. The EMF method is also applicable [13] for IAA by applying the equivalent currents as the source of the periodic Green's function.

The analysis of the farm scattering determines the performance of the antenna array under the presence of platform. If the field of view of the antenna is limited or nearby structure is complicated, reflected and diffracted waves from the farm cause degradation in the radiation pattern and impedance characteristics. In addition, if the system requires multifunction-operation such as simultaneous use of different antennas on the same platform, amount of interference must be analyzed between them under the presence of the farm. The Geometrical Theory of Diffraction (GTD) [14][15] is adequately applicable to the class of problems. GTD is an extension of Geometrical Optics (GO), where the direct and reflected waves are treated as those of GO and the diffracted waves from canonical geometries such as the edge, the cylinder, ... etc. are expressed by simple analytical formulas. Approximate modeling of the farm with combination of the canonical geometries [16] accommodates the use of GTD. To analyze the radiation pattern of the antenna array on the farm, each contribution of the farm scattering is treated by GTD ray tracing for each radiating element. GTD can be applied to the interference problem beyond the scheme of GO where no GO ray exits between the two antennas. For example, con-

sider two antennas separated by a thin fence. The interference is due to diffracted waves from the fence or equivalently the edge in the scheme of GTD. The mutual impedance is calculated by combination of the EMF method and the edge diffraction formula of GTD.

To obtain simple analytical formulas for physical quantities, where closed form expressions are preferable, the following techniques are applicable:

- neglect of higher order terms for rapidly convergent infinite series,

- use of sum formulas for infinite series,

- analytical evaluation of integrals through appropriate choice of the equivalent current in the integrand,

- application of far field or asymptotic approximation of integrals, and

- development of variational expression and appropriate choice of the trial function,

where each approximation is supported by identification of small or large parameters compared with specific scales of the system for perturbation argument. As a result, dominant terms can be extracted for implementation of efficient design procedure.

1.2   Scope of study and organization of chapters

The scope of the present study is implementation of efficient design procedure in practical applications of the antenna array for communications and radar systems. Throughout the study, the analytical modeling of hardware is investigated in connection with each stage of the analysis described in the previous section with the following concrete goals:

- development of an efficient design procedure for newly proposed collinear antenna array: the electromagnetically coupled coaxial dipole array antenna in Chapter 2, where primary effort is made for modeling of the radiating element,

- implementation of analytical methods in the parallel plate region with their applications to the circular iris in Chapter 3 and newly proposed planar antenna array: the radial line planar monopulse antenna in Chapter 4, where modeling of feeding structure is attacked in detail, and

- development of simple analytical method for the analysis of mutual coupling between radiating elements with its application to antenna arrays on a polyhedron structure in Chaters 5 and 6, where modeling of the mutual coupling and the farm scattering is sought.

The study is described with the following organization.

In Chapter 2, a design procedure is developed for a newly proposed omnidirectional antenna array, the electromagnetically coupled coaxial dipole array antenna. The key feature of the antenna is a novel use of an electromagnetically coupled feed for the radiating element. The structural simplicity of the new antenna overcomes difficulty in manufacturing of conventional antenna. The chapter is organized below. First, an exact solution for the TEM mode reflection coefficient of semi infinite coaxial cable is analyzed by using the Wiener-Hopf technique. A simple approximately closed form expression is derived through application of sum formula for infinite sums and polynomial approximation for infinite integrals. Verification of the formula is given by comparing the numerical values with the exact solution. Second, the approximate formula is applied to calculate the self admittance of the radiating element. Third, the radiation pattern of the radiating element is analyzed by an integral equation formalism with analytical implementation of the Galerkin's method. Fourth, the feeding structure is modeled by an equivalent circuit. Explicit design procedure is described including a method of matching. Finally, fabrication and measurement are given for a prototype array antenna.

In Chapter 3, analytical formulations are developed for the parallel plate region with application to a circular iris in a parallel plate waveguide. Any analysis of the circular iris has not been reported so far, and the present study attacks the problem for the first time. First, by using modal analysis, variational expression of an equivalent susceptance is obtained for the circular iris when TEM mode cylindrical wave is incident from the center. By extending the Schwinger's analysis to the case of cylindrical harmonics expansions, a simple closed form formula is obtained. The formula recovers known expression for linear iris when the radius of the circular iris is very large compared with the operating wavelength. Second, alternative formulation is developed through an exact integral equation formalism by developing the Green's function of a circular current in the parallel plate waveguide. Finally, verification of the approximate formula is given by comparison of numerical values between the two formulations.

In Chapter 4, a design procedure is developed for a newly proposed planar antenna array, the radial line planar monopulse antenna, which is capable of monopulse tracking operations. The key feature of the antenna is use of multiple port feed of a radial line and it gives a new function of synthesizing monopulse patterns which has not been achieved by related conventional antennas. The chapter is organized below. First, the mutual coupling

of probes in a parallel plate waveguide is analyzed by the EMF method with a simple closed form result. Second, the analysis is applied to derive the condition for synthesis of monopulse patterns. Third, a design procedure is proposed for uniform aperture field distribution with algebraic relations between the parameters. Finally, fabrication and measurement for a prototype antenna is given for verification of the theory.

In Chapter 5, an analysis is carried out for antenna coupling between arrays on a polyhedron structure. The present study attacks the problem for the first time. First, by using the EMF method with approximate evaluation of integral, a simple closed formula is derived for the mutual admittance between circular MSAs separated a wedge. The diffracted fields are treated by using GTD. Second, numerical simulations are carried out for antenna coupling under beam steering of the antenna array with the formula. Finally, experimental verification of the theory is given.

In Chapter 6, a simple and general first order expression of mutual impedance and admittance is derived for arbitrary class of antennas modeled by equivalent currents. The new feature of the study is unification of the previously known Fresnel approximation of mutual impedance and admittance integrals into simple and general forms including its extension to the high frequency geometries for the first time. The chapter is organized below. First, the reaction integral between arbitrary sources is evaluated by using the far field approximation, where dyadic decompositions of the field quantities are introduced with respect to ray coordinates. The developed formulas are of the form, *a product of radiation patterns multiplied by a free space propagator and divided by the voltages or the currents at the feeding points of the two antennas.* Second, the theory is extended to the case of presence of wedges. Finally, applications for MSAs are given with experimental verifications.

In Chapter 7, summaries and conclusions are described.

Chapter 2

Electromagnetically Coupled Coaxial Dipole Array Antenna

2.1 Introduction

In this chapter, a design procedure is developed for a newly proposed collinear antenna array which has an omnidirectional pattern in the horizontal plane. Figure 2.1 shows the geometry of the antenna called the electromagnetically coupled coaxial dipole array antenna [17]. It has the Electromagnetically Coupled Coaxial Dipole (ECCD) as the radiating element which is composed of a half wavelength metallic circular pipe fed electromagnetically by an annular ring slot on the outer conductor of the feeding coaxial cable. The metallic circular pipes act as radiating dipoles and their collinear arrangement in the vertical direction with in-phase excitation gives an array performance.

There exist some kinds of collinear antennas. The COaxial COllinear antenna (COCO antenna) [18]-[21] employs a collinear arrangement of coaxial cables where the feeding structures are inverted in a half wavelength step so as to produce in phase excitations. Instead of using the coaxial cable, a printed COCO antenna with microstrip feed line is also reported [22]. An additional type is the Coaxial Dipole Antenna (CDA) [23]. The

radiating dipoles of CDA is fed by an annular ring slot which extends in radial direction from the outer conductor of the feeding coaxial cable. A modification of CDA is the bi-directional collinear antenna [24] which uses an arc parasitic plate attached near the radiating dipole of CDA.

ECCD array antenna, as proposed in this chapter, is another modification of CDA which has an advantage of structural simplicity due to a novel use of an electromagnetically coupled feed for CDA.

In Section 2.2, a Wiener-Hopf analysis [25]-[28] is carried out for the TEM mode reflection coefficient of a coaxial cable which has a semi-infinite outer conductor [29]-[31]. The analysis deals with an exact solution as well as a simple approximate formula which is valid if the radius of the coaxial cable is much smaller than the operating wavelength.

In Section 2.3, the methods by Chen and Keller [32], and Lee and Mittra [33] are applied to derive the input admittance of the radiating element.

In Section 2.4, an analysis of radiation pattern of ECCD is carried out with an integral equation formalism by using the Green's functions of a perfectly conducting circular cylinder.

In Section 2.5, an equivalent circuit for ECCD array is described.

In Section 2.6, fabrication and measurement of a prototype array antenna are described.

In Section 2.7, a summary of this chapter is given.
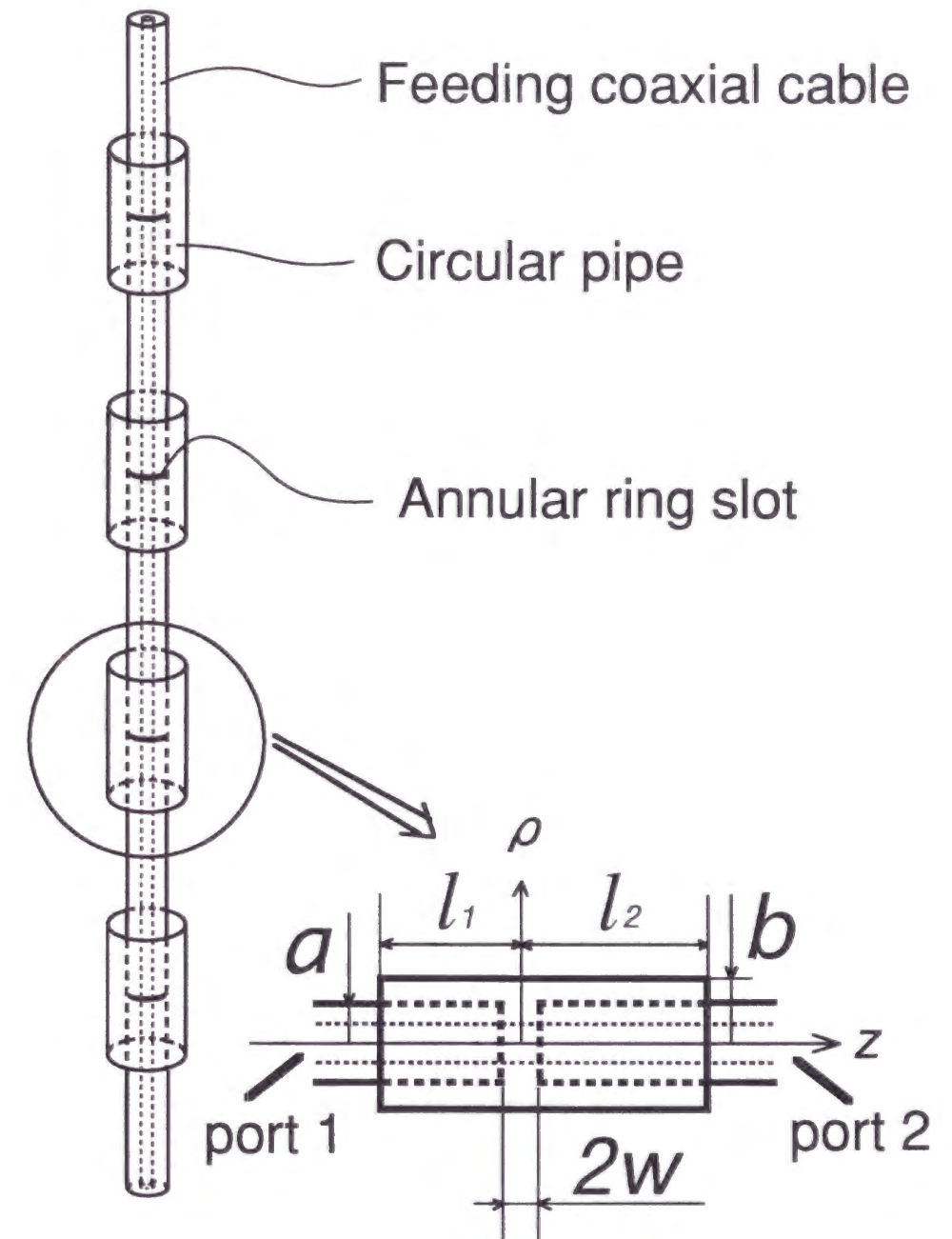
Figure 2.1: The electromagnetically coupled coaxial dipole array antenna.

2.2 TEM mode reflection coefficient for a semi-infinite coaxial cable

In this section, a Wiener-Hopf analysis is carried out for the TEM mode reflection coefficient of a semi-infinite coaxial cable, as shown in Fig.2.2, when the TEM mode is incident from inside the cable. The structure is one of the canonical Wiener-Hopf geometries. Classic results for the TEM mode incidence are given in [29], and the case of higher order mode incidence is treated in [31], where some approximate formulas are developed when the radius of the coaxial cable is much larger than the operating wavelength. In this section, we derive an exact analytical expression as well as a simple approximate formula which is valid when the radius of the coaxial cable is much smaller than the operating wavelength. From now on, $e^{-i\omega t}$ dependence is assumed for the fields.

The problem has a rotational symmetry in the ϕ direction, and functional dependence of every physical quantity appears in the analysis is of the form $f(\rho, z)$. We define a Fourier transform pair of f with respect to z as follows:

$$F(\rho, \alpha) = \frac{1}{(2\pi)^{1/2}} \int_{-\infty}^{\infty} f(\rho, z) e^{i\alpha z} dz, \tag{2.1}$$

$$f(\rho, z) = \frac{1}{(2\pi)^{1/2}} \int_{-\infty}^{\infty} F(\rho, \alpha) e^{-i\alpha z} d\alpha. \tag{2.2}$$

We assume that the propagation constant of the medium is $k = k_1 + i k_2 = \omega\sqrt{\mu\varepsilon}$, $k_1 \gg k_2 > 0$. k_2 will be put equal to zero after the analysis. The relation between α and the radial spectrum function γ is defined as follows (see Fig.2.3):

$$\alpha = \sigma + i\tau, \qquad \sigma, \ \tau : \text{ real}, \tag{2.3}$$

$$\gamma = (\alpha^2 - k^2)^{1/2} = -i\kappa = -i(k^2 - \alpha^2)^{1/2}. \tag{2.4}$$
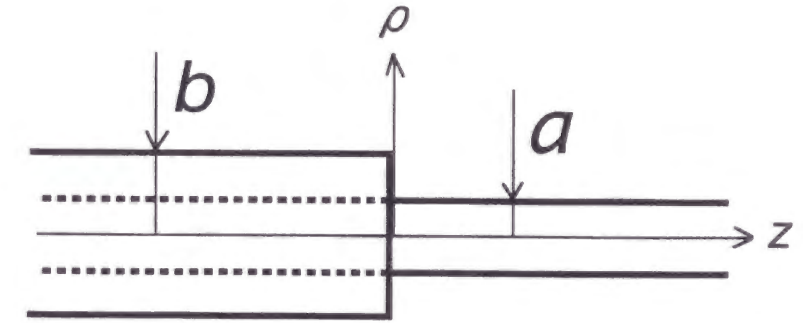
Figure 2.2: Semi-infinite coaxial cable.
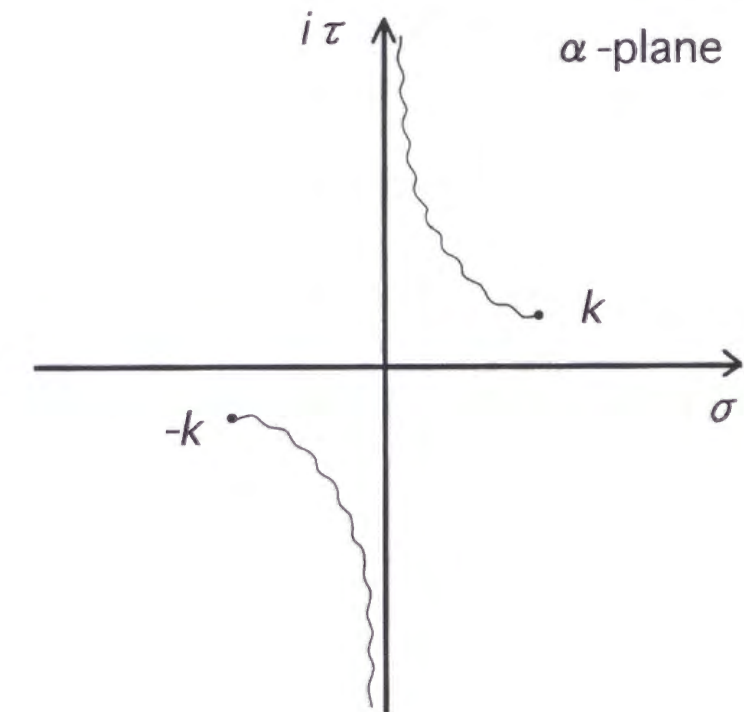
Figure 2.3: Branch cut for the radial spectrum function γ in the α-plane.

For the geometry in Fig.2.2, non zero field components are expressed by using the vector potential $\boldsymbol{A} = \hat{z}\psi(\rho, z)$ as follows [26]:

$$E_z(\rho, z) = \frac{i}{\omega\varepsilon}\left(\frac{\partial^2}{\partial z^2} + k^2\right)\psi(\rho, z), \tag{2.5}$$

$$E_\rho(\rho, z) = \frac{i}{\omega\varepsilon}\frac{\partial^2}{\partial\rho\partial z}\psi(\rho, z), \tag{2.6}$$

$$H_\phi(\rho, z) = -\frac{\partial}{\partial\rho}\psi(\rho, z). \tag{2.7}$$

$\psi(\rho, z)$ satisfies the following wave equation:

$$\frac{1}{\rho}\frac{\partial}{\partial\rho}\left(\rho\frac{\partial\psi}{\partial\rho}\right) + \frac{\partial^2\psi}{\partial z^2} + k^2\psi = 0. \tag{2.8}$$

Let the incident TEM mode current $I^i(z)$ have the following form in $a \leq \rho \leq b$:

$$I^i(z) = I_0 e^{ikz} = 2\pi\rho H_\phi^i(\rho, z), \qquad I_0 = \text{const.} \tag{2.9}$$

The boundary conditions for the field components are given as follows:

$$E_z(a, z) = 0, \qquad (-\infty < z < \infty), \tag{2.10}$$

$$E_z(b-, z) = E_z(b+, z) = 0, \qquad (-\infty < z < 0), \tag{2.11}$$

$$E_z(b-, z) = E_z(b+, z) \equiv E_z(b, z), \qquad (0 < z < \infty), \tag{2.12}$$

$$H_\phi(b+, z) - H_\phi(b-, z) = H_\phi^i(b, z), \qquad (0 < z < \infty), \tag{2.13}$$

where $b+$ and $b-$ mean $b + \varepsilon$ and $b - \varepsilon$, $(\varepsilon \to +0)$, respectively, and this convention is applied throughout the chapter. The edge condition for the end of the outer conductor is given as follows:

$$E_z(b, z) \sim z^{-1/2}, \qquad (z \to 0), \tag{2.14}$$

$$H_\phi(b, z) \sim z^{+1/2}, \qquad (z \to 0). \tag{2.15}$$

Let the Fourier transform of $\psi(\rho, z)$ with respect to z be $\Psi(\rho, \alpha)$, then (2.8) is equivalently expressed as follows:

$$\left[\frac{1}{\rho}\frac{\partial}{\partial\rho}\left(\rho\frac{\partial}{\partial\rho}\cdot\right) - \gamma^2\right]\Psi(\rho, \alpha) = 0, \qquad |\tau| < k_2, \tag{2.16}$$

14

where γ is defined in (2.4). From now on, we put subscripts $+$ or $-$ on the function which is regular in the upper half plane $(\tau > -k_2)$ or regular in the lower half plane $(\tau < k_2)$ in Fig.2.3, respectively. In general, a Fourier transform $F(\alpha)$ of a function $f(z)$ is naturally decomposed into the sum of $F_+(\alpha)$ and $F_-(\alpha)$ [25]-[28],

$$F(\alpha) = F_+(\alpha) + F_-(\alpha), \tag{2.17}$$

$$F_+(\alpha) = \frac{1}{(2\pi)^{1/2}}\int_0^\infty f(z)e^{i\alpha z}dz, \tag{2.18}$$

$$F_-(\alpha) = \frac{1}{(2\pi)^{1/2}}\int_{-\infty}^0 f(z)e^{i\alpha z}dz. \tag{2.19}$$

By using (2.5),(2.10), and the fact that the field decays as $\rho \to +\infty$, solutions for (2.16) are expressed as follows:

$$\Psi(\rho, \alpha) = \Psi_+(\rho, \alpha) + \Psi_-(\rho, \alpha) = A(\alpha)\frac{K_0(\gamma\rho)}{K_0(\gamma b)}, \qquad (\rho \geq b) \tag{2.20}$$

$$\Psi(\rho, \alpha) = B(\alpha)\frac{I_0(\gamma\rho)K_0(\gamma a) - K_0(\gamma\rho)I_0(\gamma a)}{I_0(\gamma b)K_0(\gamma a) - K_0(\gamma b)I_0(\gamma a)}, \qquad (a \leq \rho \leq b), \tag{2.21}$$

where, $A(\alpha)$ and $B(\alpha)$ are unknown functions. In the above formula, we have introduced normalization functions for the later convenience. We define the Fourier transform of $E_z(\rho, z)$ and $H_\phi(\rho, z)$ with respect to z as $E(\rho, \alpha)$ and $H(\rho, \alpha)$, respectively. By using (2.5), (2.7), (2.20), and (2.21), we have the following relations:

$$E_+(b+, \alpha) + E_-(b+, \alpha) = \frac{\gamma^2}{i\omega\varepsilon}A(\alpha), \tag{2.22}$$

$$H_+(b+, \alpha) + H_-(b+, \alpha) = \frac{\gamma K_1(\gamma b)}{K_0(\gamma b)}A(\alpha), \tag{2.23}$$

$$E_+(b-, \alpha) + E_-(b-, \alpha) = \frac{\gamma^2}{i\omega\varepsilon}B(\alpha), \tag{2.24}$$

$$H_+(b-, \alpha) + H_-(b-, \alpha) = \gamma B(\alpha)\frac{I_1(\gamma b)K_0(\gamma a) + K_1(\gamma b)I_0(\gamma a)}{I_0(\gamma b)K_0(\gamma a) - K_0(\gamma b)I_0(\gamma a)}. \tag{2.25}$$

The boundary conditions (2.11), (2.12), and (2.13) lead to the following relations:

$$E_-(b+, \alpha) = 0, \tag{2.26}$$

$$E_-(b-, \alpha) = 0, \tag{2.27}$$

15

$$E_+(b+,\alpha) = E_+(b-,\alpha) \equiv E_+(b,\alpha), \tag{2.28}$$

$$2\pi b\{H_+(b+,\alpha) - H_+(b-,\alpha)\} = \frac{1}{(2\pi)^{1/2}} \int_0^\infty I^i(z)e^{i\alpha z}dz,$$

$$= \frac{iI_0}{(2\pi)^{1/2}(\alpha+k)}. \tag{2.29}$$

The formulas (2.22), (2.24), (2.26), (2.27), and (2.28) give expressions of $A(\alpha)$ and $B(\alpha)$ as follows:

$$A(\alpha) = B(\alpha) = E_+(b,\alpha)\frac{i\omega\varepsilon}{\gamma^2}. \tag{2.30}$$

Next, we introduce an unknown function $J_-(\alpha)$ as follows:

$$2\pi b\{H_-(b+,\alpha) - H_-(b-,\alpha)\} = J_-(\alpha). \tag{2.31}$$

Subtracting (2.25) from (2.23), and using (2.29), (2.30), and (2.31), we have the following Wiener-Hopf equation with respect to E_+ and J_- :

$$\frac{iI_0}{(2\pi)^{1/2}(\alpha+k)} + J_-(\alpha) + \frac{2\pi\omega\varepsilon E_+(b,\alpha)}{i\gamma^2 L(\alpha)} = 0, \tag{2.32}$$

$$L(\alpha) = \frac{K_0(\gamma b)}{K_0(\gamma a)}\{I_0(\gamma b)K_0(\gamma a) - K_0(\gamma b)I_0(\gamma a)\}. \tag{2.33}$$

$L(\alpha)$ can be factorized in a product form $L(\alpha) = L_+(\alpha)L_-(\alpha)$. The procedure is given in Appendix A. We rewrite (2.32) as follows:

$$\frac{iI_0}{(2\pi)^{1/2}(\alpha+k)}\{(\alpha-k)L_-(\alpha) + 2kL_-(-k)\} + (\alpha-k)L_-(\alpha)J_-(\alpha)$$

$$= \frac{2\pi\omega\varepsilon i}{(\alpha+k)L_+(\alpha)}E_+(b,\alpha) + \frac{2kI_0 iL_-(-k)}{(2\pi)^{1/2}(\alpha+k)}. \tag{2.34}$$

The left-hand and right-hand sides of the above formula are regular in $\tau < k_2$ and $\tau > -k_2$, respectively, in the α-plane. Furthermore they are both regular in $|\tau| < k_2$. Then the theorem of identity states that the both sides of (2.34) are identical to an integral function

<div style="page-break"></div>

$P(\alpha)$ [25]-[28]. By using the edge condition and the results of Appendix A, the following relations are obtained in $|\tau| < k_2$ as $|\alpha| \to \infty$:

$$E_+(b,\alpha) \sim \alpha^{-1/2}, \tag{2.35}$$

$$J_-(\alpha) \sim H_-(b,\alpha) \sim \alpha^{-3/2}, \tag{2.36}$$

$$L_-(\alpha) \sim L_+(\alpha) \sim \alpha^{-1/2}. \tag{2.37}$$

By using the above properties, we see that the left-hand side of (2.34) decays as $\alpha^{-1/2}$, and the right-hand side decays as α^{-1} in $|\tau| < k_2$ when $|\alpha| \to \infty$. Then the Liouville's theorem states $P(\alpha) \equiv 0$ [25]-[28]. Thus the solution of the Wiener-Hopf equation (2.32) is given as follows:

$$E_+(b,\alpha) = -\frac{\eta I_0}{(2\pi)^{1/2}\pi}L_+(\alpha)L_-(-k), \tag{2.38}$$

where, $\eta = \sqrt{\mu/\varepsilon}$. By using (2.25), (2.30), and (2.38), $H_\phi(\rho,z)$ is expressed in the region $a \le \rho \le b$ as follows:

$$H_\phi(\rho,z) = \frac{1}{(2\pi)^{1/2}} \int_{-\infty}^\infty H(\rho,\alpha)e^{-i\alpha z}d\alpha,$$

$$= \frac{kI_0 i}{2\pi^2}L_-(-k)U(\rho,z), \tag{2.39}$$

$$U(\rho,z) = \int_C u(\rho,\alpha)e^{-i\alpha z}d\alpha, \tag{2.40}$$

$$u(\rho,\alpha) = \frac{L_+(\alpha)}{\gamma} \cdot \frac{I_1(\gamma\rho)K_0(\gamma a) + K_1(\gamma\rho)I_0(\gamma a)}{I_0(\gamma b)K_0(\gamma a) - K_0(\gamma b)I_0(\gamma a)}.$$

If the radius of the coaxial cable is much smaller compared with the operating wavelength where only the TEM mode can propagate, the poles of the integrand of $U(\rho,z)$ are located in α-plane as shown in Fig.2.4. In Fig.2.4, the poles in the upper and lower half planes correspond to the modes in the negative and positive z-axis, respectively. The pole at $\alpha = k$ represents the reflected TEM mode from the discontinuous end of the coaxial cable. The pole at $\alpha = -k$ cancels the incident TEM mode in the positive z region.

By using the relations,

$$I_0(\gamma b)K_0(\gamma a) - K_0(\gamma b)I_0(\gamma a) \rightarrow \ln\frac{b}{a}, \quad (\gamma \rightarrow 0), \tag{2.41}$$

$$I_1(\gamma\rho)K_0(\gamma a) + K_1(\gamma\rho)I_0(\gamma a) \sim \frac{1}{\gamma\rho}, \quad (\gamma \rightarrow 0), \tag{2.42}$$

the magnetic field $H_\phi^r(\rho, z)$ for the reflected TEM mode from the end of the coaxial cable is calculated by the residue of the pole at $\alpha = k$. Then the reflected current $I^r(z)$ is obtained as follows:

$$\begin{aligned} I^r(z) &= 2\pi a H_\phi^r(a, z), \\ &= -\frac{I_0}{\ln(b/a)}\{L_+(k)\}^2 e^{-ikz}. \end{aligned} \tag{2.43}$$
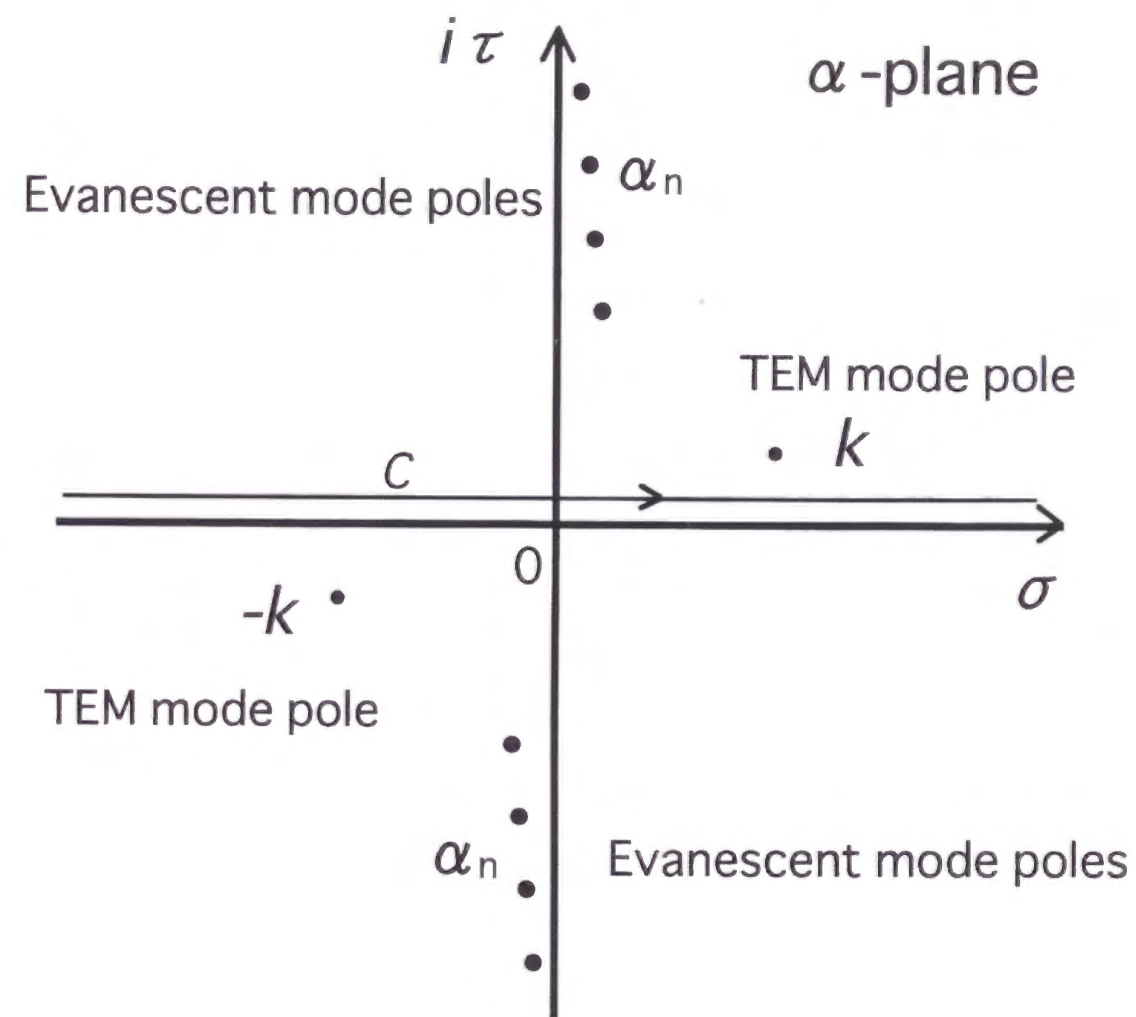
Figure 2.4: The integration contour C and poles of the integrand of $U(\rho, z)$ in the α-plane.

The ratio of $I^r(z)$ to $I^i(z)$ gives the reflection coefficient $R(z)$ of the semi-infinite coaxial cable as follows:

$$R(z) = \frac{I^r(z)}{I^i(z)} = -\frac{1}{\ln(b/a)}\{L_+(k)\}^2 e^{-2ikz}, \tag{2.44}$$

$$L_+(k) = \left[\frac{\pi}{2}\left\{J_0(ka)N_0(kb) - N_0(ka)J_0(kb)\right\}\frac{H_0^{(1)}(kb)}{H_0^{(1)}(ka)}\right]^{\frac{1}{2}}$$

$$\cdot \exp\left[i\frac{k(b-a)}{\pi}\left\{1 + \ln 2 - \frac{\pi}{2} - C_e - \ln\frac{k(b-a)}{\pi i}\right\}\right]$$

$$\cdot \left[\prod_{n=1}^{\infty}\left(1 + \frac{k}{\alpha_n}\right)^{-k(b-a)/(n\pi i)}\right]\exp\left\{\xi(k,a,b)\right\}, \tag{2.45}$$

$$\xi(k,a,b) = q(k,b) - q(k,a), \tag{2.46}$$

$$q(k,x) = \int_0^{\infty} f(\omega, k, x)d\omega, \tag{2.47}$$

$$f(\omega, k, x) = \frac{x}{\pi}\left[1 - \frac{2}{\pi\omega x}\cdot\frac{1}{\{J_0(\omega x)\}^2 + \{N_0(\omega x)\}^2}\right]\ln\left(1 + \frac{k}{\sqrt{k^2 - \omega^2}}\right), \tag{2.48}$$

$$\sqrt{k^2 - \omega^2} = i\sqrt{\omega^2 - k^2}, \tag{2.49}$$

where $C_e \simeq 0.5772$ is Euler's constant and α_n is defined as follows:

$$I_0(\sqrt{\alpha_n^2 - k^2}b)K_0(\sqrt{\alpha_n^2 - k^2}a) - K_0(\sqrt{\alpha_n^2 - k^2}b)I_0(\sqrt{\alpha_n^2 - k^2}a) = 0, \tag{2.50}$$

$$\text{Im}\alpha_n > 0, \quad \text{Im}\alpha_n < \text{Im}\alpha_{n+1}, \qquad (n = 1, 2, 3, \ldots\ldots),$$

$$\alpha_n \sim \frac{in\pi}{b-a}, \qquad (n \to \infty \quad \text{or} \quad a, b \ll \lambda).$$

Although (2.44) gives the exact solution, it has a disadvantage of practical applications because it contains infinite integrals as well as an infinite product. In general, a and b for ECCD are very small compared with the operating wavelength λ. In the following, we derive a simple approximate formula for R which is valid when $0.001\lambda \le a, b \le 0.1\lambda$.

The infinite integral given by (2.47) is evaluated numerically and an effort has been made to find an approximate numerical formula. Special care is needed for the numerical

evaluation of (2.47) because the integrand has numerical singularities. The corresponding procedure is given in Appendix B. It has been observed that a polynomial of logarithmic variables improves the convergence with respect to the order of the series in this case. The resultant expression of (2.47) in the domain $0.001 \le x/\lambda \le 0.1$ is as follows:

$$q(k,x) \equiv q(kx) \equiv Q(x/\lambda), \tag{2.51}$$

$$Q(x) \simeq -0.16073 + 0.017312\ln x + 0.0093628(\ln x)^2 + 0.00072849(\ln x)^3$$

$$+ i\{-0.023700 - 0.029142\ln x - 0.0047721(\ln x)^2 - 0.00021525(\ln x)^3\}.$$

The above formula approximates the exact values within 3% errors. The part of infinite product is approximated as follows:

$$\prod_{n=1}^{\infty}\left(1 + \frac{k}{\alpha_n}\right)^{-k(b-a)/(i\pi n)} \simeq e^{-C_e k(b-a)/(i\pi)}/\Gamma\left(1 + \frac{k(b-a)}{i\pi}\right),$$

$$\simeq \exp\left[\frac{\{k(b-a)\}^2}{12}\right], \tag{2.52}$$

where, the following formulas have been applied:

$$\alpha_n \simeq in\pi/(b-a), \tag{2.53}$$

$$\prod_{n=1}^{\infty}\left(1 + \frac{z}{an}\right)^{-z/(an)} = \frac{e^{-C_e z/a}}{\Gamma(1 + z/a)},$$

$$\simeq \exp\left\{-\frac{\pi^2}{12}\left(\frac{z}{a}\right)^2\right\}, \qquad (z/a \to 0). \tag{2.54}$$

The error due to the approximation of α_n given in (2.53) in the domain $0.001\lambda \le a, b \le 0.1\lambda$ is within 10%. The remaining parts of (2.45) are approximated as follows:

$$\frac{\pi}{2}\{J_0(ka)N_0(kb) - N_0(ka)J_0(kb)\} \simeq \ln\frac{b}{a}, \tag{2.55}$$

$$\frac{H_0^{(1)}(kb)}{H_0^{(1)}(ka)} \simeq \frac{\ln(kb/2) + C_e - i\pi/2}{\ln(ka/2) + C_e - i\pi/2}. \tag{2.56}$$

The final expression of $R(z)$ is given as follows:

$$R(z) \simeq -\frac{\ln(kb/2) + C_e - i\pi/2}{\ln(ka/2) + C_e - i\pi/2} \exp\{2(M - ikz)\}, \qquad (2.57)$$

$$M = Q\left(\frac{b}{\lambda}\right) - Q\left(\frac{a}{\lambda}\right) + \frac{\{k(b-a)\}^2}{12}$$

$$+ \frac{k(b-a)i}{\pi}\left\{1 + \ln 2 - \frac{\pi}{2} - C_e - \ln\frac{k(b-a)}{\pi i}\right\}. \qquad (2.58)$$

To see the validity of (2.57), a comparison is plotted in Fig.2.5 between the approximate values calculated by (2.57) and the exact values in the case of $a = 0.01\lambda$ and $0.015\lambda \leq b \leq 0.1\lambda$. The correspondence between them is appropriate for practical applications.
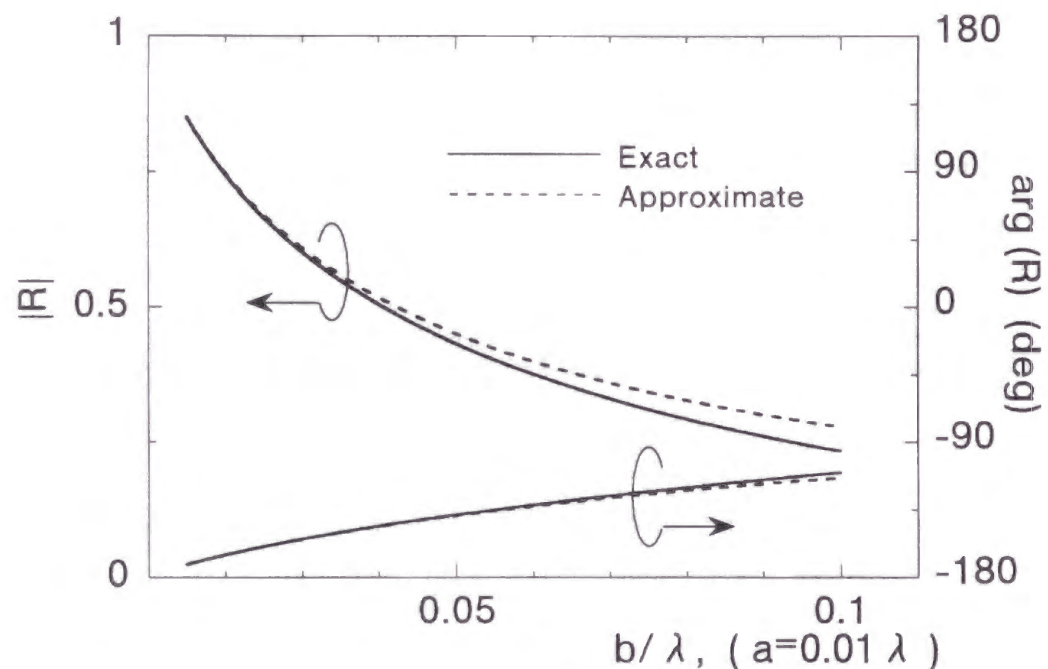
Figure 2.5: Comparison between the exact formula (2.44) and the approximate formula (2.57).

2.3   Input admittance

In this section, the TEM mode reflection coefficient for the semi-infinite coaxial cable is applied to an analysis of the input admittance of ECCD in Fig.2.1. From now on, we write $R = R(0)$ in (2.57). We derive an approximate form of the current distribution $I(z)$ on $\rho = a$ with the methods by Chen and Keller [32], and Lee and Mittra [33]. In this case, we treat the region between the circular pipe and the feeding coaxial cable in Fig.2.1 as a cavity, where the TEM mode is the only propagation mode and the effect of end discontinuities is contained in R. We define $I_{inf}(z)$ as a current on $\rho = a$ which is excited by the annular ring slot when the discontinuities of the coaxial line are absent. We also define $I_{cav}(z)$ as currents due to multiple reflections between the ends of the cavity when the TEM mode current in $I_{inf}(z)$ is incident. $I_{cav}(z)$ is identified as the Neumann series which can be summed up in a closed form. For more details, see the derivation of Eq.(5.2) in Reference [33]. $I(z)$ is approximately calculated by superposition of $I_{inf}(z)$ and $I_{cav}(z)$ as follows:

$$I(z) \simeq I_{inf}(z) + I_{cav}(z), \qquad (2.59)$$

$$I_{inf}(z) = I_0 U(z) + I_{np}(z), \qquad (2.60)$$

$$I_{cav}(z) = I_0 \frac{U(l_1) + RU(l_2)U(l_1 + l_2)}{1 - R^2\{U(l_1 + l_2)\}^2} RU(z - l_1)$$

$$+ I_0 \frac{U(l_2) + RU(l_1)U(l_1 + l_2)}{1 - R^2\{U(l_1 + l_2)\}^2} RU(z + l_2), \qquad (2.61)$$

$$U(z) = e^{ik|z|}, \qquad (2.62)$$

where the term $I_0 U(z)$ and $I_{np}(z)$ in (2.60) correspond to the currents due to the TEM mode and non-propagating modes, respectively. If the annular ring slot in Fig.2.1 is excited by a voltage Δv, the input admittance Y_{11} of ECCD is given as follows:

$$Y_{11} = \frac{I(w) + I(-w)}{2\Delta v}, \qquad (2.63)$$

$$\simeq Y_{inf} + Y_{cav}, \tag{2.64}$$

$$Y_{inf} = \frac{I_{inf}(w) + I_{inf}(-w)}{2\Delta v}, \tag{2.65}$$

$$Y_{cav} = \frac{I_{cav}(w) + I_{cav}(-w)}{2\Delta v}. \tag{2.66}$$

We calculate Y_{inf}. We assume that the width $2w$ of the annular ring slot is much smaller compared with λ, and it can be modeled by the following uniform magnetic current M_ϕ :

$$M_\phi(\rho, z) = \begin{cases} -\{\Delta v/(2w)\}\delta(\rho - a), & (|z| < w), \\ 0, & (|z| \geq w). \end{cases} \tag{2.67}$$

The only non-zero component of the magnetic field inside the coaxial cable is $H_\phi(\rho, z)$. We define the Green's function G with respect to M_ϕ as follows:

$$H_\phi(\rho, z) = i\omega\varepsilon \int_{-w}^{w} dz' \int_a^b \rho' d\rho' G(\rho, z|\rho', z') M_\phi(\rho', z'), \tag{2.68}$$

$$\frac{\partial}{\partial\rho}\left\{\frac{1}{\rho}\frac{\partial}{\partial\rho}(\rho G)\right\} + \frac{\partial^2 G}{\partial z^2} + k^2 G = -\frac{\delta(\rho - \rho')}{\rho'}\delta(z - z'). \tag{2.69}$$

G can be constructed as follows:

$$G(\rho, z|\rho', z') = -\frac{e^{ik|z-z'|}}{2ik\rho\rho'\ln(b/a)} + \frac{1}{2}\sum_{n=1}^{\infty}\frac{P_n(\rho)P_n(\rho')}{\lambda_n F_n}e^{-\lambda_n|z-z'|}, \tag{2.70}$$

$$P_n(\rho) = J_1(p_n\rho)N_0(p_n a) - N_1(p_n\rho)J_0(p_n a), \tag{2.71}$$

$$\lambda_n = \sqrt{p_n^2 - k^2}, \quad \partial\{\rho P_n(\rho)\}/\partial\rho|_{\rho=b} = 0, \tag{2.72}$$

$$F_n = \frac{2}{\pi^2 p_n^2}\left[\left\{\frac{J_0(p_n a)}{J_0(p_n b)}\right\}^2 - 1\right]. \tag{2.73}$$

By using (2.67), (2.68), and (2.70), $I_{inf}(z)$ is calculated as follows:

$$I_{inf}(z) = 2\pi a H_\phi(a, z), \tag{2.74}$$

$$= \frac{Y_0}{2}\Delta v \cdot \frac{\sin(kw)}{kw}U(z) - \frac{i\pi k}{\eta w}\Delta v\sum_{n=1}^{\infty}\frac{1 - e^{-2\lambda_n w}}{\lambda_n^2}\left[\left\{\frac{J_0(p_n a)}{J_0(p_n b)}\right\}^2 - 1\right]^{-1},$$

$$\simeq \frac{Y_0}{2}\Delta v \cdot U(z) - \frac{i\pi k}{\eta w}\Delta v\sum_{n=1}^{\infty}\frac{1 - e^{-2\lambda_n w}}{\lambda_n^2}\left[\left\{\frac{J_0(p_n a)}{J_0(p_n b)}\right\}^2 - 1\right]^{-1}, \tag{2.75}$$

$$Y_0 = \frac{2\pi}{\eta\ln(b/a)}, \tag{2.76}$$

where (2.75) is obtained by assuming $kw \ll 1$. The first term and the last summation part in (2.75) are identified with $I_0 U(z)$ and $I_{np}(z)$ in (2.60), respectively. By comparing the coefficients of $U(z)$ in the first terms in (2.60) and (2.75), we have the following relation:

$$I_0 = \frac{Y_0}{2}\Delta v. \tag{2.77}$$

Y_{inf} is obtained by (2.65) and (2.75) as follows:

$$Y_{inf} \simeq \frac{Y_0}{2} - \frac{i\pi k}{\eta w}\sum_{n=1}^{\infty}\frac{1 - e^{-2\lambda_n w}}{\lambda_n^2}\left[\left\{\frac{J_0(p_n a)}{J_0(p_n b)}\right\}^2 - 1\right]^{-1}, \tag{2.78}$$

where the approximation $U(\pm w) = e^{ik|w|} \simeq 1$ is made as in (2.75). Y_{cav} is readily obtained by (2.61), (2.66), and (2.77) as follows:

$$Y_{cav} \simeq \frac{Y_0}{2}R\frac{\{U(l_1)\}^2 + \{U(l_2)\}^2 + 2R\{U(l_1 + l_2)\}^2}{1 - R^2\{U(l_1 + l_2)\}^2}, \tag{2.79}$$

where the approximations $U(\pm w - l_1) \simeq U(l_1)$ and $U(\pm w + l_2) \simeq U(l_2)$ are made. By using (2.62), (2.64), (2.78), and (2.79), we finally obtain Y_{11} as follows:

$$Y_{11} \simeq \frac{Y_0}{2} \cdot \frac{(1 + Re^{2ikl_1})(1 + Re^{2ikl_2})}{1 - R^2 e^{2ik(l_1 + l_2)}} - \frac{i\pi k}{\eta w}\sum_{n=1}^{\infty}\frac{1 - e^{-2\lambda_n w}}{\lambda_n^2}\left[\left\{\frac{J_0(p_n a)}{J_0(p_n b)}\right\}^2 - 1\right]^{-1}. \tag{2.80}$$

In the case of $l_1 = l_2 = l$, (2.80) becomes,

$$Y_{11}(l_1 = l_2 = l) \simeq \frac{Y_0}{2} \cdot \frac{1 + Re^{2ikl}}{1 - Re^{2ikl}} - \frac{i\pi k}{\eta w}\sum_{n=1}^{\infty}\frac{1 - e^{-2\lambda_n w}}{\lambda_n^2}\left[\left\{\frac{J_0(p_n a)}{J_0(p_n b)}\right\}^2 - 1\right]^{-1}. \tag{2.81}$$

When $R = 0$, the first term in (2.81) reduces to $Y_0/2$ which represents the admittance in the case of two coaxial lines connected and fed at the center. If we put $R = -1$ and $l = 1/4\lambda$ in (2.81), then $Y_{11} = \infty$; *i.e.* when each end of the coaxial cable is open-circuited and the location of the annular ring slot is a quarter-wavelength away from the ends, the annular ring slot is short-circuited, which meets the physical insight.

To verify the applicability of the derived formula, measurements have been carried out. S parameters S_{11} and S_{21} are measured for the two ports 1 and 2 in Fig.2.1 of

24

25

the feeding coaxial cable with characteristic impedance Z_f. An equivalent circuit for the geometry consists of a transmission line with characteristic impedance Z_f loaded with input impedance Z_{11} of ECCD and Z_f in series. S_{11} and S_{21} are calculated as follows:

$$S_{11} = \frac{Z_{11}}{Z_{11} + 2Z_f}, \tag{2.82}$$

$$S_{21} = \frac{2Z_f}{Z_{11} + 2Z_f}, \tag{2.83}$$

$$Z_{11} = 1/Y_{11} \tag{2.84}$$

Figure 2.6 shows comparisons between the measured and calculated values. The parameters are $l_1 = l_2 = 0.21\lambda_{f0}$, $a = 0.0092\lambda_{f0}$, $b = 0.023\lambda_{f0}$, $w = 0.0041\lambda_{f0}$, and $Z_f = 50\Omega$, where λ_{f0} corresponds to the free space wavelength at the frequency f_0.
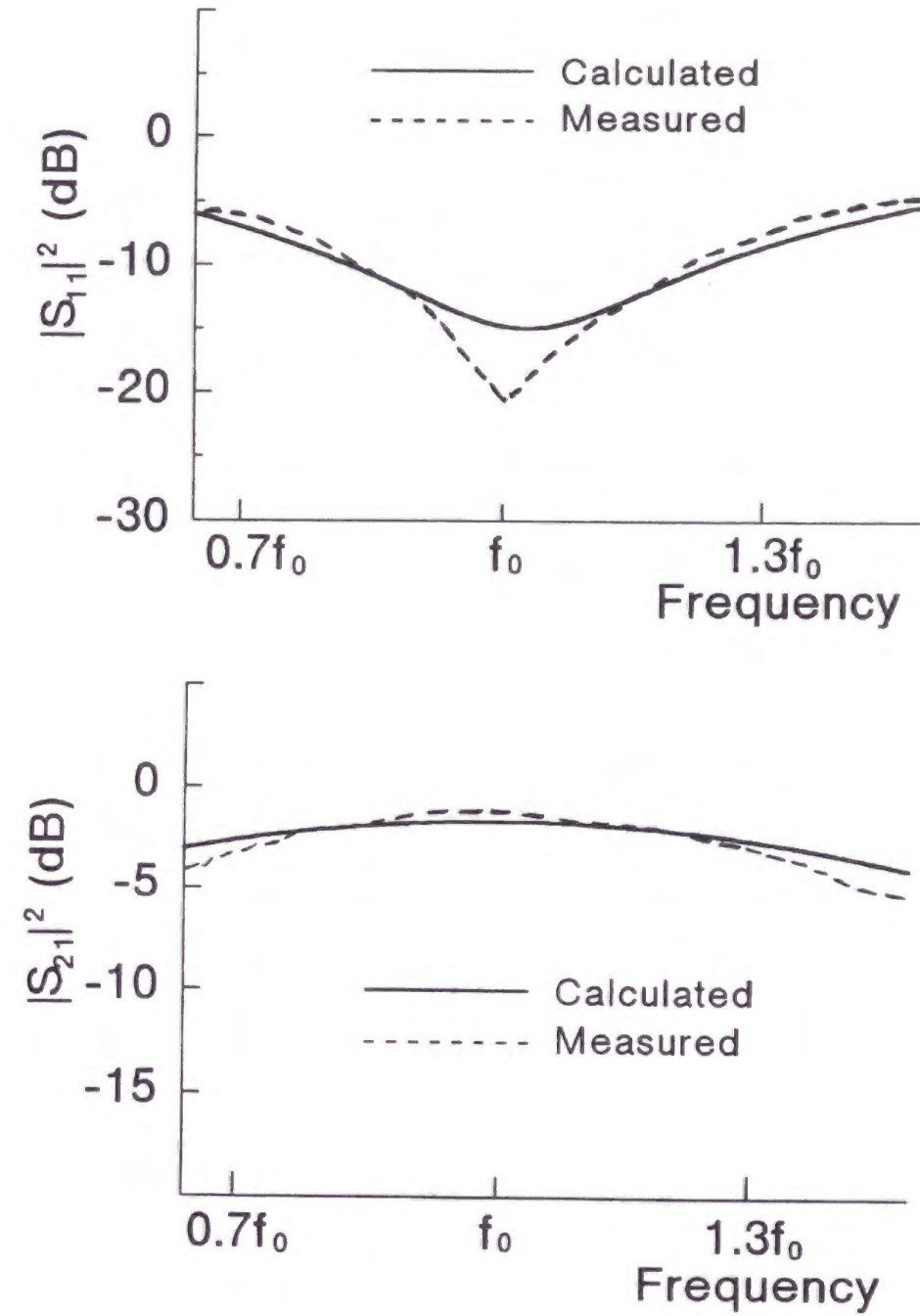
Figure 2.6: Comparison between calculated and measured values for S_{11} and S_{21} of ECCD in Fig.2.1, where $l_1 = l_2 = 0.21\lambda_{f0}$, $a = 0.0092\lambda_{f0}$, $b = 0.023\lambda_{f0}$, $w = 0.0041\lambda_{f0}$, and $Z_f = 50\Omega$.

2.4 Radiation patterns

In this section, the radiation pattern of ECCD is analyzed. We model the circular pipe and the annular ring slot in ECCD as rotationally symmetric electric and magnetic currents, respectively, which are located above a perfectly conducting infinite circular cylinder of radius a as shown in Fig.2.7. Fields of the currents are expressed through the Green's functions of the circular cylinder. The current distribution of the circular pipe is determined by an integral equation with respect to the electric field boundary condition on the surface of the pipe, and then the radiation pattern is obtained.

The non-zero fields $E_z^{(e)}(\rho, z)$, $E_\rho^{(e)}(\rho, z)$, and $H_\phi^{(e)}(\rho, z)$ of the $\hat{z}$-directed electric current $J_z(z')$ at the radius b are given by (2.5) to (2.7) with the vector potential $\psi(\rho, z)$ replaced by $A_z(\rho, z)$. $A_z(\rho, z)$ is calculated by the Green's function of the infinite circular cylinder as follows [34]:

$$A_z(\rho, z) = \int_{-l}^{l} dz' G^{(e)}(\rho, z|b, z') J_z(z'), \tag{2.85}$$

$$G^{(e)}(\rho, z|b, z') = \frac{ib}{4} \int_{-\infty}^{\infty} d\alpha e^{i\alpha|z-z'|} \frac{H_0^{(1)}(\kappa\rho_>)}{H_0^{(1)}(\kappa a)} \left\{ J_0(\kappa\rho_<) H_0^{(1)}(\kappa a) - H_0^{(1)}(\kappa\rho_<) J_0(\kappa a) \right\}, \tag{2.86}$$

where $\rho_>$ and $\rho_<$ represent the larger and the smaller values of ρ and b, respectively, and κ is given in (2.4). The non-zero fields of the $\hat{\phi}$-directed magnetic current $M_\phi(z')$ on the surface of the circular cylinder are given as follows [34]:

$$E_\rho^{(m)}(\rho, z) = \frac{1}{i\omega\varepsilon} \frac{\partial H_\phi^{(m)}}{\partial z}, \tag{2.87}$$

$$E_z^{(m)}(\rho, z) = \frac{i}{\omega\varepsilon} \frac{1}{\rho} \frac{\partial}{\partial \rho} \left(\rho H_\phi^{(m)} \right), \tag{2.88}$$

$$H_\phi^{(m)}(\rho, z) = i\omega\varepsilon \int_{-w}^{w} dz' G^{(m)}(\rho, z|a, z') M_\phi(z'), \tag{2.89}$$

$$G^{(m)}(\rho, z|a, z') = -\frac{1}{2\pi} \int_{-\infty}^{\infty} d\alpha e^{i\alpha|z-z'|} \frac{1}{\kappa} \frac{H_1^{(1)}(\kappa\rho)}{H_0^{(1)}(\kappa a)}. \tag{2.90}$$
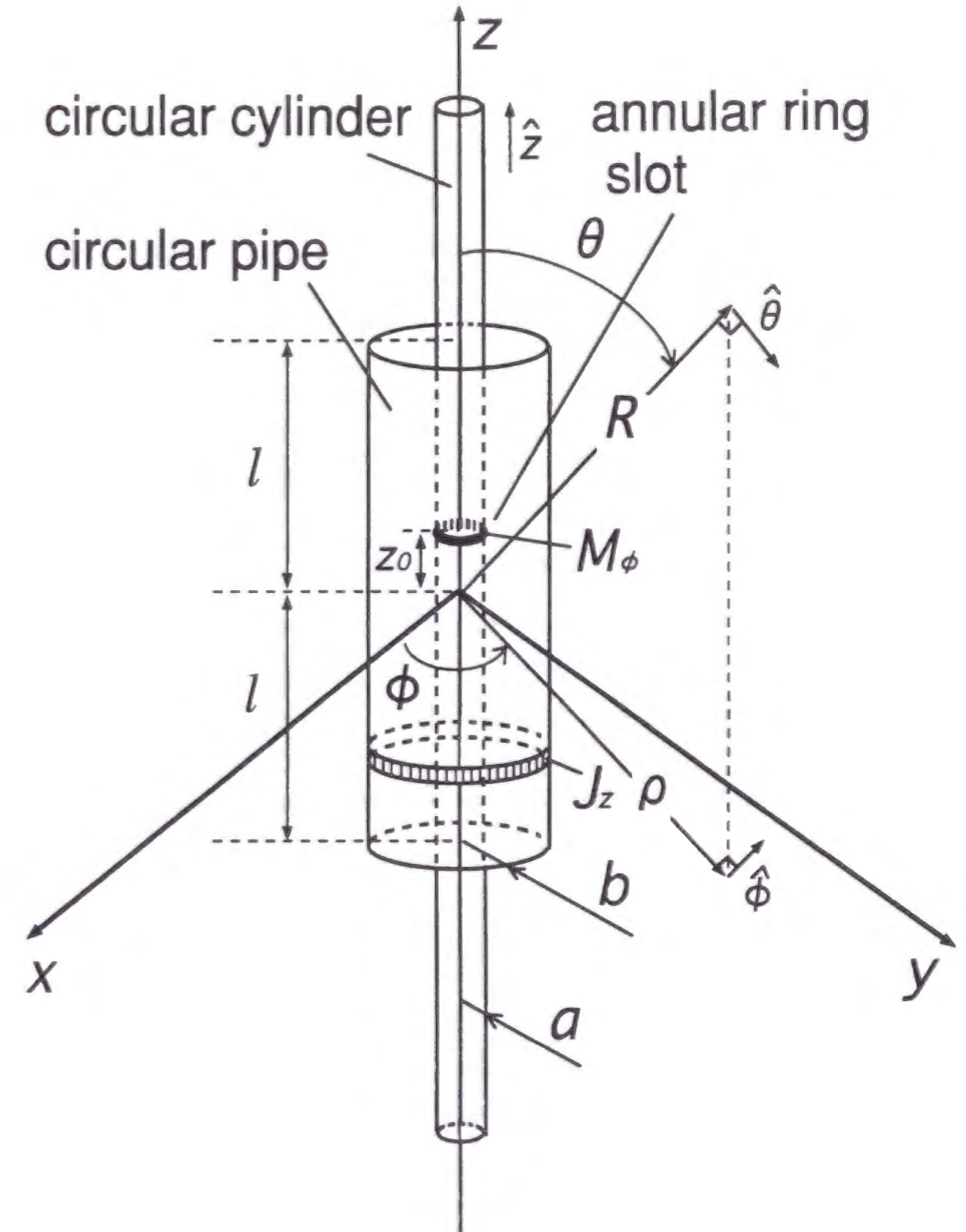
Figure 2.7: Geometry of ECCD and rotationally symmetric electric and magnetic currents on a perfectly conducting infinite circular cylinder.

If we treat M_ϕ as a known source which gives an incident wave of the scattering problem, the following integral equation for J_z is obtained by the electric field boundary condition on the surface of the circular pipe:

$$E_z^{(m)}(b, z) + E_z^{(e)}(b, z) = 0, \qquad (|z| \leq l). \tag{2.91}$$

We use the Galerkin's method to solve the above integral equation. We expand $J_z(z)$ with a class of expansion functions $\Psi_n(z), (n = 1, 2, 3, ...)$ as follows:

$$J_z(z) = \sum_{n=1}^{\infty} X_n \Psi_n(z), \tag{2.92}$$

$$\Psi_n(z) = \frac{1}{2l} \sin\left\{ \frac{n\pi}{2l}(z + l) \right\}, \tag{2.93}$$

where $X_n, (n = 1, 2, 3, ...)$ are unknown coefficients to be determined. The integral equation (2.91) is equivalent to the following form in the Galerkin's sense,

$$\int_{-l}^{l} dz \Psi_n(z)\{ E_z^{(m)}(b, z) + E_z^{(e)}(b, z) \} = 0, \qquad (n = 1, 2, 3, ...). \tag{2.94}$$

After some calculations, (2.94) reduces to the following simultaneous linear equations with respect to X_n by assuming $M_\phi(z) = M_0 \delta(z - z_0)$ for simplicity:

$$\sum_{n=1}^{\infty} A_{mn} X_n = P_m, \tag{2.95}$$

$$A_{mn} = -\frac{\eta b}{2k} \int_0^\infty d\alpha B_{mn}(\alpha) \kappa^2 \frac{H_0^{(1)}(\kappa b)}{H_0^{(1)}(\kappa a)} \{ J_0(\kappa b) H_0^{(1)}(\kappa a) - H_0^{(1)}(\kappa b) J_0(\kappa a) \}, \tag{2.96}$$

$$B_{mn}(\alpha) = C_m(\alpha) C_n(\alpha) + S_m(\alpha) S_n(\alpha), \tag{2.97}$$

$$P_m = -\frac{M_0}{\pi} \int_0^\infty d\alpha \frac{H_0^{(1)}(\kappa b)}{H_0^{(1)}(\kappa a)} \{ C_m(\alpha) \cos(\alpha z_0) + S_m(\alpha) \sin(\alpha z_0) \}, \tag{2.98}$$

$$C_n(\alpha) = \int_{-l}^{l} dz \Psi(z) \cos(\alpha z), \tag{2.99}$$

$$= \frac{n\pi \cos(\alpha l)}{(2\alpha l)^2 - (n\pi)^2} \{ (-1)^n - 1 \}, \tag{2.100}$$

$$S_n(\alpha) = \int_{-l}^{l} dz \Psi(z) \sin(\alpha z), \tag{2.101}$$

$$= \frac{n\pi \sin(\alpha l)}{(2\alpha l)^2 - (n\pi)^2} \{ (-1)^n + 1 \}. \tag{2.102}$$

An approximate solution is obtained by replacing the summation in (2.95) with finite N terms and a matrix inversion. Now we calculate the radiation pattern of the current distribution. We neglect contribution of M_ϕ for the radiation pattern by assuming that the dimension of the annular ring slot is much smaller compared with the circular pipe. The magnetic field $H_\phi^{(e)}$ of J_z is calculated by (2.7) and (2.85) as follows:

$$H_\phi^{(e)}(\rho, z) = \int_{-l}^{l} dz' G_H^{(e)}(\rho, z|b, z') J_z(z'), \tag{2.103}$$

$$G_H^{(e)}(\rho, z|b, z') = -\frac{\partial}{\partial \rho} G^{(e)}(\rho, z|b, z'), \tag{2.104}$$

$$= \frac{ib}{4} \int_{-\infty}^{\infty} d\alpha \kappa e^{i\alpha|z - z'|} \frac{H_1^{(1)}(\kappa \rho)}{H_0^{(1)}(\kappa a)} \{ J_0(\kappa b) H_0^{(1)}(\kappa a) - H_0^{(1)}(\kappa b) J_0(\kappa a) \}, \qquad (\rho \geq b). \tag{2.105}$$

In the far field region, an asymptotic approximation can be employed for the integral in (2.105) with the aid of the following formula [34]:

$$\int_{-\infty}^{\infty} d\alpha F(\alpha, \kappa) H_n^{(1)}(\kappa \rho) e^{i\alpha|z|} \sim F(k\cos\theta, k\sin\theta) \frac{2}{R} e^{ikR - i(n+1)\pi/2}, \tag{2.106}$$

$$z = R\cos\theta, \tag{2.107}$$

$$\rho = R\sin\theta, \tag{2.108}$$

$$R = \sqrt{\rho^2 + z^2}. \tag{2.109}$$

The final expression of the far field is given as follows:

$$E_\theta^{(e)} \simeq \eta H_\phi^{(e)}, \tag{2.110}$$

$$\simeq \frac{e^{ikR}}{R} \cdot \frac{\eta kb\sin\theta}{2iH_0^{(1)}(ka\sin\theta)} \{ J_0(kb\sin\theta) H_0^{(1)}(ka\sin\theta)$$

$$- H_0^{(1)}(kb\sin\theta) J_0(ka\sin\theta) \} \sum_{n=1}^{N} X_n D_n(k\cos\theta), \tag{2.111}$$

$$D_n(\alpha) = \int_{-l}^{l} dz \Psi_n(z) e^{-i\alpha z}, \tag{2.112}$$

$$= \frac{n\pi}{(2\alpha l)^2 - (n\pi)^2} \{ (-1)^n e^{-i\alpha l} - e^{i\alpha l} \}. \tag{2.113}$$

Figure 2.8 shows the calculated and measured radiation patterns of ECCD in Fig.2.7, where the parameters are the same as those of Fig.2.6 in the previous section with $l = l_1 = l_2$ and $z_0 = 0$.
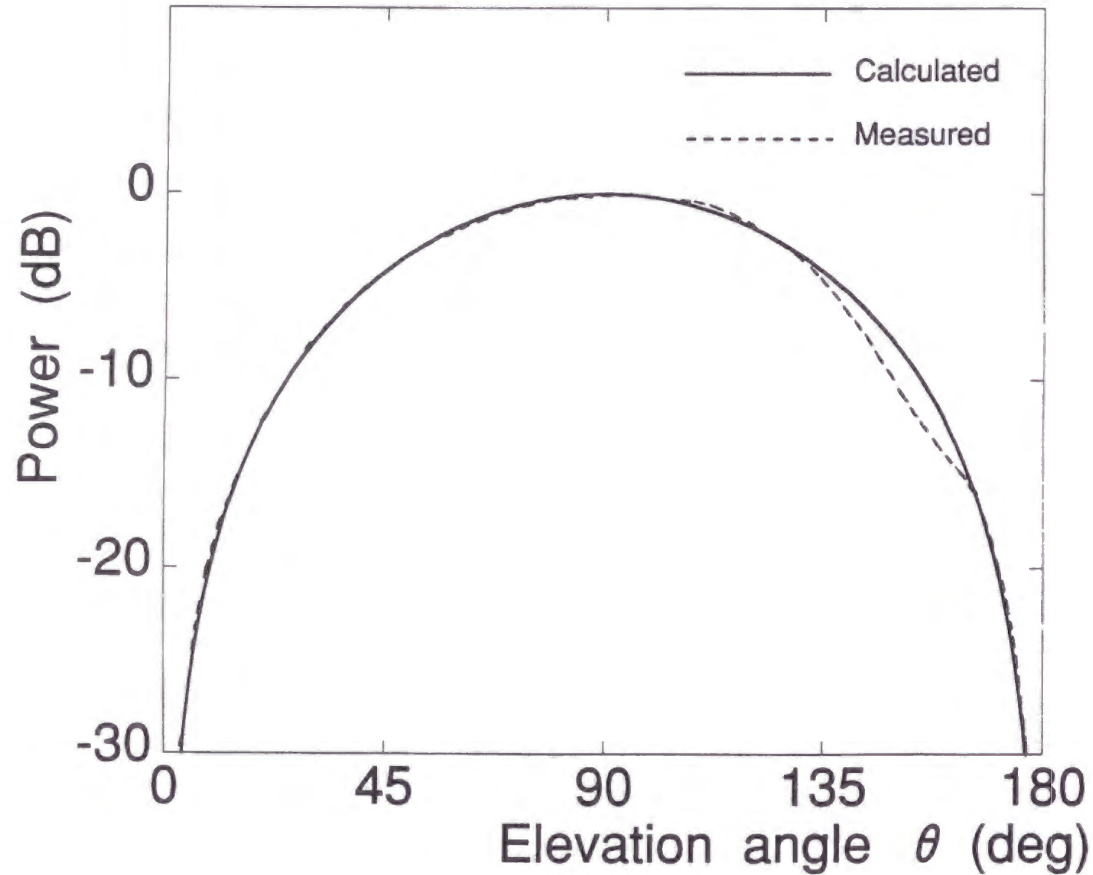
Figure 2.8: Calculated and measured radiation pattern of ECCD, where the parameters are the same as those in Fig.2.6.

2.5 Array performance

ECCD array antenna with n radiating elements is analyzed by an equivalent circuit for collinear antennas [10][35][36][37] shown in Fig.2.9. The feeding point of the array is located at the distance d_0 measured from the first radiating element. The end of the feeding coaxial cable, which is located at the distance d_n from the last radiating element, is terminated with a load of impedance Z_L. $d_m, (m = 1, 2, ..., n - 1)$ represents the spacing between m-th and $(m + 1)$-th radiating elements. k_f and Z_f represent the propagation constant and the characteristic impedance of the feeding coaxial cable, respectively. $Z_m, (m = 1, 2, ..., n)$ represents the self impedance of m-th radiating element which is calculated as follows:

$$Z_m = 1/Y_m, \tag{2.114}$$

where Y_m stands for the self admittance of m-th radiating element calculated by (2.80).

The input impedance Z_{in} of the array antenna is calculated by using the F-matrices F_m^Z and F_m, $(m = 1, 2, ..., n)$ of the equivalent circuit as follows:

$$Z_{in} = \frac{V}{I}, \tag{2.115}$$

$$\begin{pmatrix} V \\ I \end{pmatrix} = F_0 F_1^Z F_1 F_2^Z F_2 \cdots F_{n-1} F_n^Z F_n \begin{pmatrix} V_L \\ I_L \end{pmatrix}, \tag{2.116}$$

$$V_L = Z_L I_L, \tag{2.117}$$

$$F_m^Z = \begin{pmatrix} 1 & Z_m \\ 0 & 1 \end{pmatrix}, \tag{2.118}$$

$$F_m = \begin{pmatrix} \cos\theta_m & -iZ_f \sin\theta_m \\ (-i/Z_f)\sin\theta_m & \cos\theta_m \end{pmatrix}, \tag{2.119}$$

$$\theta_m = k_f d_m, \tag{2.120}$$

where V, I and V_L, I_L represent the voltage and current at the feeding port and those at the termination, respectively, F_m^Z represents the F-matrix of the serial impedance Z_m, and the effect of length d_m of the feeding coaxial cable is contained in F_m. It is noted that

(2.117) is sufficient to determine (2.115) because $Z_{in}(V_L, I_L)$ in (2.115) depends only on the ratio of V_L to I_L. The voltage V_m and current I_m seen from the feed side at the m-th radiating element are given as follows:

$$\begin{pmatrix} V_m \\ I_m \end{pmatrix} = F_m^Z F_m F_{m+1}^Z F_{m+1} \cdots F_{n-1} F_n^Z F_n \begin{pmatrix} V_L \\ I_L \end{pmatrix}, \tag{2.121}$$

where $\Delta v_m = I_m Z_m$, $(m = 1, 2, ..., n)$ gives the array excitation distribution.
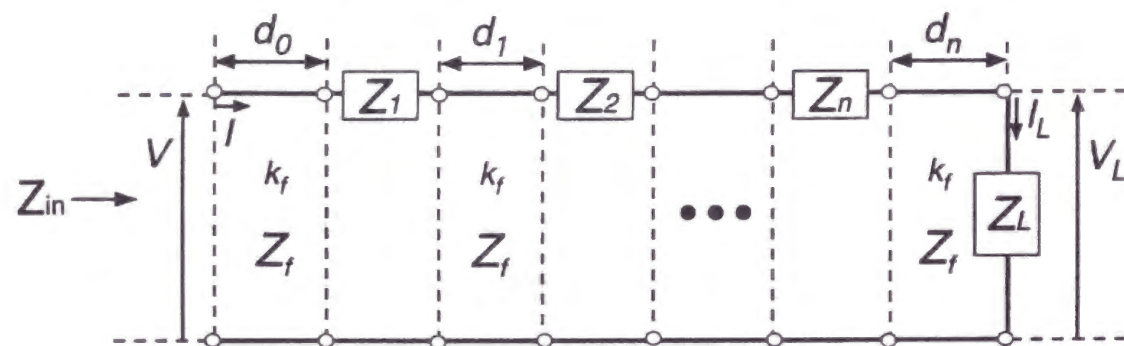
Figure 2.9: Equivalent circuit for ECCD array antenna.

2.6 Fabrication and measurements

A four element array antenna as shown in Fig.2.10 has been fabricated. The antenna is designed to have a uniform aperture field distribution. The parameters of the radiating elements are all identical to those of Figs.2.6 and 2.8 in the previous sections. The inner and outer radii of the feeding coaxial cable are $0.0026\lambda_{f0}$ and $0.0085\lambda_{f0}$, respectively. The cable is filled with dielectric material of dielectric constant $\varepsilon_r = 2.0$. The spacing d_1, d_2, and d_3 between the radiating elements are all identical to $0.71\lambda_{f0}$ which corresponds to $1\lambda_g$, where $\lambda_g = \lambda_{f0}/\sqrt{\varepsilon_r}$. The feeding coaxial cable is open ended. The distance d_4 is $(3/4)\lambda_g$ between the feeding point of the last radiating element and the open end of the cable. Near the feeding point of the array, an impedance matching section is formed. The section consists of a quarter wavelength impedance transformer with a coaxial cable. The impedance matching is carried out as follows: By varying the distance d_0 between the feeding point of the array and that of the first radiating element (see Fig.2.10), the imaginary part of Z_{in} can be canceled, where Z_{in} is calculated by (2.115). Now we have $Z_{in} = Z_r = $ real. The characteristic impedance Z_t of a quarter wavelength impedance transformer is determined by $Z_t = \sqrt{Z_r Z_f}$ to realize the matching, where Z_f is the characteristic impedance of the feeding coaxial cable. The designed parameters of the transformer are as follows: The inner and outer radii of the coaxial cable are $0.0026\lambda_{f0}$ and $0.010\lambda_{f0}$, respectively, and the length of the coaxial cable is $(1/4)\lambda_{f0}$ where $\varepsilon_r = 1$ inside, and $d_0 = 0.44\lambda_g$. Figure 2.11 shows a comparison between calculated and measured values of the return loss of the fabricated array, where the input impedance is designed to be matched at f_0. The correspondence between the two values is considered to be fair, however, not negligible disagreements are observed. The phenomenon is considered to be due to the following reasons: First, the mutual couplings are neglected between the radiating elements outside the feeding cable. Second, the region near the open end of the

feeding coaxial cable is simply modeled by the transmission line model in Fig.2.10 , and some treatments, *e.g.* inclusion of radiation effects, may be needed. Finally, more precise modeling of the transition between the radiating element and the feeding coaxial cable is considered to be important to improve the correspondence in Fig.2.11 as well as those in Fig.2.6. Figure 2.12 shows the radiation characteristics of the array. The efficiency of the antenna, measured gain versus calculated directive gain, is 91%. A good omnidirectional pattern in Azimuth (Az) angles as well as a uniform aperture field illumination in Elevation (El) angles is observed.
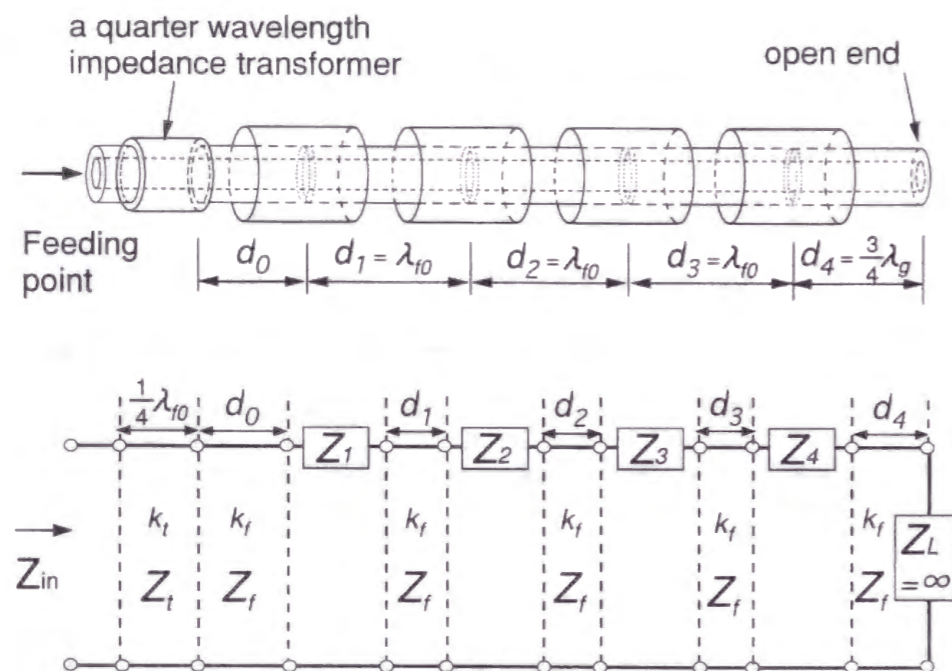
Figure 2.10: Geometry and equivalent circuit of a prototype four-element ECCD array antenna, where the parameters of radiating elements are the same as those in Fig.2.6, $\varepsilon_r = 2$ inside the feeding coaxial cable except in the quarter wavelength impedance transformer where $\varepsilon_r = 1$, the inner and outer radii of the transformer are $0.0026\lambda_{f0}$ and $0.010\lambda_{f0}$, respectively, and $d_0 = 0.44\lambda_g$.
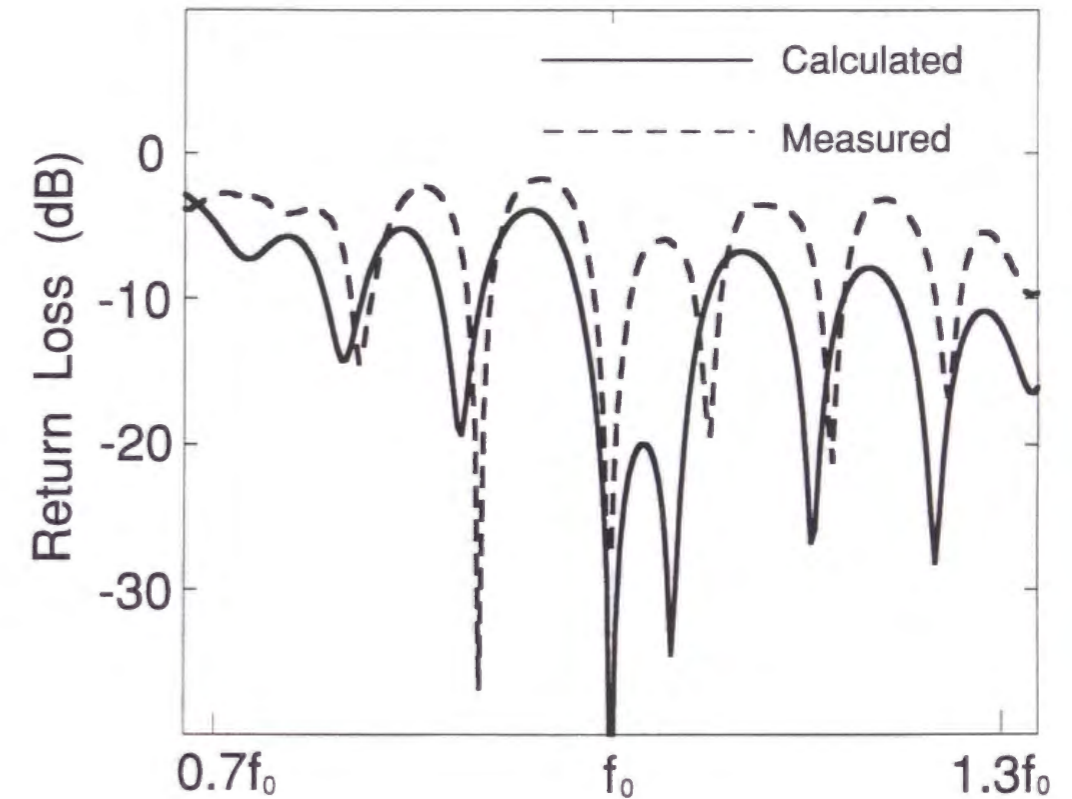
Figure 2.11: Return loss (power) of ECCD array antenna in Fig.2.10. The antenna is designed to be matched at f_0.
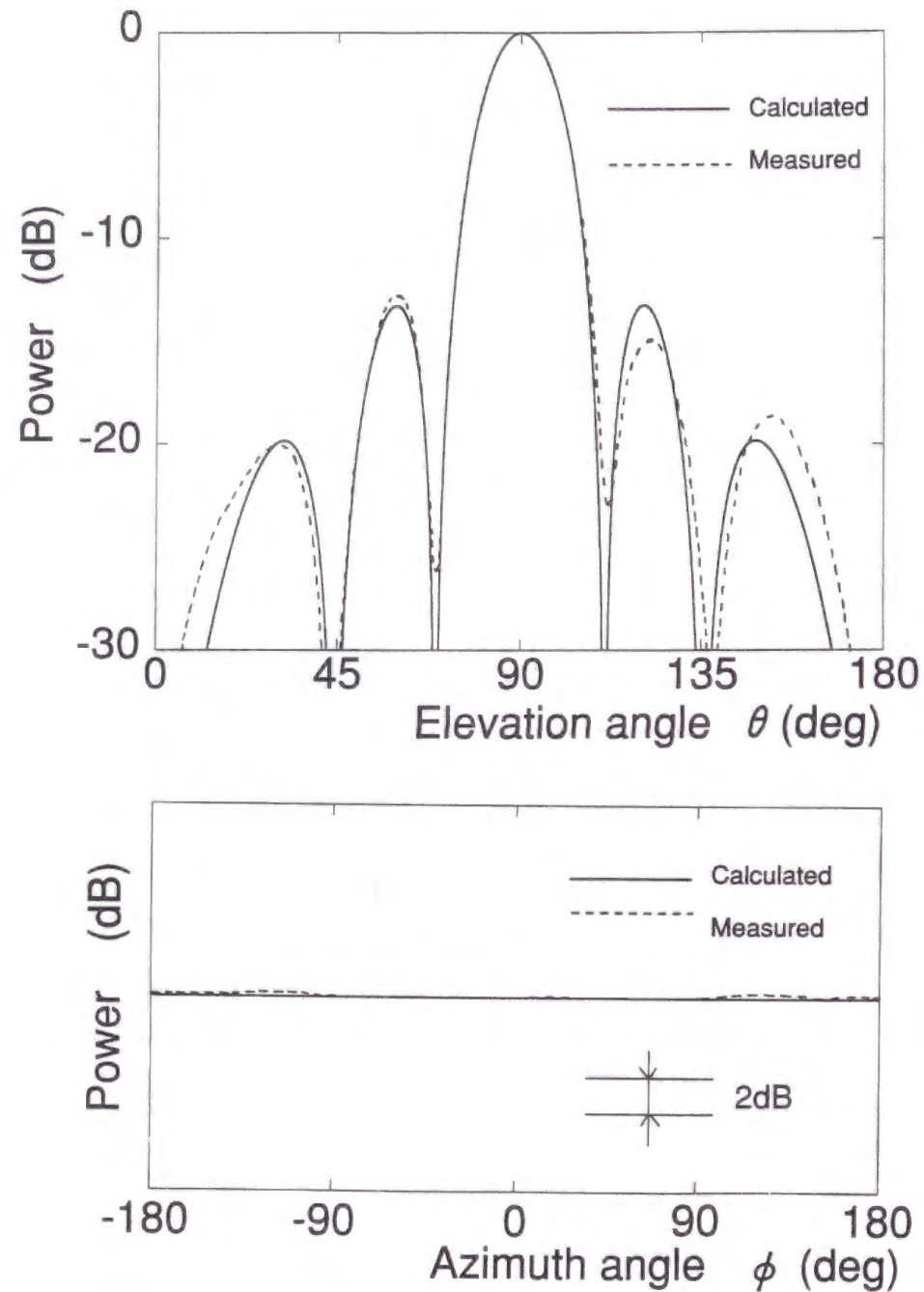
Figure 2.12: Radiation characteristics of the four-element ECCD array antenna in Fig.2.10, where the angles θ and ϕ are defined in Fig.2.7.

2.7 Summary

A design procedure is developed for a newly proposed collinear antenna array called the electromagnetically coupled coaxial dipole array antenna. The antenna has an advantage of structural simplicity suitable for manufacturing due to a novel use of an electromagnetically coupled feed. To model the edge of the radiating element, Wiener-Hopf analysis is carried out for the TEM mode reflection coefficient of a coaxial cable which has a semi-infinite outer conductor. The analysis deals with an exact solution as well as a simple approximate formula which is valid if the radius of the coaxial cable is much smaller than the operating wavelength. Comparison between values of the exact and the approximate formula is made with good correspondence. The approximate formula is utilized to calculate the input admittance of the radiating element, where the multiple reflections from the edges are taken into consideration. The dominant term of the input admittance allows physical inspection with resemblance to two coaxial cable ended by the reflection coefficients, connected and fed at the center. Comparison between calculated and measured values of S-parameters supports the theory. An analysis of radiation pattern of radiating element is carried out with an integral equation formalism by using the Green's functions of a perfectly conducting circular cylinder. Use of sinusoidal expansion function allows analytical evaluation of integrals in the Galerkin's method. The calculated and measured radiation patterns are in good agreement. To model the array antenna including feeding structure, an equivalent circuit is introduced as serial connection of the self impedances of the radiating elements. A procedure for matching is introduced with the modeling of the matching section. Fabrication and measurement of a prototype array antenna support the theory.

An efficient design procedure can be implemented with the analytical modeling as well as simple formulas for the radiating element developed in this chapter. The antenna is

suited for basestation antennas for mobile communication systems which require omni-directional patterns. Applications are also expected for other systems such as boundary layer radars.

Chapter 3

Equivalent Susceptance of a Circular Iris in a Parallel Plate Waveguide

3.1 Introduction

In this chapter, analytical formulations are developed for the parallel plate region with an application to a circular iris in a parallel plate waveguide [38].

The iris in a parallel plate waveguide is considered to be one of the canonical geometries of waveguide component with its applications to feeding structures of antenna arrays. A number of studies have been reported [3][39][40], however they are limited to the shape of linear iris. The circular iris in a parallel plate waveguide has a suitable geometry to realize the matching of the feeding probe in a waveguide. In this case, the effect of the curvature should be included for the design procedures, where approximate applications of the formula for the linear iris may give some errors. To obtain accurate modeling of the feeding structure by using the equivalent circuit approach, the corresponding formula is desired for the equivalent susceptance in the case that the TEM mode cylindrical wave is incident from the center.

This chapter treats the problem by using modal analysis of the parallel plate region

with the following organization of sections.

In Section 3.2, a simple approximate formula is obtained by using the variational method by Schwinger [3][40], where the theory is generalized to the cylindrical wave incidence. The previously known formula for an equivalent susceptance of the linear iris [3][39][40] is recovered when the radius of the circular iris is sufficiently larger than the wavelength.

In Section 3.3, an exact integral equation is formulated with respect to unknown currents on the surface of the circular iris. In the formulation, the Green's function of rotationally symmetric currents in the parallel plate waveguide with a perfectly absorbing dummy load at the center is introduced and its derivation is described. The integral equation is solved by the Galerkin's method with a class of sinusoidal expansion functions. The equivalent susceptance is expressed by using the calculated currents.

In Section 3.4, a comparison is made between the values calculated by the approximate formula and the Galerkin's method. The correspondence between them shows good agreement.

In Section 3.5, a summary of this chapter is given.

3.2 Approximate formula for equivalent susceptance

Consider a circular iris of infinitesimal thickness as shown in Fig.3.1 with a radius d and a height l in a parallel plate waveguide of a height $h < \lambda/2$, where λ is an operating wavelength such that the TEM mode is the only propagation mode. To facilitate an equivalent circuit correspondence, where normally the two ends of the equivalent circuit are terminated with the characteristic impedance of the feed line or the dummy load, a perfectly absorbing dummy load is placed at the center of the circular iris which is chosen to be the origin of the cylindrical coordinate system. With this scheme, for example the effect of feed region can be treated by using appropriate equivalent circuits for feeding probes [41]. With an introduction of unknown coefficients $\{a_n\}_{n=0,1,2,\ldots}$, $\{b_n\}_{n=0,1,2,\ldots}$, R, and T, the z-component of the electric field E_z and the ϕ-component of the magnetic field H_ϕ inside the waveguide are expressed as follows, where $e^{j\omega t}$ dependence is assumed for the fields:

$$E_z = a_0 \left\{ \frac{H_0^{(2)}(k\rho)}{H_0^{(2)}(kd)} + R\frac{H_0^{(1)}(k\rho)}{H_0^{(1)}(kd)} \right\} + \sum_{n=1}^{\infty} a_n \frac{H_0^{(1)}(\kappa_n\rho)}{H_0^{(1)}(\kappa_nd)} \cos\frac{n\pi z}{h}, \qquad (3.1)$$

$$H_\phi = jY_0a_0 \left\{ \frac{H_1^{(2)}(k\rho)}{H_0^{(2)}(kd)} + R\frac{H_1^{(1)}(k\rho)}{H_0^{(1)}(kd)} \right\} + j\sum_{n=1}^{\infty} Y_n a_n \frac{H_1^{(1)}(\kappa_n\rho)}{H_0^{(1)}(\kappa_nd)} \cos\frac{n\pi z}{h}, \qquad (3.2)$$

$$(0 < \rho \le d),$$

and

$$E_z = a_0 T \frac{H_0^{(2)}(k\rho)}{H_0^{(2)}(kd)} + \sum_{n=1}^{\infty} b_n \frac{H_0^{(2)}(\kappa_n\rho)}{H_0^{(2)}(\kappa_nd)} \cos\frac{n\pi z}{h}, \qquad (3.3)$$

$$H_\phi = jY_0 T a_0 \frac{H_1^{(2)}(k\rho)}{H_0^{(2)}(kd)} + j\sum_{n=1}^{\infty} Y_n b_n \frac{H_1^{(2)}(\kappa_n\rho)}{H_0^{(2)}(\kappa_nd)} \cos\frac{n\pi z}{h}, \qquad (3.4)$$

$$(\rho \ge d),$$
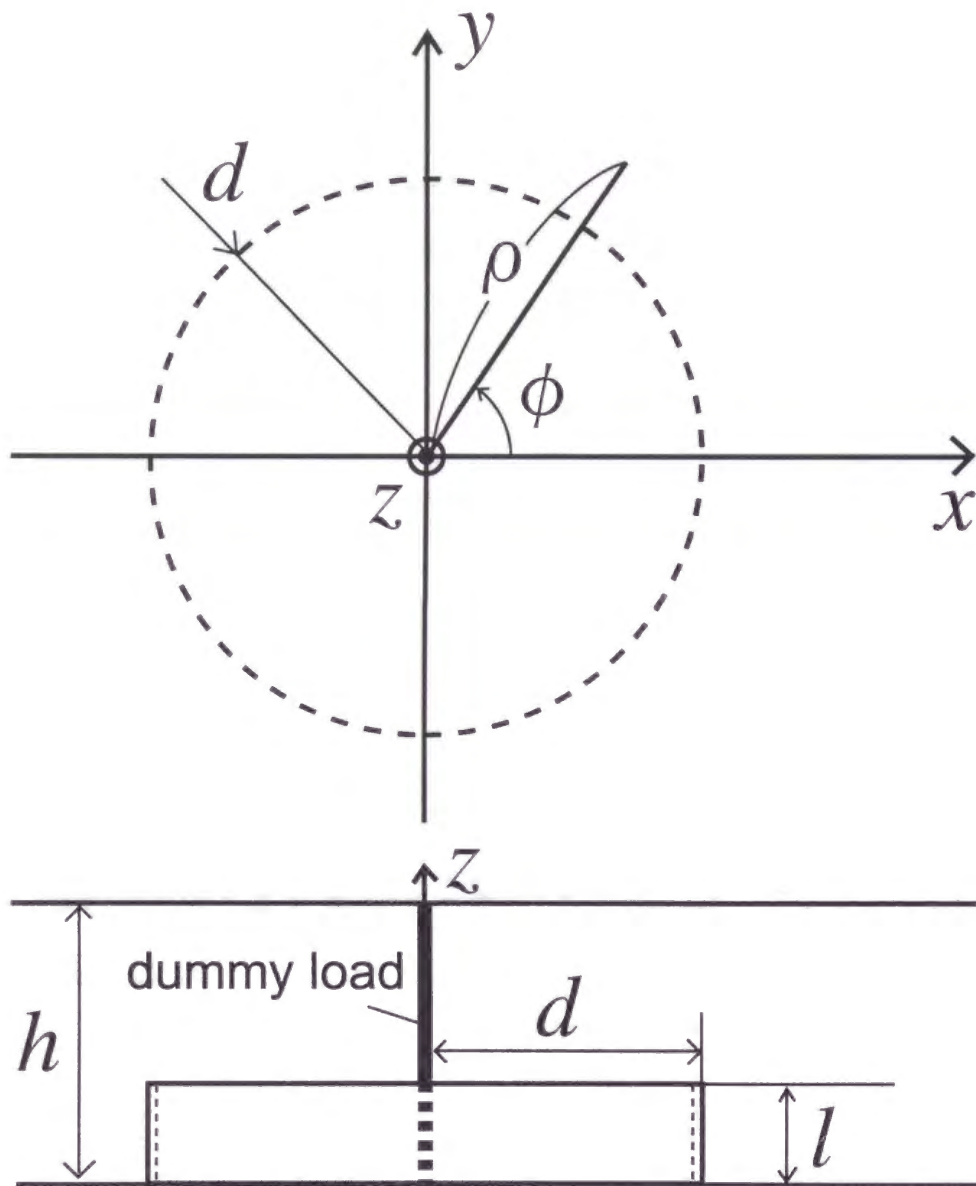
Figure 3.1: The circular iris in a parallel plate waveguide.

$$k = \frac{2\pi}{\lambda} = \omega\sqrt{\mu_0\varepsilon_0}, \tag{3.5}$$

$$\kappa_n^2 = k^2 - \left(\frac{n\pi}{h}\right)^2, \quad (\text{Im}(\kappa_n) \leq 0), \quad \kappa_0 = k,$$

$$\kappa_n = -j\gamma_n = -j\sqrt{\left(\frac{n\pi}{h}\right)^2 - k^2}, \tag{3.6}$$

$$Y_0 = \sqrt{\frac{\varepsilon_0}{\mu_0}} = \frac{1}{\eta}, \qquad Y_n = \frac{k}{\kappa_n}Y_0, \tag{3.7}$$

where ε_0 and μ_0 are permittivity and permeability of the free space, respectively.

For the convenience of the analysis, the reflection coefficient R of the dominant TEM mode is defined in a special form as follows:

$$V(\rho) = V'^+ \frac{H_0^{(2)}(k\rho)}{H_0^{(2)}(kd)} + V'^- \frac{H_0^{(1)}(k\rho)}{H_0^{(1)}(kd)}, \tag{3.8}$$

$$R = \frac{V'^-}{V'^+}, \tag{3.9}$$

where $V(\rho)$ is the modal voltage of the dominant TEM mode in the radial line, and V^+ and V^- represent the amplitudes of traveling waves in the positive and the negative directions with respect to ρ, respectively. A common definition of the voltage reflection coefficient R_o in the equivalent circuit for the radial line is taken as follows [39]:

$$V(\rho) = V^+ H_0^{(2)}(k\rho) + V^- H_0^{(1)}(k\rho), \tag{3.10}$$

$$R_o = \frac{V^-}{V^+}. \tag{3.11}$$

Because the following simple relation exists between R and R_o, the present definition applies without a loss of generality:

$$R_o = \frac{H_0^{(1)}(kd)}{H_0^{(2)}(kd)}R. \tag{3.12}$$

In the following analysis, we generalize the variational method by Schwinger [3][40] from the case that the plane wave is incident to the linear iris to the case that the cylindrical wave is incident to the circular iris. The boundary conditions about the continuity

of E_z and H_ϕ at $\rho = d$ give the following equations:

$$
\begin{aligned}
E_z(\rho = d) &= E(z), \\
&= a_0(1+R) + \sum_{n=1}^{\infty} a_n \cos \frac{n\pi z}{h}, \\
&= a_0 T + \sum_{n=1}^{\infty} b_n \cos \frac{n\pi z}{h}, \qquad (0 \le z \le h), \quad (3.13)
\end{aligned}
$$

$$
\begin{aligned}
H_\phi(\rho = d) &= jY_0 a_0 \left\{ \frac{H_1^{(2)}(kd)}{H_0^{(2)}(kd)} + R \frac{H_1^{(1)}(kd)}{H_0^{(1)}(kd)} \right\} + j \sum_{n=1}^{\infty} Y_n a_n \frac{H_1^{(1)}(\kappa_n d)}{H_0^{(1)}(\kappa_n d)} \cos \frac{n\pi z}{h}, \\
&= jY_0 T a_0 \frac{H_1^{(2)}(kd)}{H_0^{(2)}(kd)} + j \sum_{n=1}^{\infty} Y_n b_n \frac{H_1^{(2)}(\kappa_n d)}{H_0^{(2)}(\kappa_n d)} \cos \frac{n\pi z}{h}, \quad (l < z \le h), \ (3.14)
\end{aligned}
$$

where a function $E(z)$ is defined as E_z at $\rho = d$ in (3.13), and the notation will be used in the following analysis. After multiplying (3.13) by a class of functions $\{\cos(n\pi z/h)\}_{n=0,1,2,\ldots}$ and integrating them with respect to z in the domain $0 \le z \le h$, we have the following relations:

$$
a_0(1+R) = a_0 T = \frac{1}{h} \int_0^h dz E(z), \tag{3.15}
$$

$$
a_n = b_n = \frac{2}{h} \int_0^h dz E(z) \cos \frac{n\pi z}{h}. \tag{3.16}
$$

By using (3.15) and (3.16), the coefficients T and b_n in (3.14) can be eliminated with the following result:

$$
\frac{2Y_0 a_0 R}{D(kd)} + 2 \sum_{n=1}^{\infty} \frac{Y_n a_n}{D(\kappa_n d)} \cos \frac{n\pi z}{h} = 0, \qquad (l < z \le h), \tag{3.17}
$$

$$
D(z) = \frac{\pi z}{2} H_0^{(1)}(z) H_0^{(2)}(z), \tag{3.18}
$$

$$
\lim_{|z| \to \infty} D(z) = 1, \tag{3.19}
$$

where (3.19) is deduced with the aid of the following formula:

$$
H_0^{(1)}(z) \sim \sqrt{\frac{2}{\pi z}} e^{j(z - \pi/4)} \left\{ 1 - \frac{j}{8z} + O\left(\frac{1}{z^2}\right) \right\}, \qquad (|z| \to \infty). \tag{3.20}
$$

By using the relations of (3.15) and (3.16), a_0 and a_n in (3.17) are replaced with the integrals of $E(z)$, and the following relation is obtained:

$$
-\frac{2R}{1+R} \cdot \frac{Y_0}{D(kd)} \int_0^h dz' E(z') = 4 \sum_{n=1}^{\infty} \frac{Y_n}{D(\kappa_n d)} \cos \frac{n\pi z}{h} \cdot \int_0^h dz' E(z') \cos \frac{n\pi z'}{h},
$$
$$
(l < z \le h). \tag{3.21}
$$

The first factor in the left-hand side of the above formula corresponds to a shunt susceptance B in the equivalent circuit for the radial line [39] as shown in Fig.3.2 where k is the propagation constant of the dominant TEM mode and the characteristic impedance Z_c of the radial line at $\rho = d$ is normalized to unity. We summarize here the relations for the circuit in Fig.3.2 as follows [3]:

$$
jB = -\frac{2R}{1+R}, \tag{3.22}
$$

$$
R = \frac{1 - Y_{in}}{1 + Y_{in}} = -\frac{jB}{2 + jB}, \tag{3.23}
$$

inner side of the iris   **outer side of the iris**
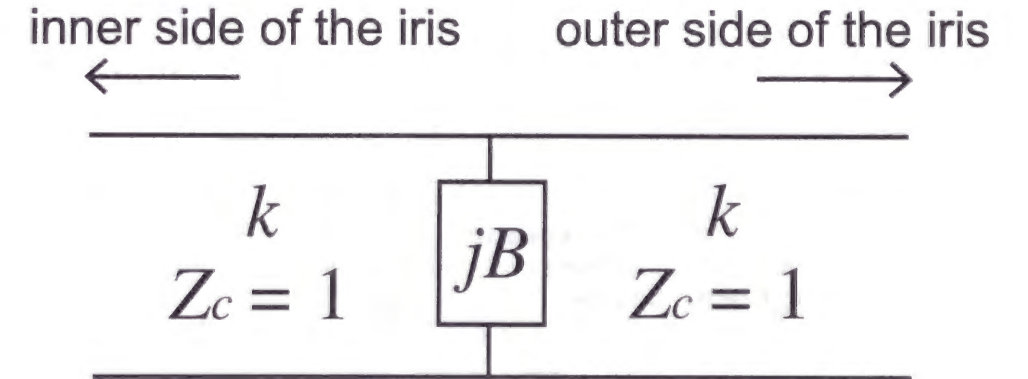
Figure 3.2: The equivalent circuit for a circular iris in a radial line.

where Y_{in} is the normalized input admittance of the circuit. After multiplying both sides of (3.21) by $E(z)$ and integrating them with respect to z in the domain $0 \le z \le h$, the susceptance B is expressed by using (3.22) with the following result:

$$B = \frac{4k \sum_{n=1}^{\infty} \frac{1}{\gamma_n D(\kappa_n d)} \left\{ \int_0^h dz E(z) \cos \frac{n\pi z}{h} \right\}^2}{\frac{1}{D(kd)} \left\{ \int_0^h dz' E(z') \right\}^2}. \tag{3.24}$$

We show that the above formula is stationary about its correct value with respect to the first order variation δ of $E(z)$. From (3.24) we have,

$$\begin{aligned}
\delta \left[\frac{1}{D(kd)} \left\{ \int_0^h dz E(z) \right\}^2 B \right] &= \frac{2B}{D(kd)} \int_0^h dz' E(z') \cdot \int_0^h dz \delta E(z) \\
&\quad + \frac{1}{D(kd)} \left\{ \int_0^h dz E(z) \right\}^2 \delta B, \\
&= 8k \sum_{n=1}^{\infty} \frac{1}{\gamma_n D(\kappa_n d)} \int_0^h dz' E(z') \cos \frac{n\pi z'}{h} \\
&\quad \cdot \int_0^h dz \delta E(z) \cdot \cos \frac{n\pi z}{h}.
\end{aligned} \tag{3.25}$$

(3.25) is rearranged as follows:

$$\begin{aligned}
\frac{1}{D(kd)} \left\{ \int_0^h dz E(z) \right\}^2 \delta B &= \frac{2}{Y_0 j} \int_0^h dz \delta E(z) \cdot \left\{ \frac{2R}{1+R} \cdot \frac{Y_0}{D(kd)} \int_0^h dz' E(z') \right. \\
&\quad \left. + 4 \sum_{n=1}^{\infty} \frac{Y_n}{D(\kappa_n d)} \cos \frac{n\pi z}{h} \cdot \int_0^h dz' E(z') \cos \frac{n\pi z'}{h} \right\}, \\
&= 0,
\end{aligned} \tag{3.26}$$

where we have used (3.21) in the last equation. Because the factor before δB in the first equation of (3.26) is non-zero, we have,

$$\delta B = 0. \tag{3.27}$$

Next we derive an approximate formula for B. From (3.20) the following asymptotic expansion is obtained:

$$\frac{1}{\gamma_n D(\kappa_n d)} = \frac{1}{\gamma_n} + \frac{1}{64 \gamma_n^3 d^2} + O\left(\frac{1}{\gamma_n^4}\right), \qquad (\gamma_n \to \infty). \tag{3.28}$$

48

Moreover, γ_n is expanded as follows:

$$\frac{1}{\gamma_n} = \frac{h}{n\pi} + O\left(\frac{1}{n^3}\right), \qquad (n \to \infty). \tag{3.29}$$

By using the above formulas, the partial terms in (3.24) is approximated as follows:

$$\sum_{n=1}^{\infty} \frac{1}{\gamma_n D(\kappa_n d)} \cos \frac{n\pi z}{h} \cdot \cos \frac{n\pi z'}{h} \simeq \frac{h}{\pi} \sum_{n=1}^{\infty} \frac{1}{n} \cos \frac{n\pi z}{h} \cdot \cos \frac{n\pi z'}{h}. \tag{3.30}$$

The following sum formula [3] is known:

$$\sum_{n=1}^{\infty} \frac{1}{n} \cos \frac{n\pi z}{h} \cdot \cos \frac{n\pi z'}{h} = \ln \sec \frac{\pi l}{2h} + \sum_{n=1}^{\infty} \frac{1}{n} \cos n\theta \cdot \cos n\theta', \tag{3.31}$$

where θ is a monotone increasing function of z in the domain $l \le z \le h$ with its range $0 \le \theta \le \pi$. θ satisfies the following relation:

$$\cos \frac{\pi z}{h} = -\sin^2 \frac{\pi l}{2h} + \cos^2 \frac{\pi l}{2h} \cdot \cos \theta. \tag{3.32}$$

θ' is defined with respect to z' in the same way as the above. By using (3.30) and (3.31), (3.24) is approximated as follows:

$$B \simeq \frac{4kh D(kd)}{\pi} \cdot \frac{\int_0^\pi d\theta \int_0^\pi d\theta' F(\theta) F(\theta') L(\theta, \theta')}{\left\{ \int_0^\pi d\theta'' F(\theta'') \right\}^2}, \tag{3.33}$$

$$L(\theta, \theta') = \ln \sec \frac{\pi l}{2h} + \sum_{n=1}^{\infty} \frac{1}{n} \cos n\theta \cdot \cos n\theta', \tag{3.34}$$

$$F(\theta) = E(z) \frac{dz}{d\theta}. \tag{3.35}$$

For the first order approximation, we put $F = $ const. in (3.33). Now we have the following approximate formula for the equivalent susceptance B:

$$B \simeq \frac{4kh D(kd)}{\pi} \ln \sec \frac{\pi l}{2h}. \tag{3.36}$$

If the radius d of the circular iris is much larger than the operating wavelength, (3.36) recovers the previously known formula for the linear iris [39][40], i.e. $D(kd) \to 1$ in this case if $kd \to \infty$ from (3.19).

49

3.3 Integral equation formalism for equivalent susceptance

In this section, a numerical solution is developed through an exact integral equation formalism for the equivalent susceptance. The result will be applied later to examine the validity of the approximate formula (3.36) derived in the previous section.

First of all, we construct the Green's function for E_z with respect to a z-directed rotationally symmetric electric current element J_z with a radius ρ' as shown in Fig.3.3, where the geometry of the parallel plate waveguide is identical to that of Fig.3.1. The present structure is adequately analyzed by a vector potential which has only non-zero component in z [3], and we write it A_z. Non-zero components of the electric field inside the waveguide are expressed as follows:

$$E_\rho = \frac{1}{j\omega_0\mu_0\varepsilon_0}\frac{\partial^2 A_z}{\partial z\partial\rho}, \tag{3.37}$$

$$E_z = \frac{1}{j\omega_0\mu_0\varepsilon_0}\left(\frac{\partial^2}{\partial z^2}+k^2\right)A_z, \tag{3.38}$$

where E_ρ is the ρ-component of the electric field. We define the Green's function $G^{(e)}$ for A_z with respect to J_z as follows:

$$A_z(\rho,z) = \mu_0\int dz'G^{(e)}(\rho,z|\rho',z')J_z(z'). \tag{3.39}$$

$G^{(e)}$ satisfies the following equation:

$$(\nabla^2+k^2)G^{(e)}(\rho,z|\rho',z') = -\delta(\rho-\rho')\delta(z-z'), \tag{3.40}$$

$$\left.\frac{\partial G^{(e)}}{\partial z}\right|_{z=0,h} = 0. \tag{3.41}$$
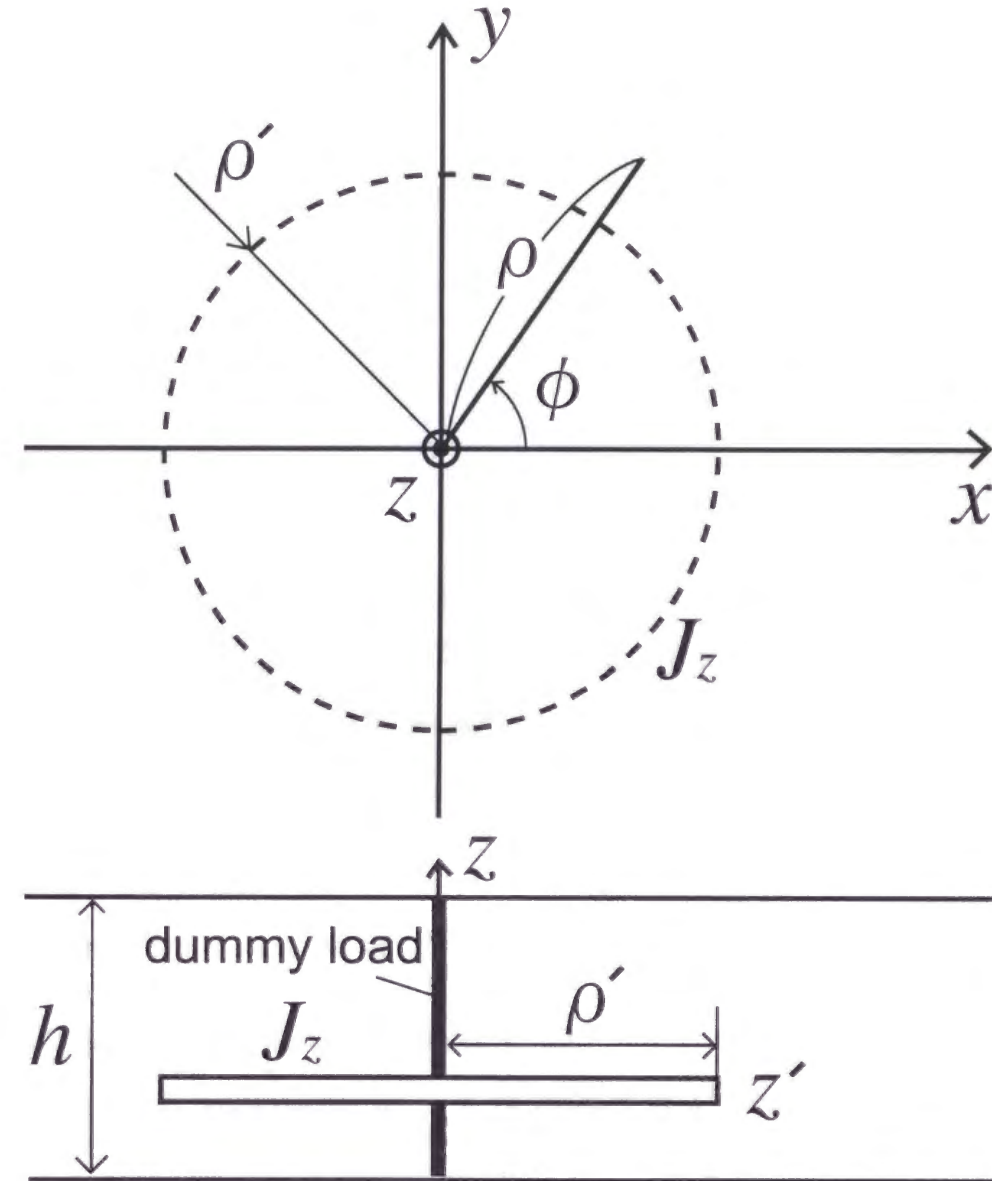
Figure 3.3: Rotationally symmetric electric current element in a parallel plate waveguide with a dummy load at the center.

In the above formulas, (3.41) is derived thorough the boundary conditions for E_ρ on the upper and lower surfaces of the parallel plate waveguide with a postulate that $G^{(e)}$ is separable with respect to ρ and z. Then we assume $G^{(e)}$ in the following form:

$$G^{(e)}(\rho, z|\rho', z') = \sum_{n=0}^{\infty} g_n(\rho, \rho') f_n(z') \cos\frac{n\pi z}{h}, \tag{3.42}$$

where g_n and f_n are unknown functions. From (3.40) and (3.42), the following equations are obtained:

$$\left\{\frac{1}{\rho}\frac{d}{d\rho}\left(\rho\frac{d}{d\rho}\cdot\right) + \kappa_n^2\right\} g_n(\rho, \rho') = -\delta(\rho - \rho'), \tag{3.43}$$

$$\sum_{n=0}^{\infty} f_n(z') \cos\frac{n\pi z}{h} = \delta(z - z'). \tag{3.44}$$

We construct a solution of (3.43). As the center of the parallel plate waveguide is loaded with a perfectly absorbing dummy load, no traveling wave exits in the positive radial direction of ρ in the domain $0 \leq \rho \leq \rho'$. In $\rho \geq \rho'$, the fields are decreased to zero as $\rho \to \infty$, or the radiation condition [3] is satisfied. Homogeneous solutions of (3.43) are given by cylindrical functions of the zero-th order under the condition (3.6) as well as the above statements. Thus we have g_n as follows:

$$g_n(\rho, \rho') = \begin{cases} A H_0^{(1)}(\kappa_n \rho), & (\rho \leq \rho'), \\ B H_0^{(2)}(\kappa_n \rho), & (\rho \geq \rho'). \end{cases} \tag{3.45}$$

The following conditions are obtained by the continuity of E_z at $\rho = \rho'$ and the condition given by integrating (3.43) with respect to ρ in an infinitesimal domain $(\rho' - \Delta, \rho' + \Delta)$, $(\Delta \to +0)$:

$$g_n(\rho' + \Delta, \rho') - g_n(\rho' - \Delta, \rho') = 0, \qquad (\Delta \to +0), \tag{3.46}$$

$$\frac{d}{d\rho} g_n(\rho' + \Delta, \rho') - \frac{d}{d\rho} g_n(\rho' - \Delta, \rho') = -1, \qquad (\Delta \to +0). \tag{3.47}$$

From (3.45) to (3.47), g_n is constructed as follows:

$$g_n(\rho, \rho') = \frac{\pi\rho'}{4j} H_0^{(1)}(\kappa_n \rho_<) H_0^{(2)}(\kappa_n \rho_>), \tag{3.48}$$

52

where $\rho_> = \rho$ and $\rho_< = \rho'$ if $\rho \geq \rho'$, and in the case of $\rho < \rho'$, $\rho_> = \rho'$ and $\rho_< = \rho$. Multiplying both sides of (3.44) by $\{\cos(n\pi z/h)\}_{n=0,1,2,\ldots}$ and integrating them with respect to z in the domain $0 \leq z \leq h$, f_n is constructed with the following result:

$$f_n(z) = \frac{\epsilon_n}{h}\cos\frac{n\pi z}{h}, \tag{3.49}$$

$$\epsilon_n = \begin{cases} 1, & (n = 0), \\ 2, & (n \geq 1). \end{cases} \tag{3.50}$$

From (3.42), (3.48), and (3.49) we have $G^{(e)}$ as follows:

$$G^{(e)}(\rho, z|\rho', z') = \frac{\pi\rho'}{4hj}\sum_{n=0}^{\infty}\epsilon_n H_0^{(1)}(\kappa_n\rho_<)H_0^{(2)}(\kappa_n\rho_>)\cos\frac{n\pi z}{h}\cdot\cos\frac{n\pi z'}{h}. \tag{3.51}$$

From (3.38), (3.39), and (3.51), the desired Green's function G for E_z with respect to J_z is finally constructed as follows:

$$E_z(\rho, z) = \int dz' G(\rho, z|\rho', z') J_z(z'), \tag{3.52}$$

$$G(\rho, z|\rho', z') = -\frac{\pi\eta\rho'}{4kh}\sum_{n=0}^{\infty}\epsilon_n\kappa_n^2 H_0^{(1)}(\kappa_n\rho_<)H_0^{(2)}(\kappa_n\rho_>)\cos\frac{n\pi z}{h}\cdot\cos\frac{n\pi z'}{h}. \tag{3.53}$$

Now we analyze the scattering problem of the circular iris in Fig.3.1 by using the Green's function G in the above. Consider an incident TEM mode cylindrical wave E_z^i which has a non-zero component only in the z-axis as follows:

$$E_z^i = H_0^{(2)}(k\rho). \tag{3.54}$$

Let J_z be an induced current distribution on the surface of the circular iris for the scattering problem. The z-component of the scattered field E_z^s is calculated by using (3.52) with $\rho' = d$. Because of the boundary condition that the total tangent electric field on the surface of the circular iris is zero, we have the following integral equation with respect to J_z at $\rho = d$:

$$E_z^i + E_z^s = 0, \qquad (0 \leq z \leq l). \tag{3.55}$$

53

We use the Galerkin's method to solve (3.55). Let $\{c_\nu\}_{\nu=0,1,2,...}$ be a class of unknown coefficients and $\{\Psi_\nu\}_{\nu=0,1,2,...}$ be a class of expansion functions. J_z is expanded as follows:

$$J_z(z) = \sum_\nu c_\nu \Psi_\nu(z), \tag{3.56}$$

$$\Psi_\nu(z) = \begin{cases} \sin\left\{\frac{\pi}{2l}(2\nu-1)(z-l)\right\}, & (0 \le z \le l), \\ 0, & (l \le z \le h). \end{cases} \tag{3.57}$$

(3.55) is equivalent to the following in the Galerkin's sense:

$$\int_0^l dz \Psi_\lambda \cdot (E_z^i + E_z^s) = 0, \quad (\lambda = 0, 1, 2, ...). \tag{3.58}$$

After some calculation (3.58) reduces to the following linear equations with respect to $\{c_\nu\}_{\nu=0,1,2,...}$, and they can be approximately solved by truncation with finite terms.

$$\sum_\nu U_{\lambda\nu} c_\nu + H_0^{(2)}(kd) l F_{\lambda 0} = 0, \quad (\lambda = 0, 1, 2, ...), \tag{3.59}$$

$$U_{\lambda\nu} = -\frac{\eta \pi d}{4kh} \sum_{n=0}^\infty \epsilon_n (\kappa_n l)^2 H_0^{(1)}(\kappa_n d) H_0^{(2)}(\kappa_n d) F_{\lambda n} F_{\nu n}, \tag{3.60}$$

$$F_{mn} = \frac{1}{l} \int_0^l dz \Psi_m(z) \cos\frac{n\pi z}{h}, \tag{3.61}$$

$$= \begin{cases} -\frac{\dfrac{2}{\pi(2m-1)}\cos\dfrac{n\pi l}{h}}{1 - \left\{\dfrac{2nl}{(2m-1)h}\right\}^2}, & \left(\dfrac{2nl}{(2m-1)h} \ne 1\right), \\ \dfrac{(-1)^{m+1}}{2}, & \left(\dfrac{2nl}{(2m-1)h} = 1\right). \end{cases} \tag{3.62}$$

By using the determined coefficients $\{c_\nu\}_{\nu=0,1,2,...}$, the z-component E_z of the total electric field in $\rho \le d$ is calculated as follows:

$$E_z = E_z^i + E_z^s,$$

$$= H_0^{(2)}(k\rho) + R_o H_0^{(1)}(k\rho) + E_z^{HO}, \tag{3.63}$$

$$R_o = -\frac{\eta \pi l k d}{4h} H_0^{(2)}(kd) \sum_\nu F_{\nu 0} c_\nu, \tag{3.64}$$

where E_z^{HO} represents the term due to higher order modes with wavenumbers κ_n, $(n \ge 1)$. As R_o in (3.63) corresponds to that of (3.11), the susceptance B comparable to (3.36) is

obtained by using (3.12) and (3.22) with the following result:

$$B = \frac{\dfrac{\eta \pi l k d}{2hj} H_0^{(1)}(kd) \sum_m F_{m0} c_m}{1 - \dfrac{\eta \pi l k d}{4h} H_0^{(1)}(kd) \sum_n F_{n0} c_n}. \tag{3.65}$$

3.4 Validity of the approximate formula

In this section, validity of the approximated formula (3.36) for the susceptance B is examined by numerical calculations. Extensive numerical calculations show that in the range of $d > 0.02\lambda$, $0.02 < h < 0.48\lambda$, and $0.1 < l/h < 0.9$, the calculated values by the approximate formula agree with the exact values by the Galerkin's method within 5%. However, it must be noted that the uniform line current is applied as a source of incident wave in this idealized mathematical model, where the applied current is always uniform and invariant under the presence of the iris. Figure 3.4 shows typical calculated curves of B as a function of the height l of the circular iris shown in Fig.3.1 with $h = 0.4\lambda$ and $d = 0.3\lambda$. In Fig.3.4, the solid line represents the values by the approximate formula (3.36), and the broken line corresponds to the numerical solution (3.65) by the Galerkin's method developed in the previous section. Good agreement between them supports the validity of the approximate formula.
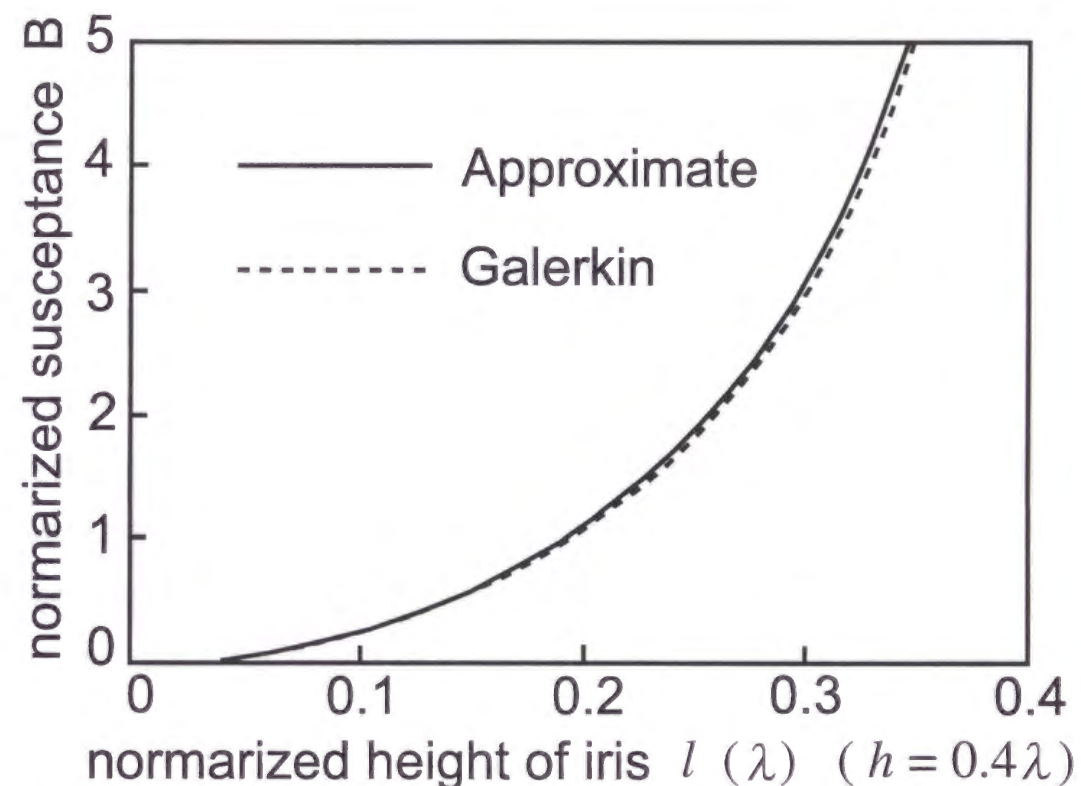
Figure 3.4: Calculated susceptance with the characteristic impedance of the radial line normalized to unity through the approximate formula (3.36) and numerical values (3.65) by the Galerkin's method, where the number of sinusoidal expansion functions for the current is 32 with 128 expansion modes of the Green's function.

3.5 Summary

Implementation of analytical modeling is investigated for parallel plate region with an application to the circular iris. By using modal expansions with respect to cylindrical harmonics, a variational expression of the equivalent susceptance is obtained for the equivalent circuit of the dominant TEM mode. The expression is stationary with respect to the first order variation of the electric field on the surface of the circular iris. By extending the method by Schwinger to the case of cylindrical harmonics expansions, a simple approximate closed form formula is obtained for the equivalent susceptance. The effect of the curvature of the circular iris is contained in a correction factor for the previously known formula for the linear iris. If the radius of the curvature is very large compared with the operating wavelength, the correction factor goes to unity, which recovers the result of the linear iris. For verification of the approximate formula, an exact integral equation is formulated by constructing the Green's function for circular current elements in the parallel plate waveguide loaded by a perfectly absorbing dummy load at the center. The Galerkin's method is used for numerical solution. Accuracy of the approximate formula is verified by comparison with the numerical solution.

The method developed in this chapter is considered to be a typical example for analytical modeling of the waveguide components used for the feeding structure of antenna arrays. As the derived circuit parameter is based on the solution of the boundary value problem, the accurate modeling is possible.

Chapter 4

Radial Line Planar Monopulse Antenna

4.1 Introduction

In this chapter, a design procedure is developed for a newly proposed planar antenna array, the Radial Line Planar Monopulse Antenna (RLPMA) as shown in Fig.4.1 [42]. The antenna is highly efficient because of a waveguide feed, and is capable of synthesizing monopulse Σ and Δ patterns by a novel use of a multiple port fed radial line. If the radial line is fed by two probes with in phase or out of phase excitations, monopulse Σ or Δ patterns, respectively, can be synthesized in one direction. If one desires a monopulse tracking operation in both azimuth and elevation angles, four feeding probes are used as shown in Fig.4.1.

There exit a number of the Radial Line Planar Antennas (RLPAs) [43]-[48]. The original art was performed by Goebels and Kelly [43] in 1961 as the annular slot array antenna fed by the radial line. Goto [44] proposed the Radial Line Slot Antenna (RLSA) in 1980 for Direct Broadcast from a Satellite (DBS) in Japan. Since then in collaboration with Ando *et al.* [45], extensive studies were carried out, and now RLSA is regarded as one of

the standard forms of planar antennas for DBS applications [49][50]. RLSAs have an advantage of structural simplicity, however, realization of uniform aperture field illumination with a high antenna efficiency is not an easy task. This is due to the following reasons: As radiation due to a reflected wave from the end of the radial line produces a cross polarized radiation when the antenna is operated in a circular polarization, a traveling wave feed of radiating slots must be employed, and this requires the slots near the termination to have infinite admittances coupled to the radial line if the loss free excitation condition is required. The difficulty has been relaxed by employing an approximate uniform [49] or the optimum non-uniform aperture field distribution [51] with a matching spiral near the termination.

Recently, other types of RLPAs have been proposed [46]-[48], using probes as a feeding structure of the radiating element. Nakano *et al.* [46] first proposed probe fed low profile helical antennas as the radiating elements, and further developed extremely low profile curl antennas [47]. Shibata *et al.* [48] used probe fed microstrip antennas as radiating elements. The probe fed RLPAs have an advantage that they can achieve a loss free uniform aperture field illumination because the excitation probes of the radiating elements can be fed by a standing wave in the radial line with a short circuited termination of its end. However at that moment, the probe fed RLPAs were only experimentally designed [46]-[48], and thus analytical studies have been expected to appear.

In the following sections, we investigate fundamental characteristics of RLPMA as well as an analytical procedure to achieve the uniform aperture field distribution of probe fed RLPAs.

In Section 4.2, the mutual coupling of probes in a radial line is analyzed by the EMF method, and experimental verification is given. The result obtained will be extensively used in the forthcoming sections.

In Section 4.3, a phenomenological analysis about fundamental characteristics of RLP-

MAs is presented, giving an understanding of why the monopulse patterns can be synthesized by RLPMAs.

In Section 4.4, a design procedure of a uniform aperture field distribution for RLPMA is proposed. This procedure is also applicable to the conventional probe fed RLPAs [46]-[48].

In Section 4.5, a design example as well as an experimental verification of RLPMA is described.

In Section 4.6, a summary of this chapter is given.
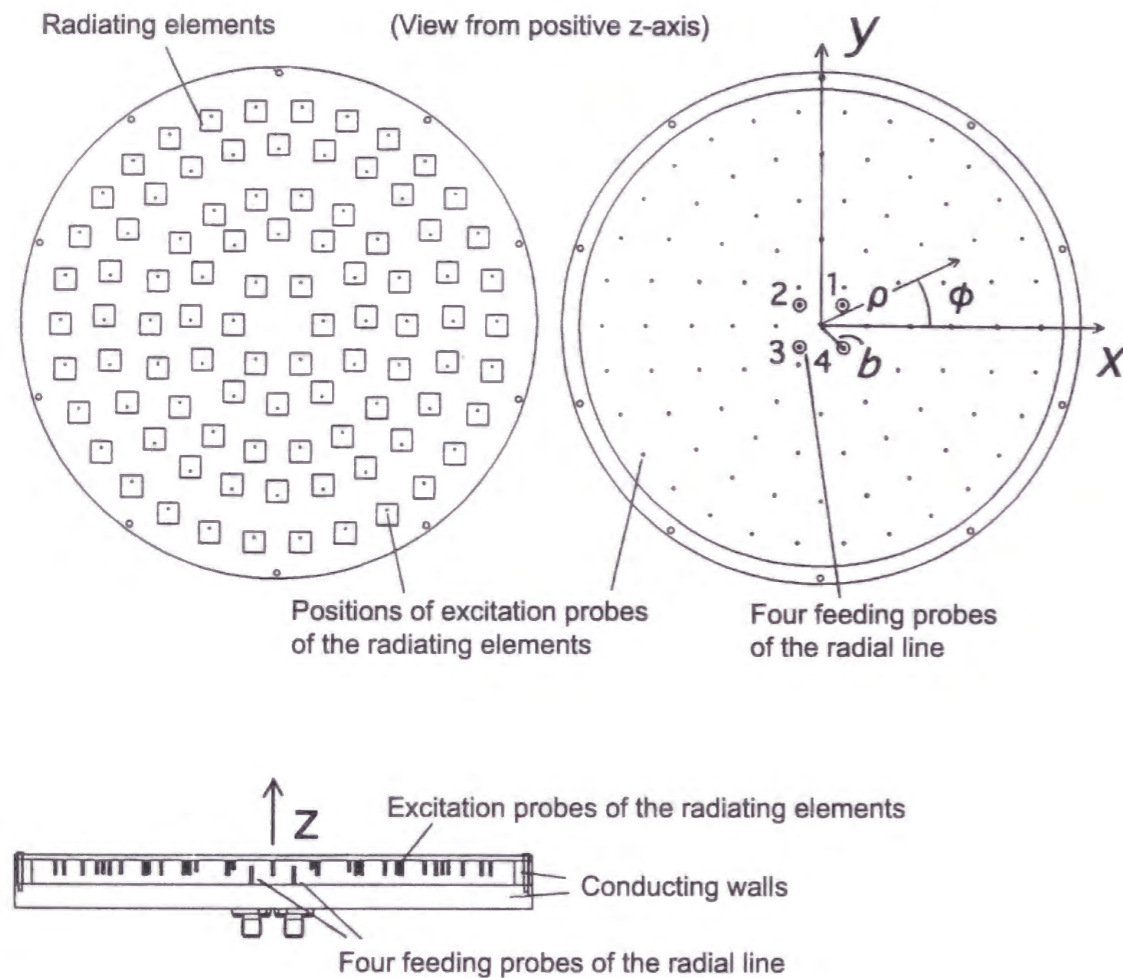
Figure 4.1: Radial line planar monopulse antenna.

4.2 Probes in a radial line

In this section, an analysis is carried out for the mutual coupling between two probes in a radial line, and an experimental verification is given. For the fields, $e^{j\omega t}$ dependence is assumed. The self impedance of a probe in a radial line was studied extensively by Williamson *et. al.*, and accurate results were obtained [52]. In this section, we give a simpler analysis by using the EMF method with a sinusoidal electric current on the surface of the probe. The resultant expressions are simple for both the self and mutual impedances, and approximately closed form expressions of the mutual impedance and the mutual coupling coefficient will be extensively used throughout the arguments in the later sections.

Consider a single isolated probe which is located at the center of the radial line, and extension of the center line of the probe is identified by the z-axis of the cylindrical coordinates (ρ, ϕ, z). On the surface of the probe, we assume a rotationally symmetric surface current density $J(z)$ which is independent of ϕ. In this case, z-component of electric field $E_z(\rho, z)$ inside the radial line is expressed by the following Green's function $G(\rho, z|\rho', z')$ [53]:

$$
\begin{aligned}
E_z(\rho, z) &= \int_0^l dz' \int_0^{2\pi} d\phi' a G(\rho, z|a, z') J(z'), \\
G(\rho, z|\rho', z') &= -\frac{\eta k}{4h} J_0(k\rho') H_0^{(2)}(k\rho) \\
&\quad + \frac{\eta j}{\pi k h} \sum_{n=1}^{\infty} \gamma_n^2 I_0(\gamma_n \rho') K_0(\gamma_n \rho) \cos \frac{n\pi z}{h} \cdot \cos \frac{n\pi z'}{h}, \quad (4.1) \\
\gamma_n &= \sqrt{(n\pi/h)^2 - k^2}, \quad (4.2)
\end{aligned}
$$

where $J_0(x), H_0^{(2)}(x), I_0(x)$, and $K_0(x)$ are cylindrical functions, a and l are the radius and the insertion length of the probe, respectively, k is the TEM mode propagation constant, and $\eta = 120\pi$. The height of the radial line is h, and from now on we assume that the

TEM mode is the only propagation mode. The derivation of (4.1) is the same as that of the Green's function in the previous section except the term $AH_0^{(1)}(\kappa_n\rho)$, $(\rho \leq \rho')$ in (3.45) being replaced by $AJ_0(\kappa_n\rho)$, $(\rho \leq \rho')$ to impose the finite condition of fields at the center of the radial line. Figure 4.2 shows the geometry of two probes in a radial line. The mutual impedance Z_{ij} between the two probes i and j is obtained by using the EMF method with sinusoidal currents I_i and I_j on the surfaces S_i and S_j of the probes i and j, respectively, as follows:

$$Z_{ij} = -\frac{1}{I_i(0)I_j(0)} \int_{S_i} \int_{S_j} J_i G(i|j) J_j dS_j dS_i, \tag{4.3}$$

$$I_i = I_i(0)\frac{\sin k(l_i - z_i)}{\sin kl_i}, \tag{4.4}$$

$$= 2\pi a_i J_i(z_i), \tag{4.5}$$

where a_i and a_j are radii, and l_i and l_j are insertion lengths of the probes i and j, respectively. In the above formulas, we have assumed that the currents I_i and I_j are real, and their feeding point intensities are $I_i(0)$ and $I_j(0)$. The Green's function (4.1) is denoted symbolically as $G(i|j)$. The self impedance Z_{ii} of the probe i is obtained by performing the two surface integration on the same surface S_i. The integrals in (4.3) are carried out by using the addition theorem [2] of cylindrical functions with the results,

$$Z_{ii} = \frac{\eta}{4kh} J_0(ka_i) H_0^{(2)}(ka_i) \tan^2 \frac{kl_i}{2}$$
$$- \frac{k\eta j}{\pi h} \sum_{n=1}^{\infty} I_0(\gamma_n a_i) K_0(\gamma_n a_i) \frac{\{\cos kl_i - \cos(n\pi l_i/h)\}^2}{\gamma_n^2 \sin^2 kl_i}, \tag{4.6}$$

$$Z_{ij} = \frac{\eta\delta_0}{4kh} J_0(ka_i) J_0(ka_j) H_0^{(2)}(kd) \tan\frac{kl_i}{2} \cdot \tan\frac{kl_j}{2}$$
$$- \frac{k\eta j}{\pi h} \sum_{n=1}^{\infty} \delta_n I_0(\gamma_n a_i) I_0(\gamma_n a_j) K_0(\gamma_n d)$$
$$\cdot \frac{\{\cos kl_i - \cos(n\pi l_i/h)\}\{\cos kl_j - \cos(n\pi l_j/h)\}}{\gamma_n^2 \sin kl_i \cdot \sin kl_j}, \tag{4.7}$$

$$\delta_n = \begin{cases} 1 & \text{(type 1)} \\ (-1)^{n+1} & \text{(type 2)}, \end{cases} \tag{4.8}$$

where d is the distance between the center points of the probes.
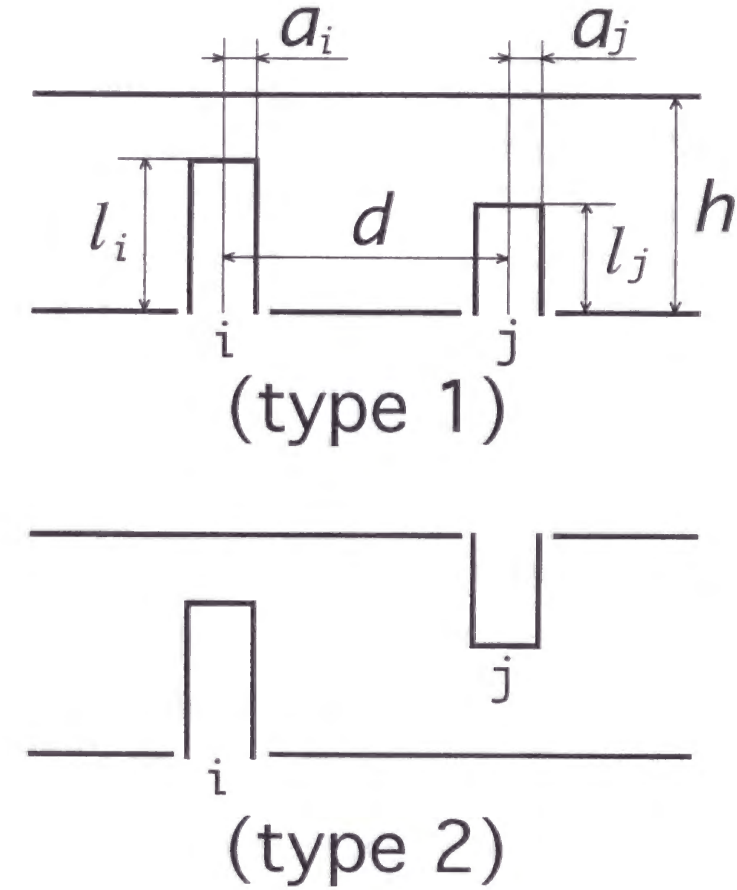
Figure 4.2: Two probes in a radial line.

When l_i is not too close to h, a useful approximate expression of Z_{ii} can be obtained by using the procedures shown in Appendix C with the following result:

$$Z_{ii} \simeq \frac{\eta}{4kh} J_0(ka_i) H_0^{(2)}(ka_i) \tan^2 \frac{kl_i}{2} - \frac{kh^2 \eta j}{2\pi^4 a_i} P\left(\frac{\pi l_i}{h}\right) - \frac{k\eta j}{\pi h} \sum_{n=1}^{M} Q_n, \qquad (4.9)$$

$$\begin{aligned}
P(x) \quad = \quad & \zeta(3)c(x) \\
& + \left\{ \frac{c(x)}{4}(\ln 2x^2 - 3) + \frac{\ln 2}{4c(x)} + \frac{1}{2}\ln 2x - \frac{3}{4} \right\} x^2 \\
& - \left\{ \frac{5c(x)}{576} + \frac{1}{192c(x)} + \frac{1}{72} \right\} x^4 \\
& - \left\{ \frac{17c(x)}{172800} + \frac{1}{11520c(x)} + \frac{1}{5400} \right\} x^6 \quad + \quad ..... \quad , \qquad (4.10)
\end{aligned}$$

$$c(x) \quad = \quad \tan^2\left(\frac{kh}{2\pi}x\right), \qquad (4.11)$$

$$Q_n \quad = \quad \left\{ \frac{I_0(\gamma_n a_i) K_0(\gamma_n a_i)}{\gamma_n^2} - \frac{h^3}{2\pi^3 a_i n^3} \right\} \frac{\{\cos kl_i - \cos(n\pi l_i/h)\}^2}{\sin^2 kl_i}, \qquad (4.12)$$

where $\zeta(x)$ is the Riemann zeta function, and $\zeta(3) \simeq 1.202$. In the above formula, Q_n corrects the error due to the asymptotic approximations in Appendix C. $M = 2$ or 3 gives the sufficient accuracy for practical applications. In that case that the distance between the two probes is much larger than the operating wavelength, the infinite series of Z_{ij} can be adequately approximated by the first term because $K_0(\gamma_n d)$ decays exponentially when the argument grows large,

$$Z_{ij} \simeq \frac{\eta \delta_0}{4kh} J_0(ka_i) J_0(ka_j) H_0^{(2)}(kd) \tan \frac{kl_i}{2} \cdot \tan \frac{kl_j}{2}. \qquad (4.13)$$

The mutual coupling coefficient in the scattering matrix between the probes i and j is calculated as follows:

$$S_{ij} = \frac{2Z_{ij}/Z_0}{(Z_{ii}/Z_0 + 1)(Z_{jj}/Z_0 + 1) - Z_{ij}^2/Z_0^2}, \qquad (4.14)$$

where Z_0 is the characteristic impedance of the feed lines which are attached to the probes.

To see the validity of the derived formulas, measurements have been carried out. Figure 4.3 shows comparisons between the measured and calculated values of S_{ij}. Good agreement between them supports the theory.
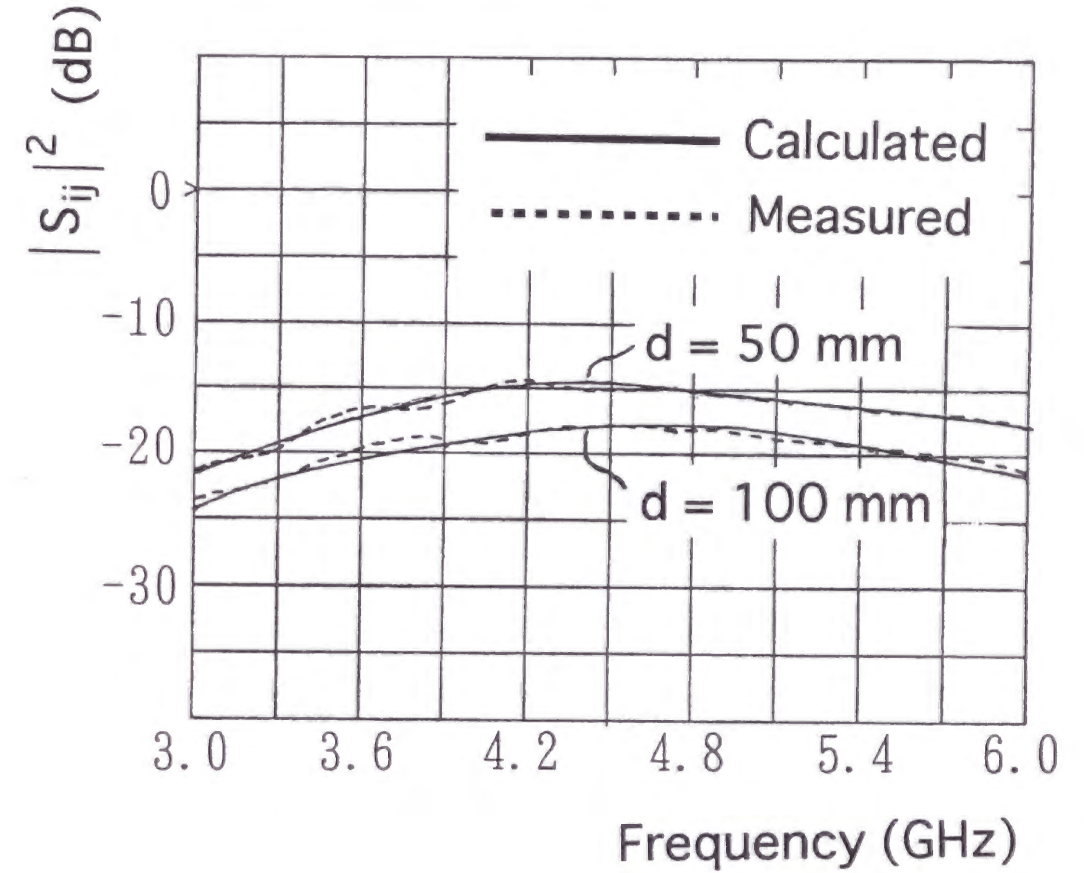
Figure 4.3: Comparison between calculated and measured values of S_{ij} (type 1 coupling). The parameters are $a_1 = a_2 = 0.65$mm, $l_1 = l_2 = 15.0$mm, and $h = 18.0$mm. Comparison has been made with $d = 50, 100$mm throughout the frequency range from 3.0 to 6.0 GHz.

4.3 Monopulse pattern synthesis

In this section, a phenomenological analysis is carried out about the synthesis of monopulse patterns by using the multiple port fed radial line. In Fig.4.1, the four feeding probes of the radial line are identical in dimensions, and their positions of the center points are identical in the radial direction and equally spaced in angles: The positions of the probes 1 to 4 are $(\rho, \phi(\deg)) = (b, 45°), (b, 135°), (b, 225°)$, and $(b, 315°)$, respectively. The feeding points of the radiating elements are arranged in concentric circles centered at the origin of the radial line.

The mutual coupling S_{fi} between the f-th feeding probe of the radial line and the i-th excitation probe which is attached to the i-th radiating element can be approximately expressed as follows:

$$S_{fi} \simeq C_0 Z_{fi}, \tag{4.15}$$

$$C_0 = \frac{2/Z_0}{(1 + Z_{ff}/Z_0)(1 + Z_{ii}/Z_0)}, \tag{4.16}$$

$$Z_{fi} \simeq \frac{\eta \delta_0}{4kh} J_0(ka_f) J_0(ka_i) H_0^{(2)}(kd) \tan\frac{kl_f}{2} \cdot \tan\frac{kl_i}{2}, \tag{4.17}$$

where the distance d between the centers of the two probes is assumed to be large enough compared with the operating wavelength so that the formula (4.13) in the previous section is applicable, and we have further assumed $|Z_{ij}/Z_0| \ll 1$ in (4.16). Z_{ff} and Z_{ii} in (4.16) are the self impedance of the f-th feeding probe of the radial line and the i-th excitation probe of the radiating element, respectively, and Z_0 is the loaded impedance of the probes. In this analysis, we assume that the input impedance of the radiating element fed by probe i and the characteristic impedance of the feed line attached to the probe f are all identical to Z_0. Other parameters are the same as those in the previous section, except that the attached subscripts f and i represent quantities of the f-th feeding probe of the radial line and the i-th excitation probe of the radiating element, respectively.

From now on, we ignore damping of power in the radial line due to radiation of the radiating elements as a wave travels in the radial line. Then an excitation distribution D_i of the array is approximately expressed, by using the excitation coefficients A_f of the four feeding probes, as follows:

$$D_i = \sum_{f=1}^{4} A_f S_{fi}, \tag{4.18}$$

$$\simeq C_1 \sum_{f=1}^{4} A_f H_0^{(2)}(k|\boldsymbol{\rho}_i - \boldsymbol{\rho}_f'|), \tag{4.19}$$

$$C_1 = \frac{C_0 \eta \delta_0}{4kh} J_0(ka_f) J_0(ka_i) \tan\frac{kl_f}{2} \cdot \tan\frac{kl_i}{2}, \tag{4.20}$$

where $\boldsymbol{\rho}_i$ and $\boldsymbol{\rho}_f'$ are positions of the probes i and f, respectively.

The monopulse Σ pattern can be realized by setting,

$$A_1 = A_2 = A_3 = A_4 = A. \tag{4.21}$$

With the above excitations, D_i is expressed as follows after some calculations using the addition theorem of cylindrical functions:

$$D_i = 4C_1 A J_0(kb) H_0^{(2)}(k\rho) + 8C_1 A \sum_{n=1}^{\infty} J_{4n}(kb) H_{4n}^{(2)}(k\rho)(-1)^n \cos 4n\phi, \tag{4.22}$$

$$\sim 4C_1 A J_0(kb) H_0^{(2)}(k\rho) + O((kb)^4), \tag{4.23}$$

where $\rho = |\boldsymbol{\rho}_i|$, $b = |\boldsymbol{\rho}_f'|$, and the last formula applies when kb is small. (4.23) shows that D_i is approximately $2J_0(kb)$ times that of an equivalent RLPA with a single probe excitation at the center when the excitation coefficients A_f are normalized by a unit power; i.e. $A_f = 1/2$.

The monopulse Δ pattern can be synthesized, for example, in the x-z plane by setting,

$$A_1 = -A_2 = -A_3 = A_4 = A. \tag{4.24}$$

In this case, the expression of D_i is as follows:

$$D_i = 4\sqrt{2}C_1 A \sum_{n=1}^{\infty} J_{2n-1}(kb) H_{2n-1}^{(2)}(k\rho) \cos\{(2n-1)\phi\} \exp\{j\frac{\pi}{2}(t_n - n)\}, \tag{4.25}$$

$$\sim 4\sqrt{2}C_1 A J_1(kb) H_1^{(2)}(k\rho) \cos\phi + O((kb)^3), \tag{4.26}$$

where $t_n = 1$ when n is an odd integer, and $t_n = 0$ when n is an even integer. The last formula is valid when kb is small enough. In (4.26), the term of $\cos\phi$ produces out of phase excitations of radiating elements whose positions are symmetric with respect to the center point of the radial line. This realizes the Δ pattern when the radiating elements are arranged on concentric circles symmetrically with respect to the origin of the radial line. By symmetry considerations, it is clear that all the higher order modes in (4.25) never affect the null depth of the Δ pattern if the radiating elements are arranged in the same symmetry as those of the four feeding probes.

To synthesize the Δ pattern in the y-z plane, we choose,

$$A_1 = A_2 = -A_3 = -A_4 = A. \tag{4.27}$$

It is noted that the monopulse patterns can be formed by using only two feeding probes of the radial line. This type of antenna may be applicable to a system which employs a monopulse tracking by using azimuthal only rotation. In this case, we put the two feeding probes of the radial line, for example in the x-axis, whose position coordinates (x, y) are $(b, 0)$ and $(-b, 0)$. The Σ pattern is formed by setting $A_1 = A_2 = A$ with the result,

$$D_i = 2C_1 A J_0(kb) H_0^{(2)}(k\rho) + 4C_1 A \sum_{n=1}^{\infty} J_{2n}(kb) H_{2n}^{(2)}(k\rho) \cos(2n\phi). \tag{4.28}$$

The Δ pattern can be excited by setting $A_1 = -A_2 = A$ with the result,

$$D_i = 4C_1 A \sum_{n=1}^{\infty} J_{2n-1}(kb) H_{2n-1}^{(2)}(k\rho) \cos\{(2n-1)\phi\}. \tag{4.29}$$

4.4   Design of uniform aperture field distribution

In this section, a design procedure of uniform aperture field distribution of RLPMA is described. This procedure is also applicable to the conventional probe fed RLPAs [46]-[48]. To achieve the uniform aperture field distribution for RLPA, a natural arrangement of the radiating elements is the concentric circle arrangement with the elements placed and excited uniformly on the aperture. For Circularly Polarized RLPA (CPRLPA), the above condition is realized by determining the spacing of the radiating elements in order to satisfy the conditions of effective aperture area of one radiating element and of grating lobe suppression. The excitation phases are adjusted in phase by rotating the radiating elements. In the case of Linearly Polarized RLPA (LPRLPA), we choose the radii of the concentric circles in a half wavelength step in the radial direction to suppress the grating lobe, and the radiating elements are rotated by 180° for side by side concentric arrangement circles to realize in phase excitation. The desired amplitude excitation distribution can be realized by adequately choosing the insertion lengths of the excitation probes of the radiating elements. In these designing procedure, it is important to include the effect of damping of power in the radial line due to the radiation from the radiating elements: From now on, we call it the radiation damping. It is also noted that if the insertion length of the probe is varied, the excitation phase also varies because of a variation of the probe reactance. This effect is not a significant restriction for CPRLPA in a construction of the hardware because we can suppress it by rotating the radiating elements by certain angles. For LPRLPA the radius of the concentric arrangement circles must be slightly modified so as to realize the in phase excitation. In the following subsections, we consider two different feed cases:

- Traveling wave feed case, and

- Standing wave feed case.

Assumptions are made that the field inside the radial line can be well approximated by that of an equivalent single probe fed RLPA, *i.e.* the statement concerning (4.23) holds, furthermore, rotationally symmetric characteristics are never distorted regarding the shape of wavefront and amplitude of the TEM propagation mode which emanates from the feeding probe. The mutual couplings between feeding probes of the radiating elements are neglected. The mutual coupling effect of the radiating elements in the free space region outside the radial line and its influence on the feed distributions are also neglected. Although the above mentioned rather crude approximations are made, simple conditions can be obtained about the realization of uniform aperture field distribution, and design procedures of the antenna parameters appear to be effective as we will see below.

Before starting the analysis, we mention here the following fundamental limitation of the magnitude $|S_{ij}|^2$ of the mutual coupling between two probes i and j in a radial line. The two probes i and j are inserted in a radial line with insertion length l_i and l_j, respectively, and the distance between the two center points of the probes is d. The following upper bound exists:

$$\lim_{kd \to \infty} kd|S_{ij}|^2 = \alpha(l_i, l_j), \tag{4.30}$$

where $\alpha(l_i, l_j)$ is calculated by using (4.13) and (4.14) with the result,

$$\alpha(l_i, l_j) = \left\{ \frac{Z_0 \eta J_0(ka_i) J_0(ka_j) \tan(kl_i/2) \tan(kl_j/2)}{\sqrt{2\pi} kh(Z_0 + Z_{ii})(Z_0 + Z_{jj})} \right\}^2. \tag{4.31}$$

When l_i is fixed, the upper bound of $|S_{ij}|^2$ is expressed as follows:

$$|S_{ij}|^2 \le \frac{\alpha^{MAX}}{kd}, \tag{4.32}$$

where α^{MAX} is the maximum of $\alpha(l_i = \text{const.}, l_j)$. For a practical application, $l_j = h$ gives a good estimate for α^{MAX}.

4.4.1 Traveling wave feed

When the end of the radial line is terminated by a matched load, the radiating elements are fed by the traveling wave in the radial line which decreases due to the radiation damping as the wave travels in the radial direction. The radiating elements are arranged in concentric circles t, $(t = 1, 2, ..., T)$ with their centers at the center of the radial line. The total number of the radiating elements on the t-th circle is $N(t)$, and the dimensions of the excitation probes of the radiating elements on each one circle are assumed to be identical. The excitation distribution $S(t)$ of the radiating element on the t-th circle with the radiation damping taken into consideration is approximately calculated as follows by using the mutual coupling coefficient $S_0(t)$ of two isolated probes given by (4.14):

$$S(t) = S_0(t) \prod_{n=1}^{t-1} \left\{ 1 - N(n)|S_0(n)|^2 \right\}^{1/2}, \tag{4.33}$$

$$S(1) = S_0(1), \tag{4.34}$$

where the above formulas can be derived by employing a standard circuit theory with the assumption that the radiation damping in each circle n is very small compared with the total power; *i.e.* $N(n)|S_0(n)|^2 \ll 1$. It is noted that the above formula can be equivalently expressed as follows:

$$S(t) = S_0(t) \left\{ 1 - \sum_{n=1}^{t-1} N(n)|S(n)|^2 \right\}^{1/2}. \tag{4.35}$$

The condition for uniform amplitude distribution with the constant power p for all radiating elements is described as follows:

$$|S(t)|^2 = p = \text{const.}. \tag{4.36}$$

By using (4.35) and (4.36), the above condition reduces to the following,

$$|S_0(t)|^2 = \left\{ p^{-1} - \sum_{n=1}^{t-1} N(n) \right\}^{-1}. \tag{4.37}$$

The loss free condition, *i.e.* radiation of all input power fed to the radial line by the radiating elements, is expressed as follows:

$$p = \left\{ \sum_{n=1}^{T} N(n) \right\}^{-1}. \tag{4.38}$$

From (4.37) and (4.38), the loss free uniform amplitude excitation is realized when the following condition holds for $|S_0(t)|^2$:

$$|S_0(t)|^2 = \left\{ \sum_{n=t}^{T} N(n) \right\}^{-1}. \tag{4.39}$$

When the array arrangement is $N(n) = N_1 n$, which gives the uniform density arrangement of the radiating elements, for example $N_1 = 6$ in Fig.4.1, the above equation is simplified to the following:

$$|S_0(t)|^2 = \frac{2}{N_1\{T(T+1) - t(t-1)\}}. \tag{4.40}$$

As described previously, the upper bound of the probe mutual coupling (4.32) must be satisfied as well. When the radius of the arrangement circle t is td_t, the upper bound condition (4.32) is expressed as follows:

$$|S_0(t)|^2 \leq \frac{1}{\xi_t t}, \tag{4.41}$$

$$\xi_t = \frac{kd_t}{\alpha^{MAX}}. \tag{4.42}$$

The equations (4.39) and (4.40) have monotonically increasing properties as t grows large, and thus their maxima occur at $t = T$. Therefore, if the following condition is satisfied, the condition (4.41) is satisfied for all t:

$$\frac{N(T)}{T} \geq \xi_T. \tag{4.43}$$

It must be noted that this condition should never be realized by actual hardware if we use the matched load termination, because this condition requires the probes on the circle

74

T to radiate out all the incident power; *i.e.* the condition essentially requires the probes to have infinitely strong coupling to the radial line. However, the loss free condition is satisfied if the short circuited termination is introduced. In this case, the probes on the circle T can be fed by standing waves, and this enables the actual hardware to satisfy the condition (4.43) if $|S_0(T)|^2$ is large enough as explicitly shown in (4.44) below. An appropriate choice of a position of the short circuited termination is a quarter wavelength away in the radial direction from the circle T, and reflected waves from the termination can be superposed in phase at the position of T with this structure. By using the large argument asymptotic approximation of Hankel function in (4.17), and superposing the incident and reflected wave contributions of $S_0(T)$, it is verified that $|S_0(T)|^2$ can be approximately replaced with $|2S_0(T)|^2$ in this case. The condition of uniform amplitude excitation for the circle T then becomes as follows:

$$|2S_0(T)|^2 = 1/N(T) \leq 4/\xi_T T. \tag{4.44}$$

For the other traveling wave fed probes, the following must be satisfied:

$$|S_0(t)|^2 = \left\{ \sum_{n=t}^{T} N(n) \right\}^{-1} \leq 1/\xi_t t. \tag{4.45}$$

It is noted that the condition is automatically satisfied by all the other circles $t < T - 1$ if the last inequality is satisfied by the $(T-1)$-th circle. When $N(t) = N_1 t$ and all ξ_t are identical to ξ, the above condition (4.45) reduces simply to the following:

$$\frac{(2T-1)N_1}{T-1} \geq \xi, \tag{4.46}$$

which is compatible with (4.44) as well. Whenever the above conditions (4.44)-(4.47) are satisfied, we can obtain the RLPA with the uniform aperture field distribution by using the traveling wave feed for the circles $t < T$, and the standing wave feed for T-th circle. In the next subsection, we consider the case when the above conditions are not satisfied. In these occasions, standing wave feed of more than one arrangement circles must be employed.

75

4.4.2 Standing wave feed

When the standing wave feed is used for more than one arrangement circles, the relation between $S_0(t)$ and $S(t)$ must be modified along the discussion about the replacement of $|S_0(T)|^2$ with $|2S_0(T)|^2$ described in the previous subsection. The new relations between $S_0(t)$ and $S(t)$ are as follows:

$$S(t) = \overrightarrow{S}(t) + \overleftarrow{S}(t), \qquad (4.47)$$

$$\overrightarrow{S}(t) = S_0(t) \prod_{n=1}^{t-1} \left\{ 1 - N(n)|S_0(n)|^2 \right\}^{1/2}, \qquad (4.48)$$

$$\overrightarrow{S}(1) = S_0(1), \qquad (4.49)$$

$$\overleftarrow{S}(t) = e^{j\psi_t} S_0(t) \left[\prod_{n=1}^{T} \left\{ 1 - N(n)|S_0(n)|^2 \right\}^{1/2} \right]$$
$$\cdot \left[\prod_{m=t+1}^{T} \left\{ 1 - N(m)|S_0(m)|^2 \right\}^{1/2} \right], \qquad (4.50)$$

$$\overleftarrow{S}(T) = e^{j\psi_T} S_0(T) \prod_{n=1}^{T} \left\{ 1 - N(n)|S_0(n)|^2 \right\}^{1/2}, \qquad (4.51)$$

where $\overrightarrow{S}(t)$ and $\overleftarrow{S}(t)$ correspond to the excitation coefficients of the radiating element on the t-th arrangement circle which are produced, respectively, by the incident wave from the center and the reflected wave from the short circuited end of the radial line. The factor $\exp(j\psi_t)$ represents phase difference at the t-th arrangement circle between the incident and reflected waves. (4.48)-(4.51) can be easily derived by physical insight, for example, as for (4.50) the product part $\prod_{n=1}^{T}$ represents the radiation damping in the period of the wave propagation from the center to the termination of the radial line, while the part $\prod_{m=t+1}^{T}$ represents the same effect while the reflected wave departs from the termination and arrives at the t-th arrangement circle. The phase of $\overleftarrow{S(t)}$ is determined by the TEM mode wavefront.

Let $1, 2, ..., L-1$ be the arrangement circles which are fed by the traveling wave from the center of the radial line, and let $L, L+1, ..., T$ be the rest of the circles which are fed

by the standing wave by using the reflected wave from the end of the radial line as well as the incident wave from the center. The uniform amplitude excitation condition for the radiating elements on the circles $t = 1, 2, ..., L-1$ is given by (4.39) in the previous subsection, with the upper bound condition for $|S_0(t)|^2$ given in (4.45). For the circles $K = L, L+1, ..., T$, the condition is determined by using (4.47)-(4.51) as follows:

$$|S(K)|^2 = |\overrightarrow{S}(K) + \overleftarrow{S}(K)|^2 = \left\{ \sum_{n=1}^{T} N(n) \right\}^{-1}. \qquad (4.52)$$

(4.52) gives simultaneous equations with respect to $|S_0(L)|^2, |S_0(L+1)|^2, ..., |S_0(T)|^2$, and they can be solved by numerical means. After the solution is obtained, they must be examined to be compatible with the condition (4.41). If the solution is incompatible with that condition, the number of the standing wave feed circles is increased, and then the same procedure is tried.

4.4.3 Design procedures

We summarize here practical procedures to design CPRLPA and LPRLPA which have the uniform aperture field distribution. The following procedures have an advantage of simplicity because the numerical optimization procedures can be carried out independently for each arrangement circle. This advantage comes from the fact that the objective functions expressed by $S_0(t)$ are uniquely fixed for all the arrangement circles t.

1. CPRLPA

   (a) Place the radiating elements uniformly on the aperture;

   (b) Determine the objective values of $|S_0(t)|^2$;

   (c) Use a numerical optimization procedure to determine the insertion length of the excitation probe of the radiating element for each circle t independently;

   (d) Calculate the resultant excitation phases of the radiating elements by (4.47); and

   (e) Rotate the radiating elements to fix the excitation phases identical.

2. LPRLPA

   (a) Place the radiating elements uniformly with radii of the arrangement circles side by side in a half wavelength step;

   (b) Determine the objective values of $|S_0(t)|^2$;

   (c) Calculate a phase ϕ_M of $S_0(M)$, where M is an arbitrary chosen arrangement circle;

   (d) Set the objective value to $|S_0(t)| \exp(j\phi_M)$ for $S_0(t), t = .., M-2, M, M+2, ..,$ and to $|S_0(t)| \exp(j\phi_M + j\pi)$, for $S_0(t), t = .., M-1, M+1, ..;$ and

   (e) By using the insertion length of the excitation probe of the radiating element and the radius of the arrangement circle for each t as variables, carry out a numerical optimization procedure, independently for each t, to realize the objective values of $S_0(t)$.

Strictly speaking, the above procedure for LPRLPA will not give a perfect solution for the uniform aperture field distribution because the density of the radiating elements on the aperture may deviate from the uniform density. However, in practical applications, this factor will not give a significant effect to the antenna performance. When one desires further accuracy, simultaneous optimization procedures with $2T$ variables must be applied. The contents of $2T$ variables are probe insertion lengths and radii of each arrangement circles.

4.5 Design example and experiment

A RLPMA as shown in Fig.4.1 with $N(t) = 6t$ and $T = 5$, has been fabricated by using the design procedure described in the previous sections. In this example, the standing wave feed of two arrangement circles $T - 1$ and T is used. The feed region parameters of the fabricated antenna with the operating wavelength λ are $a_f = 0.02\lambda$, $l_f = 0.24\lambda$, $d = 0.33\lambda$, and $h = 0.27\lambda$. The radii of feeding probes of the radiating elements are all identical to 0.02λ, the radii of the arrangement circles are $0.48\lambda, 0.95\lambda, 1.39\lambda, 1.94\lambda$, and 2.42λ, respectively in the radial direction, and the insertion lengths of the probes on the respective circles are $0.12\lambda, 0.16\lambda, 0.19\lambda, 0.16\lambda$, and 0.17λ. Linearly polarized microstrip antennas which are all resonant at the operating wavelength are used as the radiating elements. Figure 4.4 shows the measured and calculated monopulse patterns in the y-z plane (E-plane). Almost the same characteristics are observed in the x-z plane as well. The agreement between the calculated and measured values in the Σ pattern supports the theory described in the previous section. In the Δ pattern, the calculated values are plotted without considering the radiation damping. The measured Σ/Δ ratio is more than 40 dB. These results show the capability of RLPMA for the monopulse tracking operation.
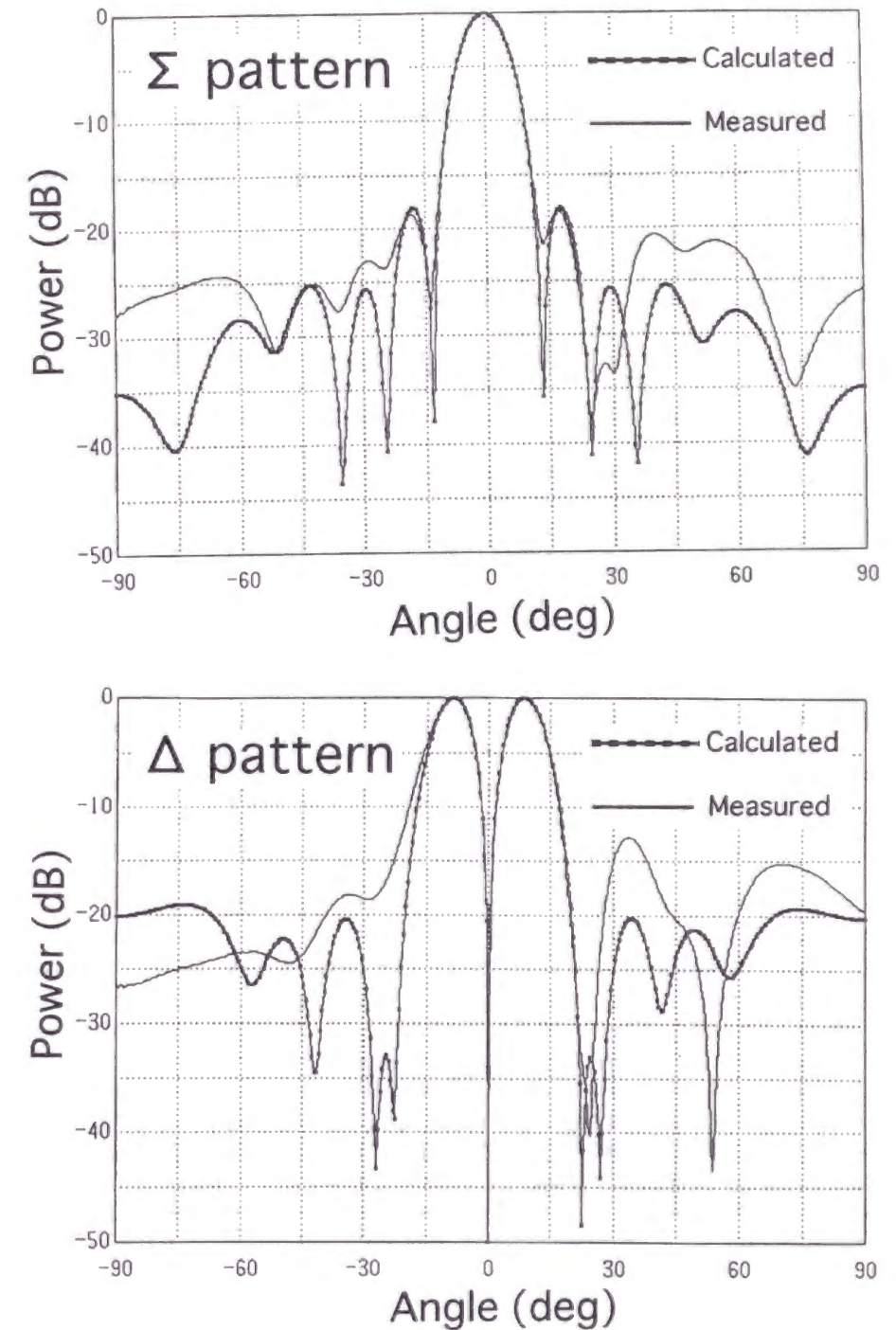
Figure 4.4: E-plane monopulse Σ and Δ patterns of RLPMA.

4.6 Summary

A design procedure is developed for a newly proposed planar antenna array, the radial line planar monopulse antenna. The antenna is highly efficient because of a waveguide feed, and is capable of synthesizing monopulse Σ and Δ patterns by a novel use of a multiple port fed radial line with in phase or out of phase excitations of sets of feeding probes. By using the EMF method, an analysis of the mutual coupling between probes in the radial line is carried out with the result of simple closed form expressions. The mechanism of monopulse pattern synthesis is made clear through modal expansions in the radial line. It is concluded that the dominant mode excited by feeding probes gives significant contribution for the monopulse pattern synthesis if the feeding radius of the probes are placed near the center of the radial line. For Σ pattern, the dominant mode has no angular dependence which gives in phase excitation of radiating elements. For Δ pattern, it has sinusoidal dependence in angle which gives out of phase excitation for opposite pairs of radiating elements with respect to the center of the radial line. Simple design procedures are developed for the uniform aperture field distribution by using algebraic relations obtained between the parameters. Perfect antenna efficiency can be obtained by means of the standing wave feed. A prototype antenna has been fabricated and the radiation characteristics have been measured. The measured result supports the theory and verifies the capability of the antenna for the monopulse tracking operation. The feature of the antenna is suited for application to mobile satellite communications systems.

The method developed in this chapter is considered to give a typical example of the analytical modeling of the feeding structure of antenna arrays.

Chapter 5

An Analysis of Antenna Coupling Between Arrays on a Polyhedron Structure

5.1 Introduction

In this chapter, an analysis is carried out for antenna coupling between arrays on a polyhedron structure [54]. The effect of the antenna farm scattering is treated through an application of GTD combined with the EMF method.

Multifunction antennas are required for recent communication systems and radar systems. Antenna arrays on a polyhedron structure are one of good candidates for such systems because of their capability of simultaneous operations for different signals from different directions. However, a difficulty arises in designing such an antenna. In the period of simultaneous operations, interference between arrays may cause some damage to the hardware such as receiving modules. Accurate estimation of a level of the interference is needed. The analysis of antenna coupling between arrays on a polyhedron structure has not been reported so far. As a related topic, Bailey [55] suggested a method to analyze mutual coupling between circular waveguide fed apertures in a rectangular ground plane

where the effect of edge diffracted field from the finite ground plane for the self and mutual admittance was included. In this chapter, we extend the method to the calculation of antenna coupling between arrays on a polyhedron structure which have linearly polarized circular MSAs as radiating elements.

In Section 5.2, an analysis is carried out for mutual couplings between two isolated circular MSAs located on different faces of a perfectly conducting wedge. MSAs are treated by the cavity model [6]. Radiation field of one of the antennas is incident to a wedge, and then the Keller's GTD diffraction coefficients are used for diffracted field which is incident to the other antenna. The EMF method is applied to the calculation of the mutual admittance between them and gives a closed form result. The mutual coupling between two elements is calculated from the result.

In Section 5.3, the method is extended to the calculation of antenna coupling between arrays on a polyhedron structure. The antenna coupling is defined as mutual couplings between a radiating element in one array and all radiating elements in the other array.

In Section 5.4, experimental verification of the method is carried out. The mutual coupling has been measured between a circular MSA and a phased array which has 128 circular MSA elements located on different faces of a polyhedron. Good agreement is obtained between the measured and calculated levels in the period of beam steering of the array.

In Section 5.5, several numerical simulations which describe properties of the antenna coupling are given.

In Section 5.6, a summary of this chapter is given.

5.2 Theory

First of all, we derive an approximate formula for mutual coupling between two linearly polarized circular MSAs separated by a wedge. Figures 5.1 and 5.2 show the geometry of two circular MSAs located on different faces of a wedge.

The radiated magnetic field H_1 from equivalent magnetic current element J_{m1} of MSA1 is given with $e^{j\omega t}$ dependence of field quantities as follows [56]:

$$H_1 = \nabla\nabla \cdot A_{m1}/j\omega\epsilon_0\mu_0 - j\omega A_{m1}, \tag{5.1}$$

where A_{m1} is the magnetic vector potential for the current element. A_{m1} is given by the cavity model [6] as follows:

$$A_{m1} = \frac{\epsilon_0}{4\pi}\frac{e^{-jk\rho}}{\rho}J_{m1}, \tag{5.2}$$

$$J_{m1} = KJ_1(k_{11}\bar{a})K_{m1} = KJ_1(k_{11}\bar{a})\cos(\phi_1 - \phi_{10})i_{\phi_1}, \tag{5.3}$$

where, K is a constant, ϕ_1 is the angle of a current element, ϕ_{10} is the location angle of the feeding probe of the MSA, $k_{11}\bar{a} = 1.84118$ (TM_{11} mode), and $\bar{a}$ is the equivalent radius of the circular MSA by taking the fringing effect [7][56] into consideration,

$$\bar{a} = a\left\{1 + \frac{2h}{a\pi\epsilon_r}(\ln\frac{\pi a}{2h} + 1.7726)\right\}^{\frac{1}{2}}, \tag{5.4}$$

where h and ϵ_r are the thickness and the dielectric constant of the dielectric substrate, respectively, and a is the radius of the MSA.

In order to use GTD, we employ far field approximation to H_1 as follows:

$$H_1 \cong \frac{k}{4\pi\eta j}\frac{e^{-jk\rho}}{\rho}(\hat{\beta}_1 \cdot J_{m1})\hat{\beta}_1, \tag{5.5}$$

where $k = \omega\sqrt{\epsilon_0\mu_0}$, $\eta = 120\pi$, and β_1 is defined customarily [14] as follows:
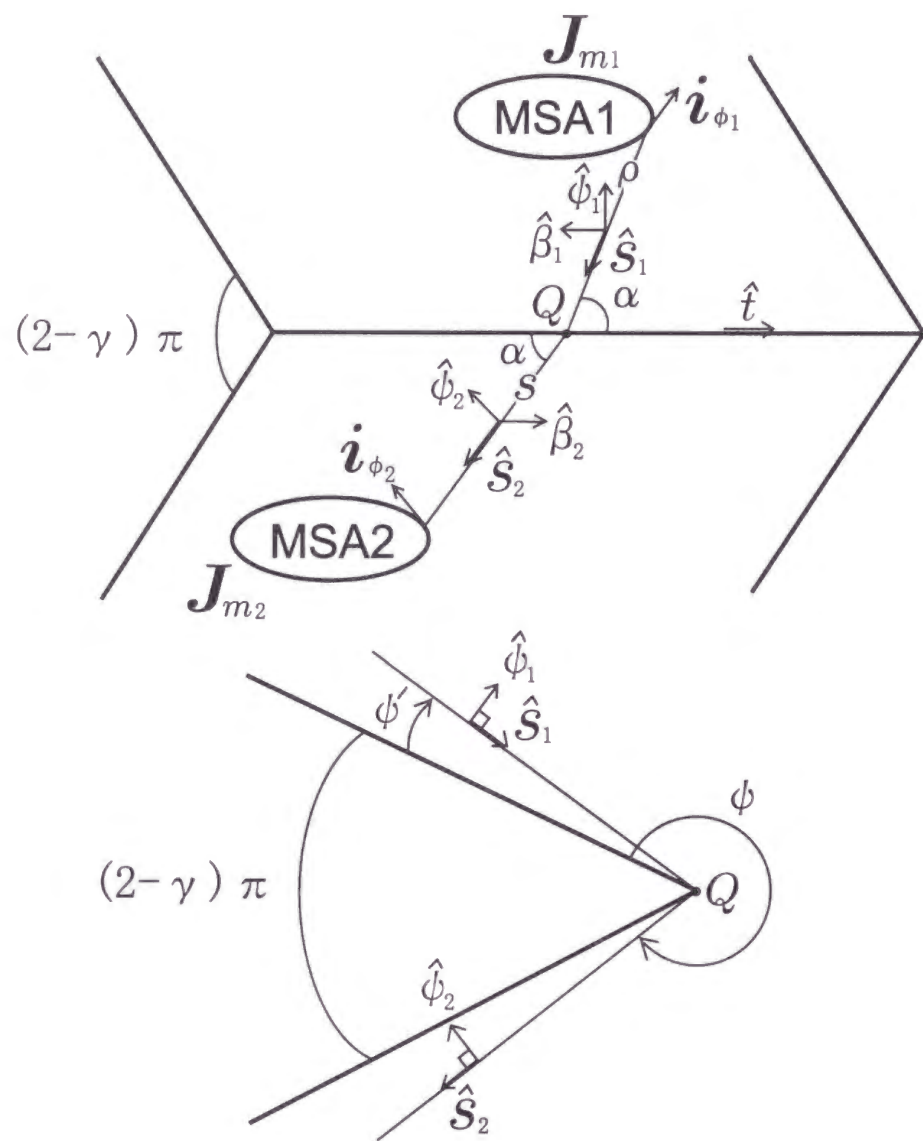
$$\hat{\beta}_1 = \hat{s}_1 \times \hat{\psi}_1. \tag{5.6}$$
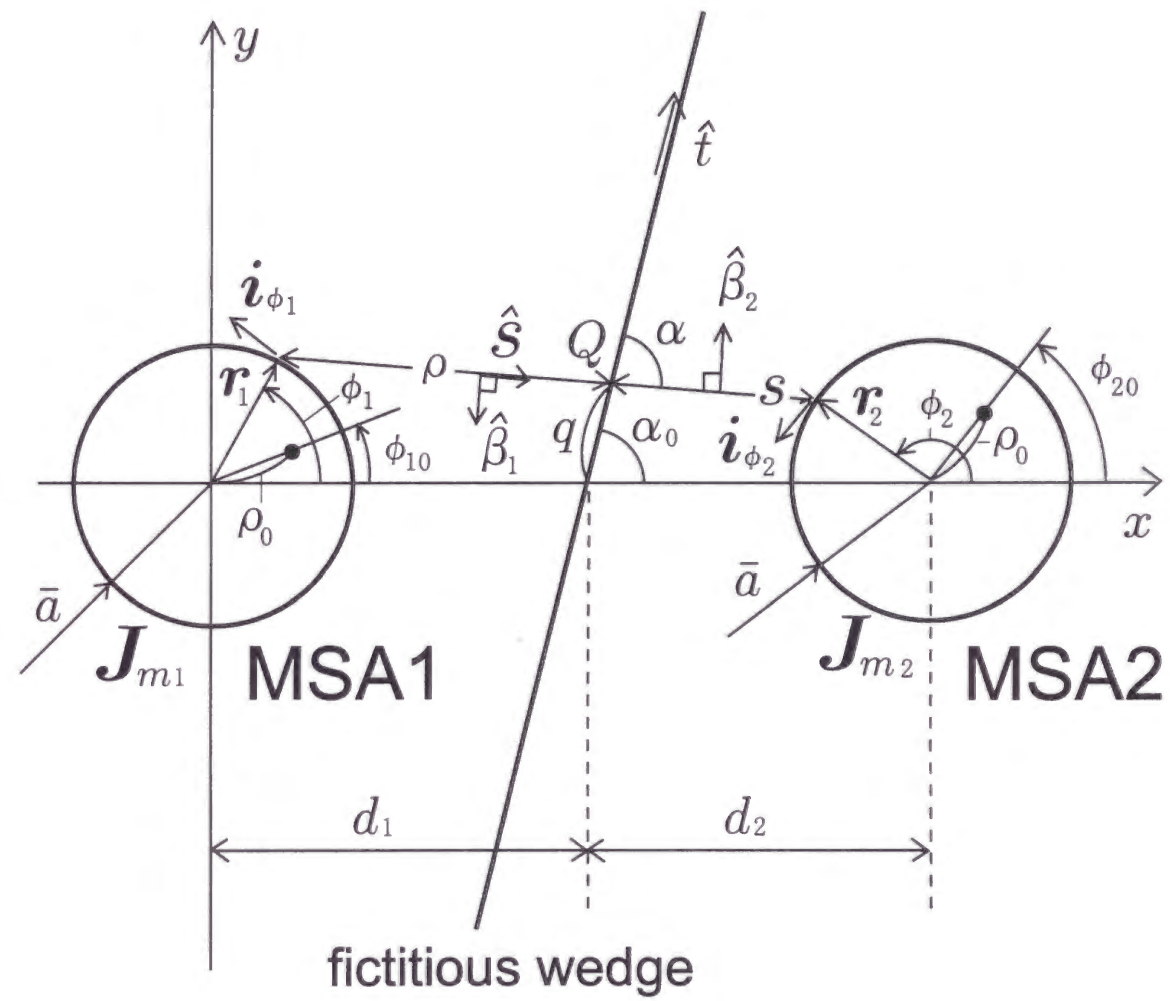
Figure 5.1: Microstrip antennas on different faces of a wedge.

Figure 5.2: Simplified model for the mutual coupling.

The diffracted field H_d from a perfectly conducting wedge is given as follows [14]:

$$H_d = -(\tilde{D}_s \hat{\psi}_2 \hat{\psi}_1 + \tilde{D}_h \hat{\beta}_2 \hat{\beta}_1) \cdot H_1(Q) \sqrt{\frac{\rho}{s(s+\rho)}} e^{-jks}, \tag{5.7}$$

$$\tilde{D}_h^s = \frac{\sin(\pi/\gamma)e^{-j\frac{\pi}{4}}}{\gamma\sqrt{2\pi k}\sin\alpha} \left[\frac{1}{\cos(\pi/\gamma) - \cos\{(\psi - \psi')/\gamma\}} \mp \frac{1}{\cos(\pi/\gamma) - \cos\{(\psi + \psi')/\gamma\}} \right], \tag{5.8}$$

where $H_1(Q)$ is the incident field from MSA1 at the diffraction point Q, ρ is the distance between the magnetic current element of MSA1 and the diffraction point Q, and the distance s between that of MSA2 and Q is defined in the same way, as shown in Figs.5.1 and 5.2. The Keller's GTD diffraction coefficients in Eqs.(5.7) and (5.8) are adapted, because they are adequately applicable to our case where the observing point is well below the shadow boundary.

The mutual admittance Y_{21} between MSA is defined by using the EMF method [56] as follows:

$$Y_{21} = \frac{-h^2 \bar{a}^2}{V_1 V_2^*} \int_{-\pi}^{\pi} d\phi_1 \int_{-\pi}^{\pi} d\phi_2 J_{m2}^* \cdot H_d, \tag{5.9}$$

where, J_{m2} is the equivalent magnetic current element of MSA2 defined in the same form as J_{m1}, and the superscript $*$ represents complex conjugate. V_1 and V_2 are feed point voltages of MSAs 1 and 2, respectively, and they are given as follows:

$$V_1 = V_2 = K J_1(k_{11}\rho_0)h, \tag{5.10}$$

where ρ_0 is the distance between the center of MSA and the feeding point.

In practice, antenna arrays are mounted on the faces of a polyhedron. We make an assumption to the diffraction coefficients as $\psi = \gamma\pi$ and $\psi' = 0$. Then they become as follows:

$$\tilde{D}_s = 0, \tag{5.11}$$

$$\tilde{D}_h = \frac{\sin(\pi/\gamma)e^{-j\frac{\pi}{4}}}{\gamma\sqrt{2\pi k}\sin\alpha} \cdot \frac{2}{\cos(\pi/\gamma) + 1}. \tag{5.12}$$

88

The assumption makes the analysis simple, where the geometry of the problem becomes equivalent to Fig.5.2. The geometry is interpreted as that of the mutual coupling between MSAs on the same ground plane separated by a fictitious wedge. The model is applicable because deviation of the diffracted field with wedge angle γ is contained in the diffraction coefficient $\tilde{D}_h$ and the other parts in $J_{m2}^* \cdot H_d$ in (5.9) do not depend on γ.

We have Y_{21} as follows:

$$Y_{21} = \frac{k\bar{a}^2 j}{4\pi\eta} \left\{ \frac{J_1(k_{11}\bar{a})}{J_1(k_{11}\rho_0)} \right\}^2 \int_{-\pi}^{\pi} d\phi_1 \int_{-\pi}^{\pi} d\phi_2 \frac{\tilde{D}_h g}{\sqrt{\rho s(\rho + s)}} e^{-jk(\rho+s)}, \tag{5.13}$$

$$g = -(K_{m2}^* \cdot \hat{\beta}_2)(\hat{\beta}_1 \cdot K_{m1}). \tag{5.14}$$

We derive an asymptotic expression for Y_{21}. It is assumed that the distances d_1 and d_2 from the centers of the MSAs 1 and 2 to the edge, respectively, are much larger than the equivalent radius of MSA, i.e. , $d_1, d_2 \gg \bar{a}$. Next, we use in (5.14) the following identities obtained from Fig.5.2:

$$r_1 + \rho\hat{s} = d_1\hat{x} + q\hat{t}, \tag{5.15}$$

$$q\hat{t} + s\hat{s} = d_2\hat{x} + r_2. \tag{5.16}$$

These identities give the following relations:

$$\rho = \frac{\sin\alpha_0}{\sin\alpha} \{d_1 - r_1 \cdot \hat{x} + \cot\alpha_0 \cdot (r_1 \cdot \hat{y})\}, \tag{5.17}$$

$$s = \frac{\sin\alpha_0}{\sin\alpha} \{d_2 + r_2 \cdot \hat{x} - \cot\alpha_0 \cdot (r_2 \cdot \hat{y})\}, \tag{5.18}$$

$$\rho + s = |(d_1 + d_2)\hat{x} + r_2 - r_1|. \tag{5.19}$$

89

We expand parts of the integrand as follows:

$$\frac{\tilde{D}_h}{\sqrt{\rho s(\rho + s)}} \cong D_h \frac{1}{\sqrt{d_1 d_2 (d_1 + d_2)}} A, \tag{5.20}$$

$$
\begin{aligned}
A &= 1 + \frac{1}{2d_1}\{\boldsymbol{r_1} \cdot \hat{x} - \cot\alpha_0 \cdot (\boldsymbol{r_1} \cdot \hat{y})\} \\
&\quad - \frac{1}{2d_2}\{\boldsymbol{r_2} \cdot \hat{x} - \cot\alpha_0 \cdot (\boldsymbol{r_2} \cdot \hat{y})\} \\
&\quad - \frac{1}{2(d_1 + d_2)}(\boldsymbol{r_2} - \boldsymbol{r_1}) \cdot \hat{x},
\end{aligned} \tag{5.21}
$$

$$D_h = \frac{\sin(\pi/\gamma)e^{-j\frac{\pi}{4}}}{\gamma\sqrt{2\pi k \sin\alpha_0}} \cdot \frac{2}{\cos(\pi/\gamma) + 1}, \tag{5.22}$$

$$e^{-jk(\rho+s)} \cong e^{-jk(d_1+d_2)} \cdot e^{jk(\boldsymbol{r_1}-\boldsymbol{r_2})\cdot\hat{x}}\left[1 - jk\frac{\{(\boldsymbol{r_2}-\boldsymbol{r_1})\cdot\hat{y}\}^2}{2(d_1+d_2)}\right], \tag{5.23}$$

$$
\begin{aligned}
g &\cong (\boldsymbol{K_{m2}}^* \cdot \hat{y})(\boldsymbol{K_{m1}} \cdot \hat{y}) \\
&\quad - \frac{(\boldsymbol{r_2}-\boldsymbol{r_1})\cdot\hat{y}}{d_1+d_2}\{(\boldsymbol{K_{m2}}^* \cdot \hat{x})(\boldsymbol{K_{m1}} \cdot \hat{y}) + (\boldsymbol{K_{m2}}^* \cdot \hat{y})(\boldsymbol{K_{m1}} \cdot \hat{x})\}.
\end{aligned} \tag{5.24}
$$

In the above approximations, we have used the following formulas:

$$\hat{\beta}_1 = (\hat{s} \cdot \hat{y})\hat{x} - (\hat{s} \cdot \hat{x})\hat{y}, \tag{5.25}$$

$$= -\hat{\beta}_2, \tag{5.26}$$

$$\hat{s} \cdot \hat{x} \cong 1 - \frac{\{(\boldsymbol{r_2}-\boldsymbol{r_1})\cdot\hat{y}\}^2}{2(d_1+d_2)^2} \cong 1, \tag{5.27}$$

$$\hat{s} \cdot \hat{y} \cong \frac{(\boldsymbol{r_2}-\boldsymbol{r_1})\cdot\hat{y}}{d_1+d_2}. \tag{5.28}$$

Employing formulas in Appendix D, we finally obtain the following result:

$$Y_{21} \cong PD_h\frac{e^{-jk(d_1+d_2)}}{\sqrt{d_1 d_2 (d_1 + d_2)}}Q, \tag{5.29}$$

$$
\begin{aligned}
Q &= A_1 \cos\phi_{10} \cdot \cos\phi_{20} \\
&\quad + \frac{1}{kd_1}(A_2\cos\phi_{10}\cdot\cos\phi_{20} + A_3\sin\phi_{10}\cdot\cos\phi_{20}) \\
&\quad + \frac{1}{kd_2}(A_2\cos\phi_{10}\cdot\cos\phi_{20} + A_3\cos\phi_{10}\cdot\sin\phi_{20}) \\
&\quad + \frac{A_4\sin\phi_{10}\cdot\sin\phi_{20}}{k(d_1+d_2)},
\end{aligned} \tag{5.30}
$$

$$P = \frac{\pi k\bar{a}^2 j}{4\eta}\left\{\frac{J_1(k_{11}\bar{a})}{J_1(k_{11}\rho_0)}\right\}^2,$$

$$A_1 = \{J_0(k\bar{a}) - J_2(k\bar{a})\}^2,$$

$$A_2 = \frac{(k\bar{a})^2 j}{2}\{J_0(k\bar{a}) - J_2(k\bar{a})\}\left\{J_0(k\bar{a}) + \left(1 - \frac{2}{(k\bar{a})^2}\right)J_2(k\bar{a})\right\},$$

$$A_3 = -j\cot\alpha_0 \cdot \{J_0(k\bar{a}) - J_2(k\bar{a})\}J_2(k\bar{a}),$$

$$A_4 = -4jJ_0(k\bar{a})J_2(k\bar{a}).$$

It is noted that the above approximate formula of Y_{21} can be applied to H-plane coupled elements as well as E-plane coupled elements. Y_{21} does not vanish when MSAs are coupled by H-plane because we have summed up every coupling between infinitesimal equivalent magnetic current elements, as can be seen in Fig.5.2. Thus the expression is considered to be of the second order approximation. It is also noted that the first order term in the above expression of Y_{21} can be interpreted as the product of the radiation pattern of each MSA in the direction of the edge corrected with GTD propagator. The aspect will be extensively studied in Chapter 6 in a general framework of the first order approximation.

In the case that MSAs are on the same ground plane where the coupling is due to the GO waves, use of the half space Green's function with an analogous analysis gives the following result [57]:

$$Y_{21} \cong \left\{ C_1 \frac{1}{kd} + C_2 \frac{1}{(kd)^2} \right\} e^{-jkd} \cos \phi_{10} \cdot \cos \phi_{20} + C_3 \frac{e^{-jkd}}{(kd)^2} \sin \phi_{10} \cdot \sin \phi_{20}, \quad (5.31)$$

$$C_0 = \frac{\pi(k\bar{a})^2 j}{2\eta} \left\{ \frac{J_1(k_{11}\bar{a})}{J_1(k_{11}\rho_0)} \right\}^2,$$
$$C_1 = C_0 \{ J_0(k\bar{a}) - J_2(k\bar{a}) \}^2,$$
$$C_2 = C_0 \{ (k\bar{a})^2 - 1 \} [\{ J_0(k\bar{a}) \}^2 - \{ J_2(k\bar{a}) \}^2],$$
$$C_3 = 2C_0 j [\{ J_0(k\bar{a}) \}^2 + \{ J_2(k\bar{a}) \}^2],$$

where the geometry of MSAs is the same as those in Fig.5.2 except for absence of the fictitious wedge and d being treated as the distance between the MSAs. The expression has the second order asymptotic approximation with respect to $kd \to \infty$.

The mutual coupling coefficient S_{21} between two elements is calculated as follows:

$$S_{21} = \frac{-2(Y_{21}/Y)}{(1 + Y_{11}/Y)^2 - (Y_{21}/Y)^2}, \quad (5.32)$$

where Y_{11} is the self admittance of MSA calculated by the conventional methods [7][56], and Y is the characteristic admittance of transmission line.

5.3 Antenna coupling

It is appropriate to define antenna isolation S_{Ai} between arrays on a polyhedron structure as the mutual couplings between a radiating element i in one array and all radiating elements of the other array A, because interference occurs between them.

S_{Ai} is calculated as follows:

$$S_{Ai} = \sum_{n \in A} S_{ni} I_n, \quad (5.33)$$
$$I_n = \tilde{I}_n e^{j\tilde{\phi}_n}, \qquad \sum_{n \in A} |I_n|^2 = 1, \quad (5.34)$$

where n is a number of radiating elements in the array A, the sum $\sum_{n \in A}$ runs over all the radiating elements in A, S_{ni} is the mutual coupling between radiating element n in the array A and the radiating element i in the array B, $\tilde{I}_n$ is an exciting amplitude, and $\tilde{\phi}_n$ is an exciting phase of n. In the above expressions, we assume that the exciting power for the array A is normalized by a unit power.

5.4 Experimental verification

Figsures 5.3 and 5.4 show the configuration of the experiment. The scatterer is a rectangular parallelepiped which has the size of $36\lambda \times 36\lambda \times 55\lambda$, where λ is the operating wavelength. A linearly polarized circular MSA array is mounted on the face A, and an isolated MSA which has the same characteristics of the element in A is mounted on the other face B separated by a wedge. E-plane and E-plane coupling is chosen throughout the measurement. Figure 5.5 shows the size and physical parameters of the MSA. The array has 25dB sidelobe levels by means of a deterministic density tapering method [58] with 128 exciting elements as shown in Fig.5.6. The signal from a network analyzer is amplified by a linear amplifier and is divided into 128 phase shifters. The output port of the isolated MSA is connected to the other port of the network analyzer. The experiment has been carried out in an anechoic chamber.

Figure 5.3 shows the direction of main beam of the array. The mutual couplings between the array and the MSA have been measured for the beam scan within a range of $-90° \le \theta \le 90°$. The measurement has been carried out at one degree step, and time fluctuation of the measured signal at every θ has been averaged by utilizing the function of the network analyzer.

Figure 5.7 shows a comparison between the measured and calculated values. Good agreement between them supports the theory.
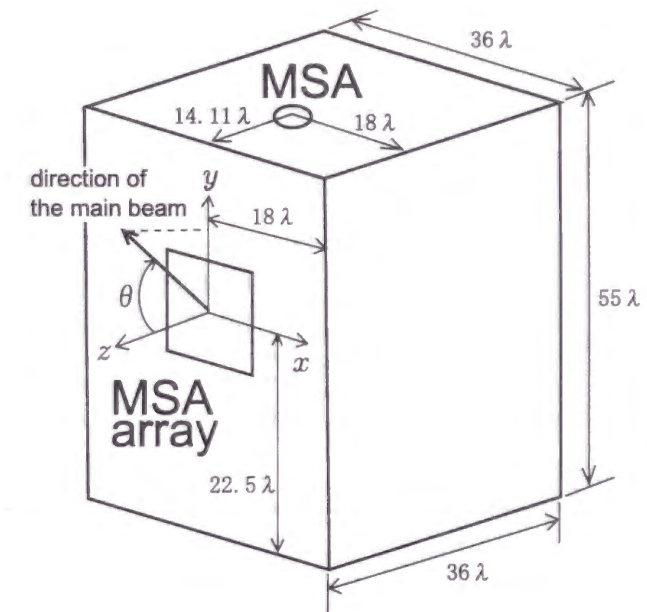
Figure 5.3: Antennas on a polyhedron used in the experiment.
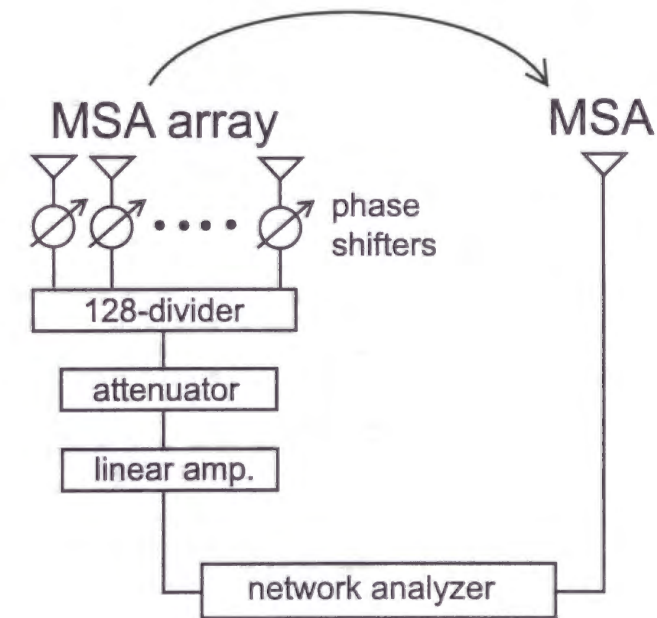
Figure 5.4: Configuration of the experiment.

0. 029 λ

0. 053 λ

feeding point

0. 182 λ

$\varepsilon_r = 2.2$
$\tan \delta = 0.0009$
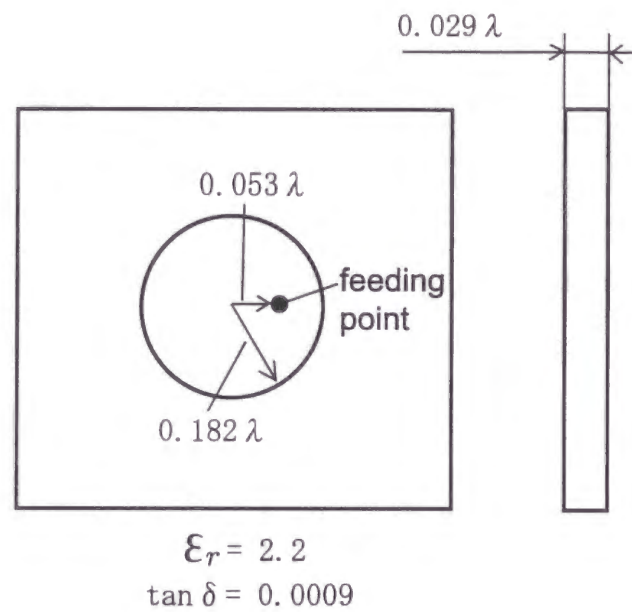
Figure 5.5: Physical parameters of the microstrip antenna.

■ – exciting element

0.24 λ

0.48 λ
0.97 λ

0.14 λ

0.28 λ
0.56 λ
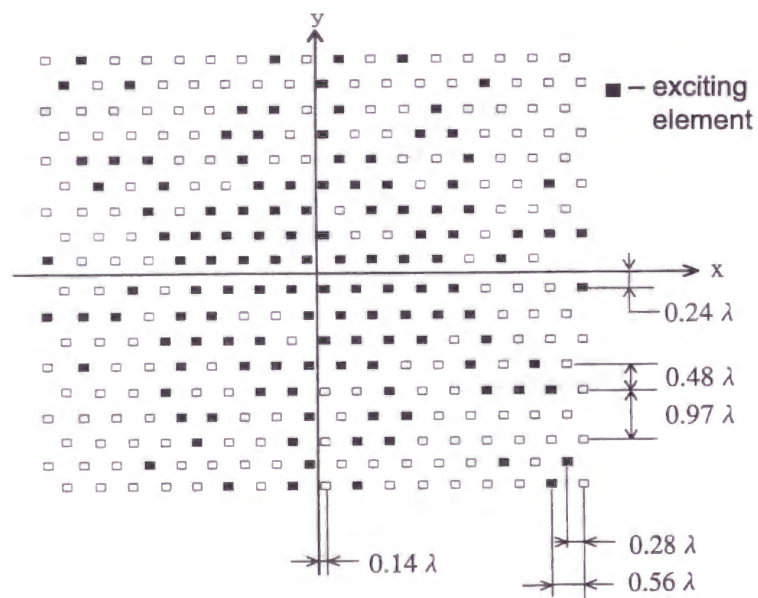
Figure 5.6: Thinning map of the array.
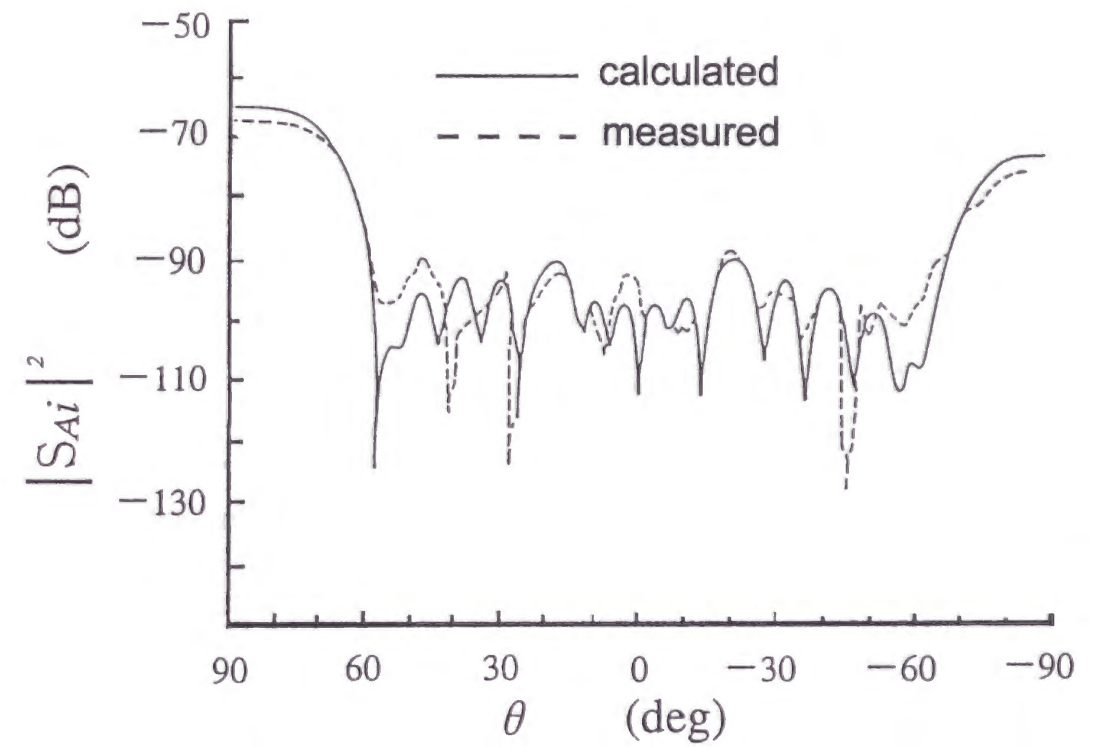
Figure 5.7: Comparison between calculated and measured values.

5.5 Numerical simulations

Some numerical simulations are given to clarify the characteristics of antenna coupling between arrays on a polyhedron structure.

Figure 5.8 shows a simulation model. Two arrays are mounted on a conducting polyhedron. Each array has 900 linearly polarized circular MSAs, where 30×30 radiating elements are arranged in a square lattice of 0.5λ spacing. The size and physical parameters of the MSA are the same as those of Fig.5.5. The antenna coupling S_{2i} is defined as the mutual coupling between radiating element i in the array 1 and all radiating elements in the array 2. The array 2 is excited with a unit power, and the two arrays are coupled by E-plane. In Fig.5.8, θ and ϕ define the direction of the main beam of the array 2. Figure 5.9 shows examples of the simulation with parameters $\phi = 0°, D = 20\lambda$, and $D = 40\lambda$. For each D, five cases of θ are plotted. In Fig.5.9, points of the lattice represent the radiating elements in the array 1. Figure 5.10 shows antenna couplings for radiating element i_0 which is the nearest element to the array 2 (see Fig.5.8). In Fig.5.10, θ is varied continuously within the range of $-90° \leq \theta \leq 90°$. Figure 5.11 shows the case that the beam of the array 2 is steered to a different direction $\phi = 90°$.

From the above results, some characteristics of the antenna coupling are known. As shown in Fig.5.10, S_{2i_0} increases when θ is steered to wide angles. The reason is described as follows: When θ in Fig.5.8 is steered to wide angles, the field from the shoulder of the main beam of the array 2 becomes incident to the wedge between the array 2 and i_0. Then intensity of the diffracted field becomes high. As seen in Fig.5.10, the same phenomenon is observed around $\theta = -90°$. The reason is that the spacing of the elements in the array 2 is 0.5λ, a grating lobe arises at the direction $\theta = +90°$ when the beam is steered at $\theta = -90°$. As seen from Fig.5.9, the other elements in the array 1 have almost the same characteristics as those of i_0 described above. When the beam is steered to a direction

around which the array 1 does not exist ($\phi = 90°$), S_{2i_0} becomes remarkably weak as shown in Fig.5.11, because intensity of the incident fields to the wedge between the array 1 and the array 2 becomes weak in this case. From the above observation, it is concluded that sidelobe level of the antenna array in the direction of the wedge gives significant contribution the coupling. Therefore, null beam forming or low sidelobe operation in that direction is applicable to obtaining good isolation characteristics.
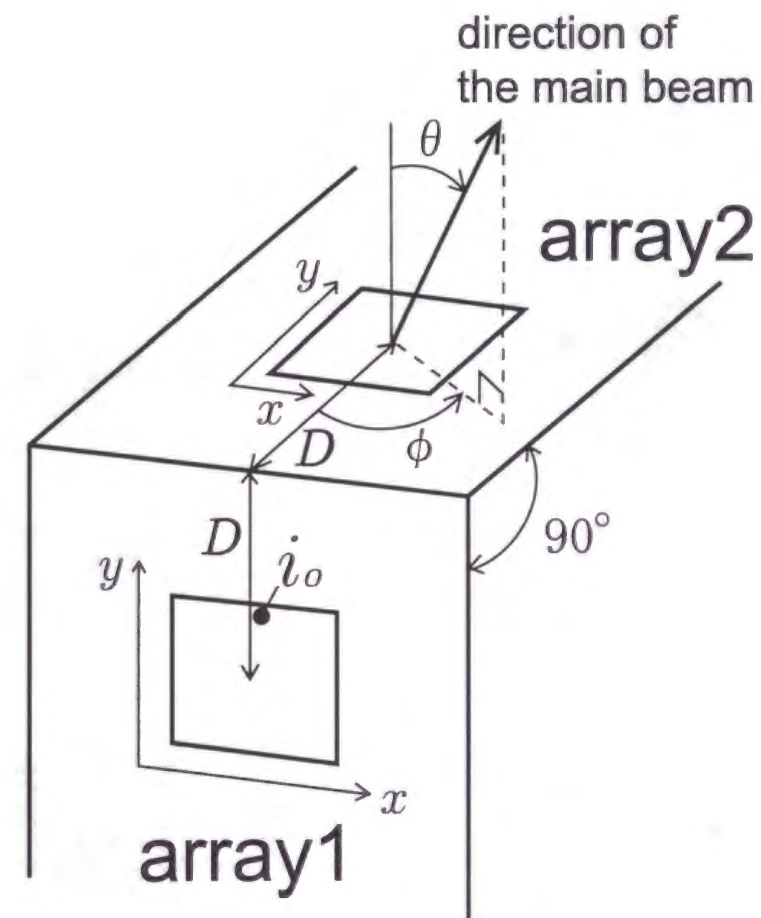
Figure 5.8: Simulation model.
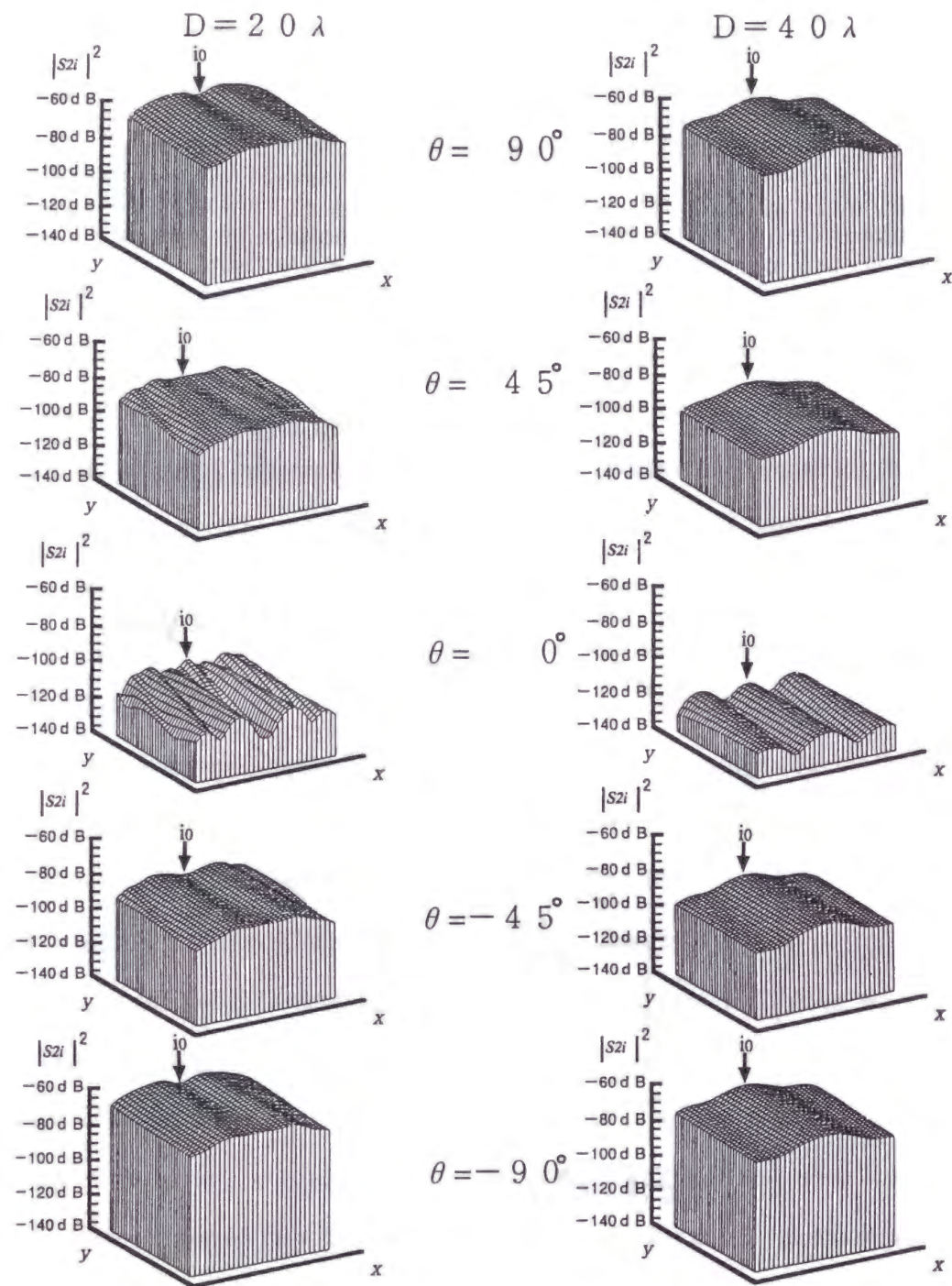
Figure 5.9: The antenna coupling between arrays.
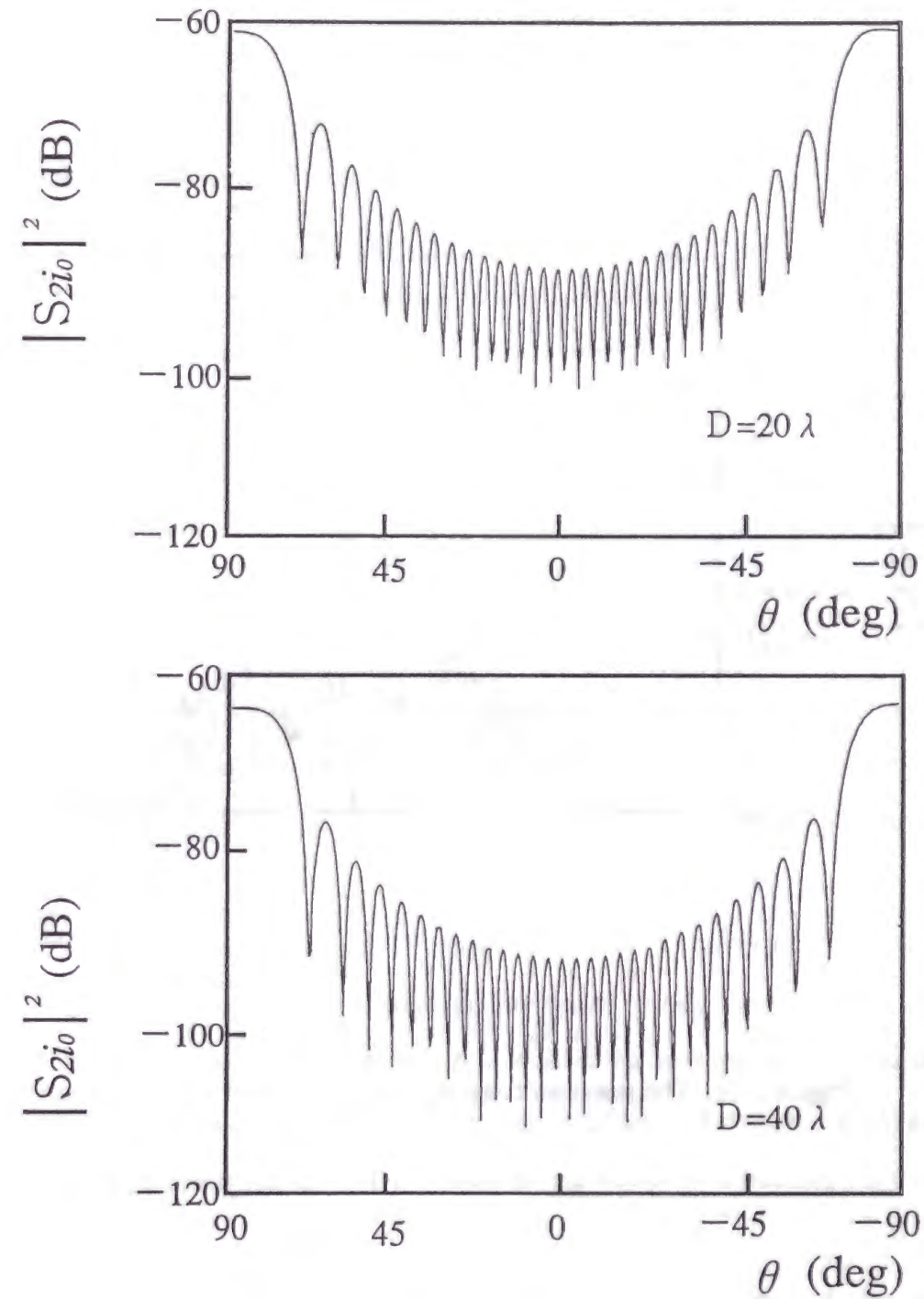
Figure 5.10: The antenna coupling between i_0 and array 2 ($\phi = 0°$).
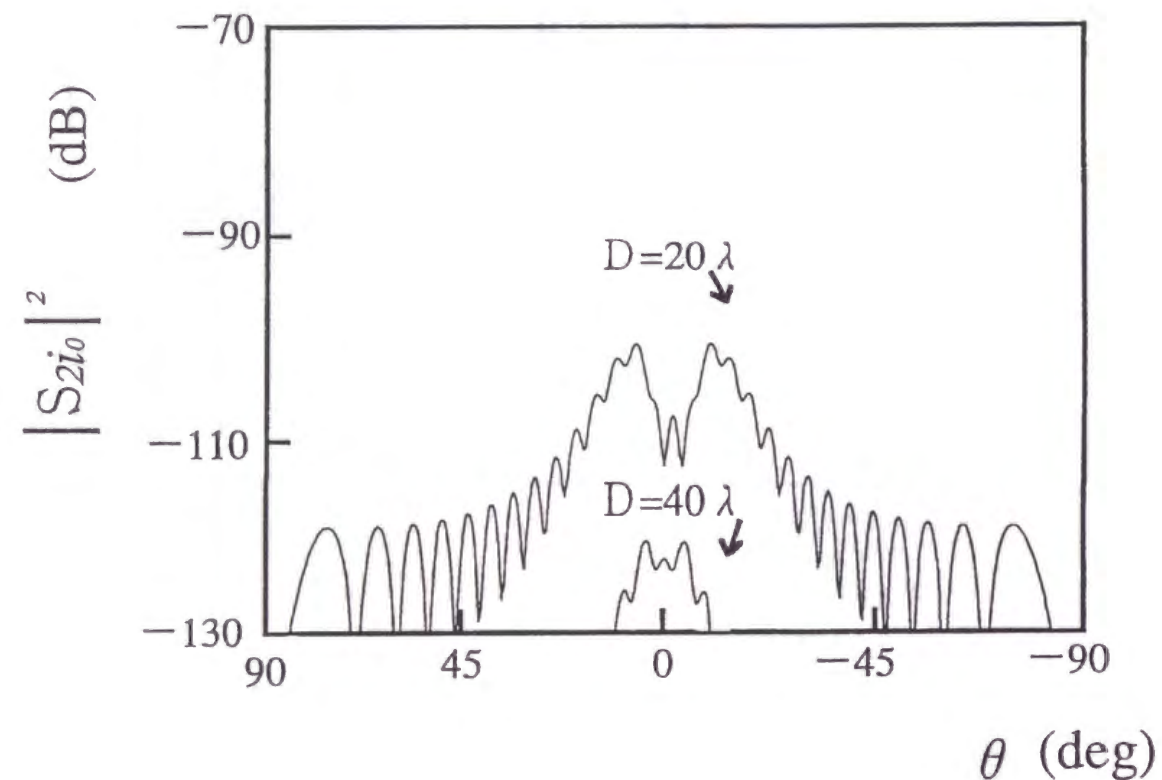
Figure 5.11: The antenna coupling between i_0 and array 2 ($\phi = 90°$).

5.6 Summary

An analysis is carried out for antenna coupling between arrays on a polyhedron structure. The antenna coupling is treated as mutual couplings between a radiating element in one array and all radiating elements in the other array. To deal with a large number of pairs of the radiating elements, an approximate formula is developed for the mutual admittance between circular MSAs separated by a wedge. The MSAs are treated by the cavity model and the diffracted field is expressed by mean of GTD. Approximate analytical evaluation of the mutual admittance integral is achieved for the case that the radius of MSA small is compared with the distances in the geometry. The resultant expression is of a simple closed form with the second order approximation which is applicable to H-plane and H-plane coupling as well as E-plane and E-plane coupling between the MSAs. The expression is also given in the case of MSAs on the same ground plane with the same order of approximation. For experimental verification of the method, the mutual couplings are measured between MSA and a phased array which has 128 circular MSA elements located on different faces of a polyhedron. Good agreement is observed between the measured level of coupling in the period of beam steering of the array and calculated level by the theory. Several numerical simulations are given to understand properties of the antenna coupling. It is concluded that sidelobe level of the antenna array in the direction of the wedge gives significant contribution to the coupling. Therefore, null beam forming or low sidelobe operation in that direction is applicable to obtaining good isolation characteristics.

The effect of antenna farm can be adequately treated by means of the analytical modeling developed in this chapter.

Chapter 6

Simple Expression of Antenna Coupling by Using a Product of Radiation Patterns

6.1 Introduction

In this chapter, a simple and general first order expression of mutual impedance and admittance is derived for arbitrary class of antennas modeled by equivalent currents [60]. The dominant terms of the mutual admittances in Chapter 5 is recovered within the framework of this scheme.

The analysis of mutual couplings in antenna arrays [1] is, in general, difficult due to the limitation of computational time. In addition, varieties of radiating elements have varieties of analytical expressions, where most of the formulas are complicated and require some efforts to develop software for specific problems. Some universal treatments of the antenna coupling should be sought to realize the efficient computation. One idea is employment of far field approximations for largely separated radiating elements. Friis [61] developed a simple formula, known as *the Friis Transmission Formula*, through his physical insight by using the energy conservation argument. The usefulness of the formula

is, no doubt, for designing of link budget in communications and radar systems, while it lacks the information of phase. Some extensions of the transmission formula in the Friis' form which contain the phase terms and antenna polarization are reported [62][63]. The Fresnel approximation can be employed for the mutual impedance and admittance integrals given by the EMF method [4][5]. Although the resultant expressions appear to be of simple forms, direct physical interpretations of field quantities are lost in contrast to those in the Friis' form. Some intermediate forms of the integral applicable to general antennas should be sought.

In the following sections, the first order universal relations are developed for the problem by using the far field approximation.

In Section 6.2, the far fields of the current elements are given with an introduction of dyadic decompositions of the field quantities with respect to ray coordinates.

In Section 6.3, decomposition of the mutual impedance and admittance integrals are studied analogous to the Friis' form for arbitrary antennas with their given equivalent currents. The reaction integral [64][65] between two antennas is employed for the expression, and far field approximations are made. The developed formulas are of the form, *a product of radiation patterns multiplied by a free space propagator and divided by the voltages or the currents at the feeding points of the two antennas.*

In Section 6.4, the antenna coupling under the presence of a wedge is treated as an extension of the theory through a modification of the propagator by using GTD [14].

In Section 6.5, two cases of MSAs on a ground plane and on a polyhedron structure are treated for the application of the theory, and experimental verification is given.

In Section 6.6, a summary of this chapter is given.

6.2 Far fields of current elements

Consider an electric current element $\boldsymbol{J}(\boldsymbol{r}')$ and a magnetic current element $\boldsymbol{M}(\boldsymbol{r}')$, as shown Fig.6.1, located at $\boldsymbol{r}'$, the far fields $\boldsymbol{E}(\boldsymbol{r})$ and $\boldsymbol{H}(\boldsymbol{r})$ of the currents are given as follows [2][5] with $e^{j\omega t}$ dependence of field quantities:

$$\boldsymbol{E}(\boldsymbol{r}) = \boldsymbol{E_A}(\boldsymbol{r}) + \boldsymbol{E_F}(\boldsymbol{r}), \tag{6.1}$$

$$\boldsymbol{H}(\boldsymbol{r}) = \boldsymbol{H_A}(\boldsymbol{r}) + \boldsymbol{H_F}(\boldsymbol{r}), \tag{6.2}$$

$$\boldsymbol{E_A}(\boldsymbol{r}) \simeq -j\omega \boldsymbol{A_T}(\boldsymbol{r}), \tag{6.3}$$

$$\boldsymbol{E_F}(\boldsymbol{r}) \simeq j\omega\eta\hat{s} \times \boldsymbol{F}(\boldsymbol{r}), \tag{6.4}$$

$$\boldsymbol{H_A}(\boldsymbol{r}) \simeq -j\frac{\omega}{\eta}\hat{s} \times \boldsymbol{A}(\boldsymbol{r}), \tag{6.5}$$

$$\boldsymbol{H_F}(\boldsymbol{r}) \simeq -j\omega \boldsymbol{F_T}(\boldsymbol{r}), \tag{6.6}$$

$$\boldsymbol{A_T}(\boldsymbol{r}) = (\mathbf{1} - \hat{s}\hat{s}) \cdot \boldsymbol{A}(\boldsymbol{r}), \tag{6.7}$$

$$\boldsymbol{F_T}(\boldsymbol{r}) = (\mathbf{1} - \hat{s}\hat{s}) \cdot \boldsymbol{F}(\boldsymbol{r}), \tag{6.8}$$

$$\boldsymbol{A}(\boldsymbol{r}) = \frac{\mu_0}{4\pi}\frac{e^{-jkR}}{R}\boldsymbol{J}(\boldsymbol{r}'), \tag{6.9}$$

$$\boldsymbol{F}(\boldsymbol{r}) = \frac{\varepsilon_0}{4\pi}\frac{e^{-jkR}}{R}\boldsymbol{M}(\boldsymbol{r}'), \tag{6.10}$$

$$R = |\boldsymbol{r} - \boldsymbol{r}'|, \tag{6.11}$$

$$\hat{s} = \frac{\boldsymbol{r} - \boldsymbol{r}'}{R}, \tag{6.12}$$

$$\eta = \sqrt{\frac{\mu_0}{\varepsilon_0}}, \qquad k = \omega\sqrt{\mu_0\varepsilon_0}, \tag{6.13}$$

where $\boldsymbol{A}$ and $\boldsymbol{F}$ represent vector potentials with respect to $\boldsymbol{J}$ and $\boldsymbol{M}$, and ε_0 and μ_0 are permittivity and permeability of free space, respectively.
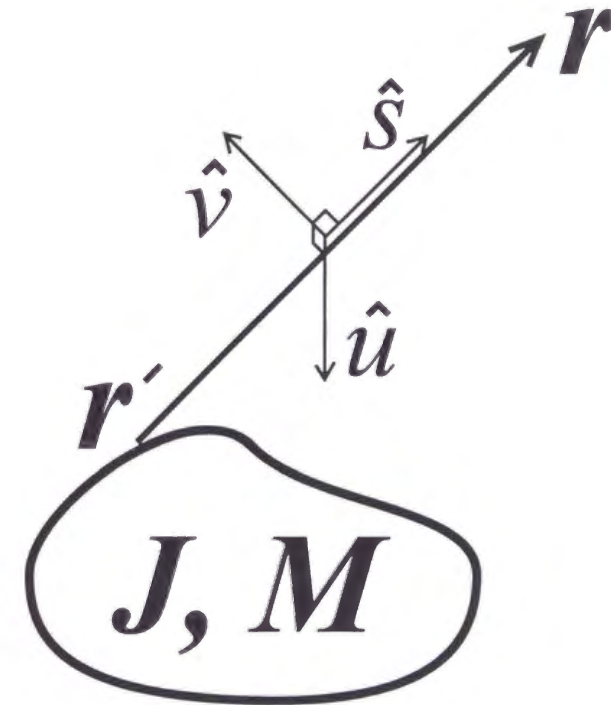
Figure 6.1: Currents and ray coordinates.

We introduce a ray coordinate system $(\hat{v}, \hat{u}, \hat{s})$ and define the following two dyadic operators $\bar{P}$ and $\bar{\Gamma}$:

$$\bar{P} = \mathbf{1} - \hat{s}\hat{s} = \hat{u}\hat{u} + \hat{v}\hat{v}, \tag{6.14}$$

$$\bar{\Gamma} = \hat{u}\hat{v} - \hat{v}\hat{u} \equiv \hat{s} \times \cdot \quad, \tag{6.15}$$

$$\hat{s} = \hat{v} \times \hat{u}, \tag{6.16}$$

$$\hat{v} = \hat{u} \times \hat{s}, \tag{6.17}$$

$$\hat{u} = \hat{s} \times \hat{v}, \tag{6.18}$$

where $\bar{P}$ acts as a projection operator transverse to $\hat{s}$, and $\bar{\Gamma}$ represents a vector product operation with respect to $\hat{s}$. It is noted that the transverse vectors $\hat{v}$ and $\hat{u}$ can be chosen in any rotation angles with respect to $\hat{s}$ if the conditions (6.16) to (6.18) are satisfied. Now (6.3) to (6.6) are rewritten as follows:

$$E_A = \eta \tilde{g} \bar{P} \cdot J, \tag{6.19}$$

$$E_F = -\tilde{g} \bar{\Gamma} \cdot M, \tag{6.20}$$

$$H_A = \tilde{g} \bar{\Gamma} \cdot J, \tag{6.21}$$

$$H_F = \frac{\tilde{g}}{\eta} \bar{P} \cdot M, \tag{6.22}$$

$$\tilde{g} = \frac{k}{4\pi j} \frac{e^{-jkR}}{R}. \tag{6.23}$$

Let X and Y be vectors like J and M, the following relations are easily obtained and will be used later:

$$X \cdot \bar{P} \cdot Y = (\bar{P} \cdot X) \cdot (\bar{P} \cdot Y), \tag{6.24}$$

$$X \cdot \bar{\Gamma} \cdot Y = (\bar{P} \cdot X) \cdot (\bar{\Gamma} \cdot Y). \tag{6.25}$$

6.3 Simple expression of antenna coupling

Let us consider two antennas named 1 and 2 both located in free space as shown in Fig.6.2. The mutual impedance Z_{21} and admittance Y_{21} between the two antennas are calculated by the reaction integral, where the expressions are stationary with respect to field quantities as follows [2][65]:

$$Z_{21} = -\frac{1}{I_1 I_2} < 1, 2 >, \tag{6.26}$$

$$Y_{21} = \frac{1}{V_1 V_2} < 1, 2 >, \tag{6.27}$$

$$< 1, 2 > = \int_{v_1} d\mathbf{r}_1 \int_{v_2} d\mathbf{r}_2 (J_2 \cdot E^{(1)} - M_2 \cdot H^{(1)}). \tag{6.28}$$

In the above formulas, the antennas are modeled by the equivalent electric and magnetic current elements J_1, M_1, J_2, and M_2 where the subscripts 1 and 2 represent the quantity with respect to antennas 1 and 2, respectively, and the convention is utilized throughout the chapter. $E^{(1)}$ and $H^{(1)}$ are electric and magnetic fields of the form (6.1) and (6.2), respectively, which are radiated by J_1 and M_1 of antenna 1 and received by antenna 2. The domains of integrations in (6.28) are the volumes v_1 and v_2 of the two antennas. I_i and V_i, $i \in \{1, 2\}$ are the current and the voltage applied at the feeding point of antenna i, respectively. If the exact current elements are known, (6.28) gives the exact value. However, in practical applications, use of approximate forms of current elements may approximate (6.28) like those of the EMF method and the aperture distribution method by using the Huygens principle with respect to closed surfaces surrounding each antenna. For example, the former may be suited for dipoles and the latter may be applicable to horn antennas.
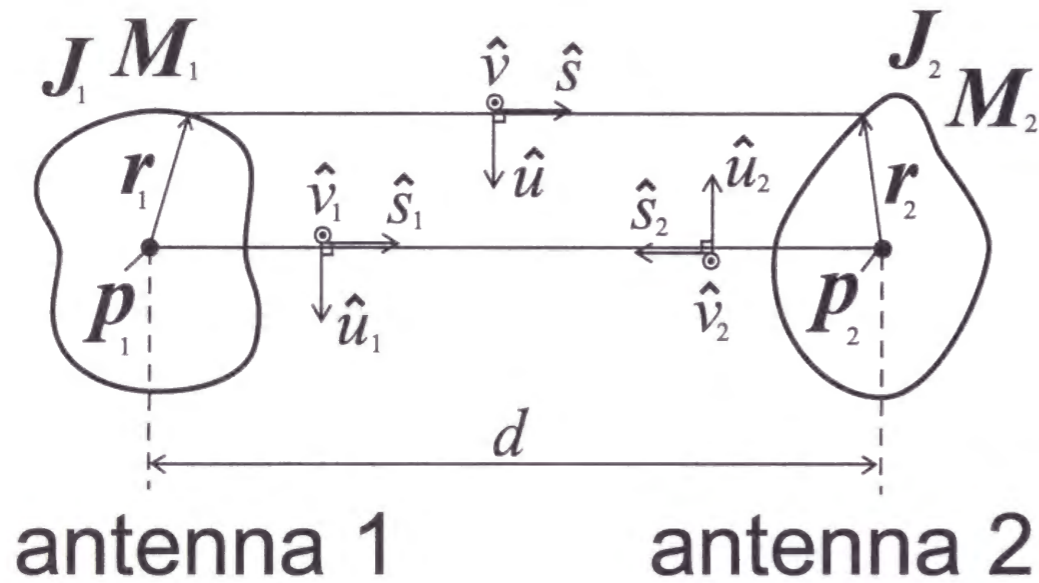
Figure 6.2: Coordinates of two antennas.

If the two antennas are located in the far zone to each other, a simple expression can be derived for the reaction integral (6.28) by using the far field approximations. The result is as follows:

$$< 1, 2 > \quad \simeq \quad \frac{g}{\eta} \boldsymbol{e_2^J} \cdot \boldsymbol{e_1^J} - \eta g \boldsymbol{h_2^M} \cdot \boldsymbol{h_1^M} - \eta g \boldsymbol{h_2^M} \cdot \boldsymbol{h_1^J} + \frac{g}{\eta} \boldsymbol{e_2^J} \cdot \boldsymbol{e_1^M}, \qquad (6.29)$$

$$\boldsymbol{e_i^J} \quad = \quad \eta \int_{v_i} d\boldsymbol{r_i} \bar{P}_i \cdot \boldsymbol{J_i}(\boldsymbol{r_i}) \exp(jk\hat{s}_i \cdot \boldsymbol{r_i}), \qquad (6.30)$$

$$\boldsymbol{h_i^M} \quad = \quad \frac{1}{\eta} \int_{v_i} d\boldsymbol{r_i} \bar{P}_i \cdot \boldsymbol{M_i}(\boldsymbol{r_i}) \exp(jk\hat{s}_i \cdot \boldsymbol{r_i}), \qquad (6.31)$$

$$\boldsymbol{e_i^M} \quad = \quad - \int_{v_i} d\boldsymbol{r_i} \bar{\Gamma}_i \cdot \boldsymbol{M_i}(\boldsymbol{r_i}) \exp(jk\hat{s}_i \cdot \boldsymbol{r_i}), \qquad (6.32)$$

$$\boldsymbol{h_i^J} \quad = \quad \int_{v_i} d\boldsymbol{r_i} \bar{\Gamma}_i \cdot \boldsymbol{J_i}(\boldsymbol{r_i}) \exp(jk\hat{s}_i \cdot \boldsymbol{r_i}), \qquad (6.33)$$

$$g \quad = \quad \frac{k}{4\pi j} \frac{e^{-jkd}}{d}, \qquad (6.34)$$

$$d \quad = \quad |\boldsymbol{p_2} - \boldsymbol{p_1}|, \qquad (6.35)$$

$$\hat{s}_1 \quad = \quad \frac{\boldsymbol{p_2} - \boldsymbol{p_1}}{d}, \qquad (6.36)$$

$$\hat{s}_2 \quad = \quad -\hat{s}_1, \qquad (6.37)$$

where $\boldsymbol{p_1}$ and $\boldsymbol{p_2}$ are the reference points of antennas 1 and 2. The distance d between them and the unit vector $\hat{s}_1$ from antennas 1 to 2 are defined as in (6.35) and (6.36), respectively. The reference points can be chosen freely and conveniently so as to define the center points of antennas. $\bar{P}_i$ and $\bar{\Gamma}_i$ represent (6.14) and (6.15), respectively, where $(\hat{v}, \hat{u}, \hat{s})$ are replaced with $(\hat{v}_i, \hat{u}_i, \hat{s}_i)$, and g is the free space propagator between the two antennas. The formulas (6.30) to (6.33) are radiation patterns of antenna i in the direction of $\hat{s}_i$, where $\boldsymbol{e}_i^X$ and $\boldsymbol{h}_i^X$, $X \in \{J, M\}$ represent the electric and magnetic field patterns of source $X \in \{J, M\}$, respectively. The terms in (6.29) are interpreted as products of radiation patterns, in the direction of the two antennas seeing each other, multiplied by the free space propagator g and constants η or $1/\eta$. The last constants guarantee the dimension of $< 1, 2 >$ being power if we introduce the circuit correspondence of the

electric and magnetic fields as the voltage and current, respectively.

We briefly describe the derivation of (6.29) in the case of the first term as an example. The term comes from $\boldsymbol{J_2} \cdot \boldsymbol{E}_A^{(1)}$. The component of the reaction integral is calculated by using the far field approximation as follows:

$$
\begin{aligned}
\int_{v_1} d\boldsymbol{r_1} \int_{v_2} d\boldsymbol{r_2} \boldsymbol{J_2} \cdot \boldsymbol{E}_A^{(1)} &= \eta \int_{v_1} d\boldsymbol{r_1} \int_{v2} d\boldsymbol{r_2} \tilde{g} \boldsymbol{J_2} \cdot \bar{P}_1 \cdot \boldsymbol{J_1}, &(6.38) \\
&\simeq \eta g \int_{v_1} d\boldsymbol{r_1} \int_{v2} d\boldsymbol{r_2} e^{jk\hat{s}_2 \cdot \boldsymbol{r_2}} \boldsymbol{J_2} \cdot \bar{P}_1 \cdot \boldsymbol{J_1} e^{jk\hat{s}_1 \cdot \boldsymbol{r_1}}, &(6.39) \\
&= \frac{g}{\eta} \left(\eta \int_{v2} d\boldsymbol{r_2} e^{jk\hat{s}_2 \cdot \boldsymbol{r_2}} \bar{P}_2 \cdot \boldsymbol{J_2} \right) \cdot \left(\eta \int_{v1} d\boldsymbol{r_1} e^{jk\hat{s}_1 \cdot \boldsymbol{r_1}} \bar{P}_1 \cdot \boldsymbol{J_1} \right), & \\
& &(6.40) \\
&= \frac{g}{\eta} \boldsymbol{e_2^J} \cdot \boldsymbol{e_1^J}. &(6.41)
\end{aligned}
$$

In (6.38) the following approximations are employed to derive (6.39):

$$
\begin{aligned}
\hat{s} &\simeq \hat{s}_1 = -\hat{s}_2, &(6.42) \\
\tilde{g} &\simeq \frac{k}{4\pi j} \frac{e^{-jk\{d+\hat{s}_1 \cdot (\boldsymbol{r_2}-\boldsymbol{r_1})\}}}{d}, &(6.43) \\
&= g e^{jk(\hat{s}_2 \cdot \boldsymbol{r_2}+\hat{s}_1 \cdot \boldsymbol{r_1})}, &(6.44)
\end{aligned}
$$

where $\hat{s}$ in (6.12) is approximately replaced by (6.36) under the condition (6.45) below. The factorization in (6.40) is carried out through the relation (6.24). The other terms in (6.29) are analogously obtained by using (6.24), (6.25), and (6.42) to (6.44).

The condition of validity of the far field approximations is described as follows:

$$
\max(|\boldsymbol{r_1}|)/d \ll 1, \quad \text{and} \quad \max(|\boldsymbol{r_2}|)/d \ll 1, \tag{6.45}
$$

where $\max(|\boldsymbol{r_i}|)$, $i \in \{1, 2\}$ is defined as the absolute maximum of the displacement vector $\boldsymbol{r_i}$ around $\boldsymbol{p_i}$ in each volume v_i of the integral (6.38). Although the theory correctly gives contribution of the field to the $1/d$ order for any type of antennas, it is noted that the theory always gives zero value if one of the radiation patterns is zero in the direction of the other antenna. In the case of antennas being closely spaced and the $1/d^2$ order or the

higher order contributions of the field are dominant, the theory cannot be applied. For example, E-plane and E-plane coupling of nearby dipoles on the same plane, H-plane and H-plane coupling of nearby MSAs on the same ground plane, ... *etc.* should be treated by some other theories including the contribution of near field terms. Even if the $1/d$ term does not disappear, *i.e.* the radiation pattern is not zero, the present theory gives erroneous values if the near field terms are predominant in the coupling. Thus the theory should be applied to the antennas well separated so as to satisfy the condition of (6.45).

6.4 Antenna coupling under the presence of a wedge

In this section, the method developed in the previous section is extended to the case of antennas under the presence of a perfectly conducting wedge. We assume, for simplicity, that the two antennas 1 and 2 are located in the shadow region of the wedge where the diffracted fields are dominant and no GO terms are present. In the case that GO terms exist, each contribution should be separately added by using the free space propagator in the previous section with appropriate ray tracing for direct and reflected waves, where the direction of each ray coordinate of antenna is chosen in accordance with the traced rays.

The diffracted electric and magnetic fields $\boldsymbol{E}^{(1)}$ and $\boldsymbol{H}^{(1)}$ of antenna 1 due to the wedge are given as follows [14]:

$$\boldsymbol{E}^{(1)} = -(\tilde{D}_h\hat{\psi}_2\hat{\psi}_1 + \tilde{D}_s\hat{\beta}_2\hat{\beta}_1)\cdot\boldsymbol{E}_q^{(1)}U, \qquad (6.46)$$

$$\boldsymbol{H}^{(1)} = -(\tilde{D}_s\hat{\psi}_2\hat{\psi}_1 + \tilde{D}_h\hat{\beta}_2\hat{\beta}_1)\cdot\boldsymbol{H}_q^{(1)}U, \qquad (6.47)$$

$$U = \sqrt{\frac{\rho}{s(s+\rho)}}e^{-jks}, \qquad (6.48)$$

$$\tilde{D}_h^s = \frac{\sin(\pi/\gamma)e^{-j\pi/4}}{\gamma\sqrt{2\pi k}\sin\alpha}\left[\frac{1}{\cos(\pi/\gamma) - \cos\{(\psi-\psi')/\gamma\}} \mp \frac{1}{\cos(\pi/\gamma) - \cos\{(\psi+\psi')/\gamma\}}\right], \qquad (6.49)$$

where $\boldsymbol{E}_q^{(1)}$ and $\boldsymbol{H}_q^{(1)}$ are electric and magnetic fields, respectively, of antenna 1 at the diffraction point q of the wedge, $\tilde{D}_s$ and $\tilde{D}_h$ are the Keller's GTD diffraction coefficients, and the rest of the parameters in (6.46) to (6.49) are defined in Fig.6.3.
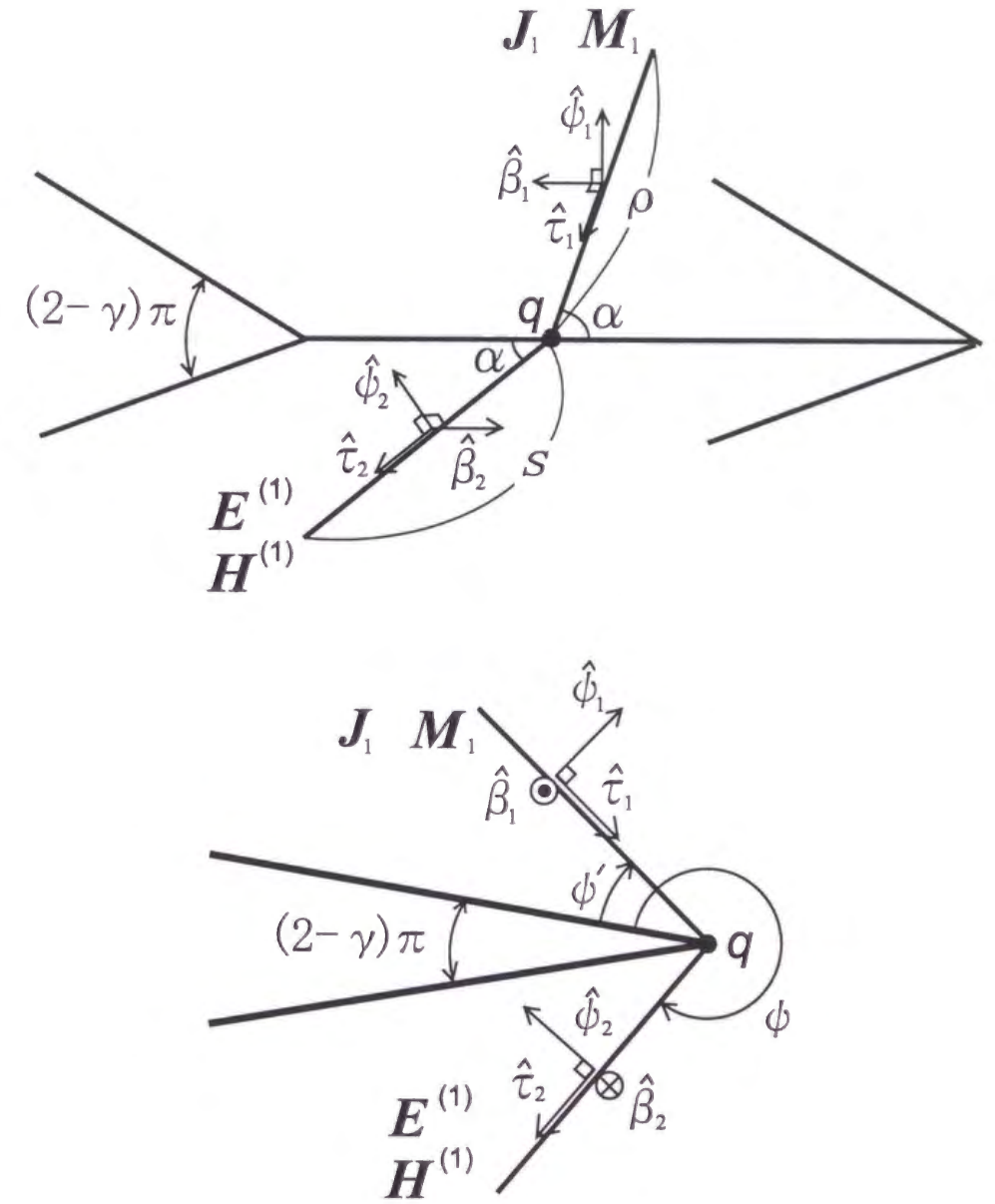
Figure 6.3: Wedge geometry.

The reaction integral (6.28) is approximately expressed as follows:

$$< 1, 2 > \simeq \frac{1}{\eta} \boldsymbol{e_2^J} \cdot \bar{G}_E \cdot \boldsymbol{e_1^J} - \eta \boldsymbol{h_2^M} \cdot \bar{G}_H \cdot \boldsymbol{h_1^M} - \eta \boldsymbol{h_2^M} \cdot \bar{G}_H \cdot \boldsymbol{h_1^J} + \frac{1}{\eta} \boldsymbol{e_2^J} \cdot \bar{G}_E \cdot \boldsymbol{e_1^M},$$

(6.50)

$$\bar{G}_E = -G(D_h \hat{\psi}_2 \hat{\psi}_1 + D_s \hat{\beta}_2 \hat{\beta}_1),$$

(6.51)

$$\bar{G}_H = -G(D_s \hat{\psi}_2 \hat{\psi}_1 + D_h \hat{\beta}_2 \hat{\beta}_1),$$

(6.52)

$$G = \frac{k}{4\pi j} \cdot \frac{e^{jk(d_1+d_2)}}{\sqrt{d_1 d_2 (d_1 + d_2)}},$$

(6.53)

where D_s and D_h represent the value of (6.49) when the center points of the two antennas are used for the GTD ray tracing. As the derivation of (6.50) is analogous to that of (6.29), we omit the proof here.

6.5 Applications

In this section, two applications are given for the analysis of the mutual coupling between circular MSAs.

Consider two MSAs 1 and 2 with the identical radius of a. By using the cavity model [6][7][56], they can be modeled by a circular magnetic currents $\boldsymbol{M}_i$, $i \in \{1, 2\}$ as follows:

$$\boldsymbol{M}_i = K J_1(k_{11}\bar{a}) \cos(\phi' - \phi_i) \delta(\rho' - \bar{a}) \hat{\phi}',$$

(6.54)

$$\bar{a} = a \left\{ 1 + \frac{2h}{a\pi\varepsilon_r} \left(\ln \frac{\pi a}{2h} + 1.7726 \right) \right\}^{1/2},$$

(6.55)

where K is a constant, $\bar{a}$ is the equivalent radius of MSA where $k_{11}\bar{a} = 1.84118$ for the TM$_{11}$ mode operation, h is the thickness of the dielectric material where MSA is printed, ε_r is the relative dielectric constant, (ρ', ϕ', z') is the local coordinate systems of MSA i with the orientation at the center of MSA i where $\hat{\phi}'$ is the unit vector for the angle variable, and ϕ_i is the angle of feeding point of MSA i. The voltage V_i of the feeding point of MSA i is given by the following formula:

$$V_i = K J_1(k_{11}\rho_0)h,$$

(6.56)

where ρ_0 is the radius of feeding point of MSA.

6.5.1 MSAs on a ground plane

For the first application of the theory developed in the previous section, we analyze the mutual coupling between two MSAs on a ground plane as shown in Fig.6.4. From (6.27) and (6.29), the mutual admittance Y_{21} between the two MSAs 1 and 2 is approximately expressed as follows:

$$Y_{21} \simeq -\frac{\eta}{V_1 V_2} \cdot 2g \boldsymbol{h}_2^M \cdot \boldsymbol{h}_1^M, \qquad (6.57)$$

where the half space propagator $2g$ is used to consider the effect of the ground plane. By using (6.54), we have the following formula:

$$\begin{aligned} \boldsymbol{h}_i^M &= \frac{1}{\eta} \int_{v_i} d\boldsymbol{r}_i \bar{P}_i \cdot \boldsymbol{M_i} \exp(jk\hat{s}_i \cdot \boldsymbol{r_i}), \\ &= \frac{K}{\eta} J_1(k_{11}\bar{a}) h \pi \bar{a} \{ J_2(k\bar{a}) - J_0(k\bar{a}) \} \cos \phi_i \cdot \hat{u}_i. \end{aligned} \qquad (6.58)$$

The final expression of Y_{21} is as follows:

$$Y_{21} \simeq \left\{ \frac{J_1(k_{11}\bar{a})}{J_1(k_{11}\bar{\rho}_0)} \right\}^2 \frac{ke^{-jkd}}{2\pi\eta jd} (\pi\bar{a})^2 \{ J_0(k\bar{a}) - J_1(k\bar{a}) \}^2 \cos \phi_1 \cdot \cos \phi_2. \qquad (6.59)$$

It is noted that the above formula recovers the first term of (5.31) in Chapter 5 where an asymptotic expansion with respect to $\bar{a}/d \ll 1$ to the second order is employed in Y_{21}. Thus the present theory correctly gives the first order contribution in the limit $\bar{a}/d \to 0$. The change in sign between (5.31) and (6.59) comes from the difference in definition of the feeding angle of MSA.

Figure 6.5 shows a comparison between the calculated and measured values of $|S_{21}|^2$ between the two MSAs with E-plane and E-plane coupling, $i.e.$ $\phi_1 = 0$ and $\phi_2 = \pi$, where $Y_{11} = 0.0192 + j0.0029$, $Y = 0.02$, $\varepsilon_r = 2.2$, $a = 0.182\lambda$, $\rho_0 = 0.053\lambda$, and $h = 0.029\lambda$ at the operating wavelength λ. The experiment has been carried out in an anechoic chamber with S-parameter measurements by using a network analyzer. In Fig.6.5, the solid line

represents calculated values by the present theory with the contribution of $1/d$ term only, and the broken line represents calculated values due to the EMF method [6][7][56] by assuming the same magnetic current of (6.54) and it includes all the near field terms without the far field approximation. Although significant deviation of values are observed within the region of less than a half wavelength spacing of antennas, the correspondence between the measured and calculated values for well separated spacing is considered to be in good agreement.
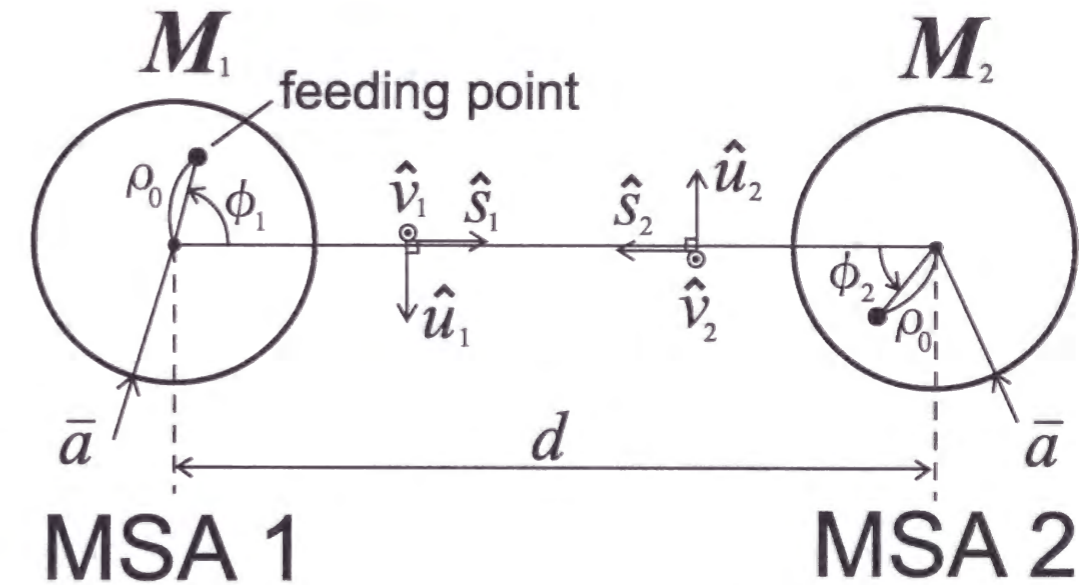

Figure 6.4: MSAs on a ground plane.
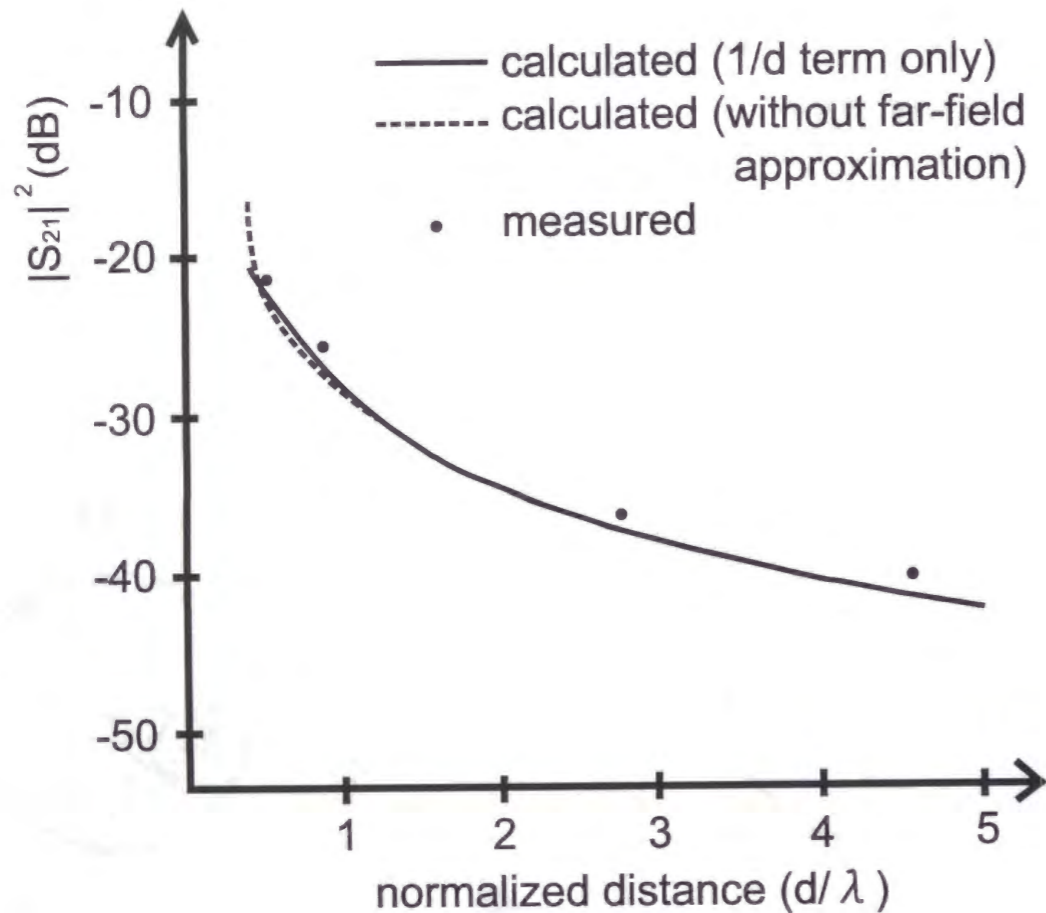
Figure 6.5: Comparison between calculated and measured values of the mutual coupling between MSAs (E-plane and E-plane coupling) on a ground plane.

6.5.2 MSAs on a polyhedron structure

For the second application, we treat the case that the MSAs are placed on a polyhedron structure where multiple wedge diffractions are dominant. The simplest case of the coupling is shown in Fig.6.6, where the polyhedron is expanded on a plane surface and the corresponding GTD ray tracing results in the geodesic between MSAs 1 and 2. Y_{21} is obtained by modifying (6.52) to the multiple diffraction case with the following result:

$$Y_{21} \simeq -\frac{\eta}{V_1 V_2} \boldsymbol{h}_2^M \cdot \bar{G} \cdot \boldsymbol{h}_1^M, \tag{6.60}$$

$$\bar{G} = \frac{-k}{4\pi j} \exp(-jk \sum_{s=1}^{n+1} d_s) \left\{ (\prod_{l=1}^{n+1} d_l)(\sum_{m=1}^{n+1} d_m) \right\}^{-1/2} \left\{ \frac{1}{2^{n-1}} \prod_{t=1}^{n} D_h^{(t)} \right\} \hat{\beta}_{n+1} \hat{\beta}_1. \tag{6.61}$$

In the above formula, the factor $1/2^{n-1}$ is introduced to correct the diffraction coefficients $D_h^{(t)}$, $t \in \{2, 3, ..., n\}$ for the t-th wedge diffraction where contributions of image sources are absent. It is noted from (6.49) that D_s is identically zero when the MSAs are placed on the surface of the polyhedron. If we choose the ray coordinate of MSAs as $\hat{u}_1 = \hat{\beta}_1$ and $\hat{u}_2 = \hat{\beta}_{n+1}$, then we have Y_{21} as follows:

$$Y_{21} \simeq \left\{ \frac{J_1(k_{11}\bar{a})}{J_1(k_{11}\rho_0)} \right\}^2 \frac{k}{4\pi \eta j} \exp(-jk \sum_{s=1}^{n+1} d_s) \left\{ (\prod_{l=1}^{n+1} d_l)(\sum_{m=1}^{n+1} d_m) \right\}^{-1/2} \left\{ \frac{1}{2^{n-1}} \prod_{t=1}^{n} D_h^{(t)} \right\}$$
$$\cdot (\pi \bar{a})^2 \{ J_0(k\bar{a}) - J_2(k\bar{a}) \}^2 \cos \phi_1 \cdot \cos \phi_2. \tag{6.62}$$

In the case of $n = 1$, the above formula correctly recovers the first term of (5.30) in Chapter 5 where the second order approximation is employed. Contributions due to the other multiple diffractions can be treated in the same way by GTD ray tracing, and the results have the same form as (6.62) except for the distances and diffraction coefficients being replaced by the corresponding values. Figure 6.7 shows a comparison between the calculated and measured values between the MSAs separated by a wedge with E-plane and E-plane coupling, where the contributions due to the multiple diffractions are negligible because the other edges of the scatterer are well distant (more than 20λ) form the MSAs.

The parameters of the MSAs are identical with those in the previous subsection. The experiment has been carried out in an anechoic chamber with S-parameter measurements by a network analyzer. A linear amplifier has been inserted to enlarge the dynamic range of the equipment. This guarantees -90 dB of measurable level to the reference level of $S_{21} = 0$ under the presense of -100 dB of noise floor level. Good agreement supports the theory.

Figure 6.6: MSAs on a polyhedron structure.
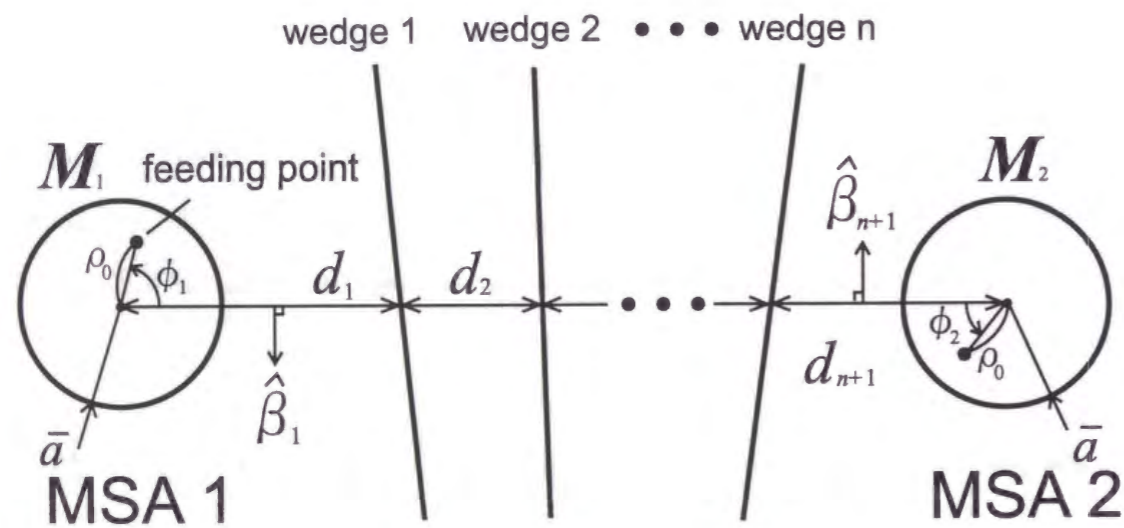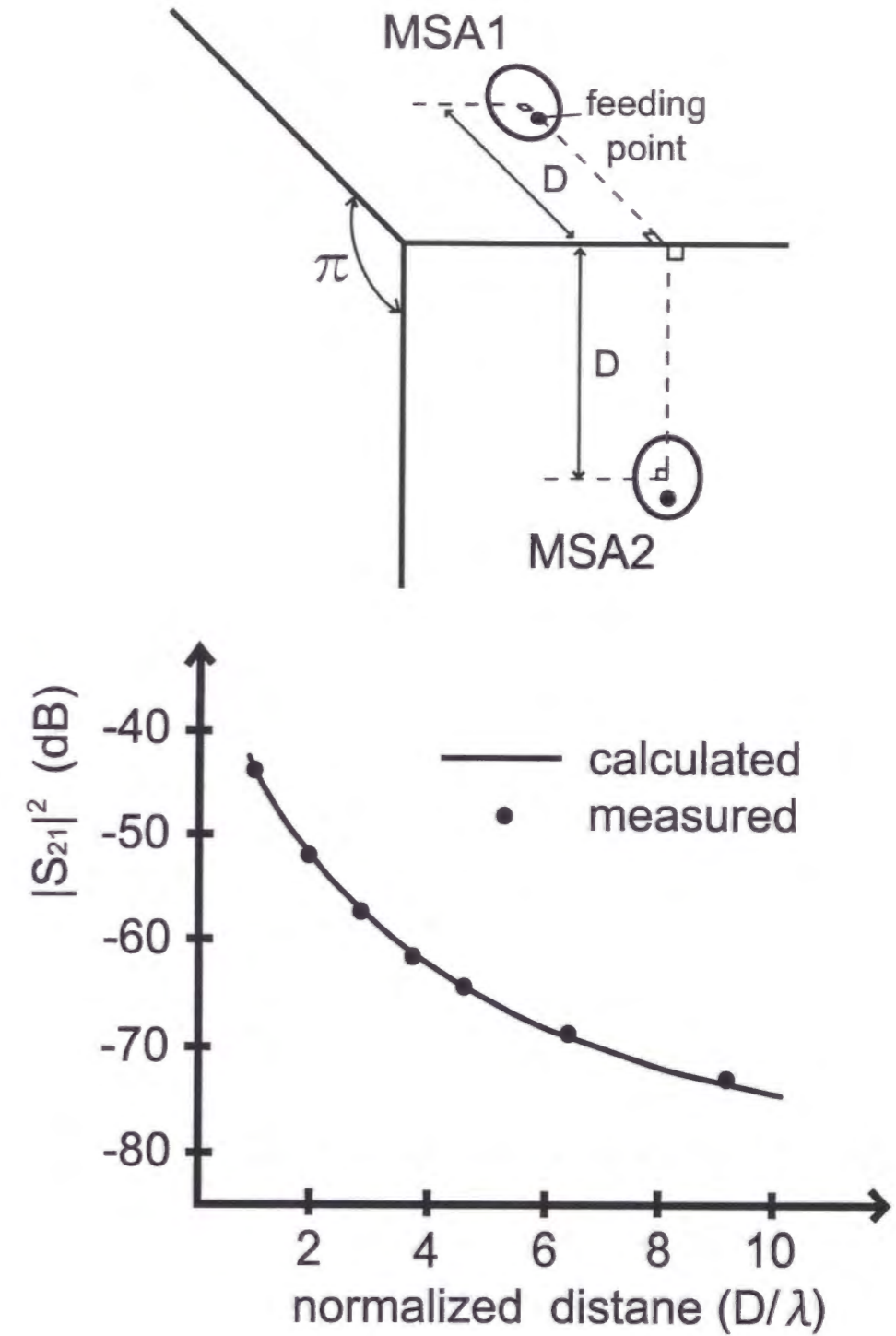

Figure 6.7: Comparison between calculated and measured values between MSAs (E-plane and E-plane coupling) separated by a wedge.

6.6 Summary

A general scheme is investigated for analytical modeling of the mutual coupling between radiating elements in antenna arrays and related problems of antenna farm. Simple expressions of the mutual impedance and admittance are obtained by using far field approximations of the reaction integral between two antennas modeled by given equivalent currents. The expression allows a physical interpretation as a product of radiation patterns multiplied by a propagator of the environment and divided by the voltages or the currents at the feeding points of the two antennas, which gives an approximate first order universal relationship between antennas of arbitrary shape placed in the far field. As the formulas are expressed by local ray coordinates by means of dyadic decomposition of field quantities, physical inspection gives modification of the theory under the presence of high frequency geometries. For a model of antenna coupling on a polyhedron structure, the theory is extended to the case of multiple diffraction due to wedges, where GTD is used for the expression of the diffracted fields. For the application of the theory, two cases of MSAs on a ground plane and on a polyhedron structure are given. The theory correctly recovers the results of Chapter 5 by the first order approximation. Good correspondence between calculated and measured values supports the theory.

The theory is adequately applicable to the analysis of mutual couplings between largely separated radiating elements in antenna arrays and related problems of antenna farm.

Chapter 7

Conclusions

This study is devoted to implementation of efficient design procedures in practical applications of antenna arrays by using analytical modeling of the hardware. Throughout the study, the analytical modeling of hardware is investigated for the radiating element, the feeding structure, the mutual coupling between the radiating elements, and the farm scattering. In the following, summary and conclusion of each chapter are given.

In Chapter 2, a design procedure is developed for a newly proposed collinear antenna array called the electromagnetically coupled coaxial dipole array antenna. The antenna has an advantage of structural simplicity suitable for manufacturing due to a novel use of an electromagnetically coupled feed. Primary effort has been made for the analytical modeling of the radiating element. First, to model the edge of the radiating element, Wiener-Hopf analysis is carried out for the TEM mode reflection coefficient of a coaxial cable which has a semi-infinite outer conductor. A simple closed form formula is obtained with good accuracy. Second, the formula is utilized to calculate the input admittance of the radiating element, where the multiple reflections from the edges are taken into consideration. The dominant term of the input admittance allows physical insight in the scheme of the equivalent circuit. Third, an analysis of radiation pattern of radiating element is carried out with an alternative integral equation formalism. Fourth, as a

model of the array antenna including feeding structure, an equivalent circuit is introduced as serial connection of the self impedances of the radiating elements. A procedure for matching is introduced with the modeling of the matching section. Finally, fabrication and measurement of a prototype array antenna support the design procedure.

In Chapter 3, implementation of analytical modeling is investigated for parallel plate region with an application to the circular iris. First, by using modal expansions with respect to cylindrical harmonics, a variational expression of the equivalent susceptance is obtained for the equivalent circuit of the dominant TEM mode. The expression is stationary with respect to the first order variation of the electric field on the surface of the circular iris. A simple approximate closed form formula is obtained for the equivalent susceptance. The effect of the curvature of the circular iris is contained in a correction factor for the previously known formula for the linear iris. If the radius of the curvature is very large compared with the operating wavelength, the correction factor goes to unity, which recovers the result of the linear iris. Second, numerical solution is constructed by using an exact integral equation formalism. Finally, verification of the approximate formula is given by comparing its values with those of the numerical solution. The content gives a typical example for analytical modeling of the feeding structure of antenna arrays, where accurate modeling is achieved through the use of circuit parameters based on solutions of the boundary value problem.

In Chapter 4, a design procedure is developed for a newly proposed planar antenna array, the radial line planar monopulse antenna. The antenna is highly efficient because of a waveguide feed, and is capable of synthesizing monopulse patterns. First, by using the EMF method, an analysis of the mutual coupling between probes in the radial line is carried out with the result of simple closed form expressions. Second, the mechanism of monopulse pattern synthesis is made clear through modal expansions in the radial line. third, simple design procedures are developed for the uniform aperture field distribution

by using algebraic relations obtained between the parameters, where the perfect antenna efficiency can be obtained by means of the standing wave feed. Finally, fabrication and measurement of a prototype antenna support the design procedure. This chapter gives a typical example of the analytical modeling of the feeding structure of antenna arrays.

In Chapter 5, an analysis is carried out for antenna coupling between arrays on a polyhedron structure. First, to compute efficiently a large number of pairs of the radiating elements, an approximate formula is developed for the mutual admittance between circular MSAs separated by a wedge, where GTD is used for the expression of the diffracted field. Approximate analytical evaluation of the mutual admittance integral is achieved with a simple closed form expression of the mutual admittance between the MSAs. Second, experimental verification of the theory is given. Finally, through several numerical simulations supported by the formula, it is concluded that sidelobe level of the antenna array in the direction of the wedge gives significant contribution to the coupling. Therefore, null beam forming or low sidelobe operation in that direction is applicable to obtaining good isolation characteristics. With the procedure, the effect of antenna farm can be calculated effectively.

In Chapter 6, a general scheme is investigated for analytical modeling of the mutual coupling between radiating elements in antenna arrays and related problems of antenna farm. First, simple expressions of the mutual impedance and admittance are obtained by using far field approximations of the reaction integral between two antennas modeled by given equivalent currents. The expression allows a physical interpretation as a product of radiation patterns multiplied by a propagator of the environment and divided by the voltages or the currents at the feeding points of the two antennas. This gives an approximate first order universal relationship between antennas of arbitrary shape placed in the far field. Second, extension of the theory is readily achieved for high frequency geometries by physical insight. As a model of antenna coupling on a polyhedron structure, antenna

couplings due to multiple diffracted fields by wedges are treated by using GTD. Finally, two cases of MSAs on a ground plane and on a polyhedron structure are given for the application, where the theory correctly recovers the results in Chapter 5 by the first order approximation. Good correspondence between calculated and measured values supports the theory. The theory is adequately applicable to the analysis of mutual couplings between largely separated radiating elements in antenna arrays and related problems of the farm scattering.

The hardware and methods developed in the present study are considered to have wide applicability for communications and radar systems. The electromagnetically coupled coaxial antennas is applicable to basestation for mobile communication systems which require omnidirectional antennas. Thanks to the advantage in manufacturing and simple design procedure developed in the present study, future applications are also expected to other systems such as boundary layer radars. The radial line planar antenna is capable of supporting monopulse tracking operation with the highly efficient feeding structure. The feature is suited for its application to mobile satellite communication systems. Proposed analysis method for the mutual coupling with its extension to the farm scattering problems is expected to have general applications to practical systems due to its capability of efficient computation.

Implementation of the efficient design procedure requires selection of dominant parameters and optimal determination of their values. Good amount of physical insight is needed at every stage of the design. The analytical modeling can sublimate the hardware into mathematical formulas. The resultant relation shall be of a simple form which well describes the physical phenomena. It is hoped that the methodology shall survive decades regardless of trends in the antenna engineering.

Bibliography

[1] R.C. Hansen, Ed., *Microwave Scanning Antennas,* , Vol. I to III, Academic Press, New York, 1966.

[2] R. F. Harrington, *Time-Harmonic Electromagnetic Fields,* McGraw-Hill, Inc., New York, NY, 1961.

[3] R.E. Collin, *Field Theory of Guided Waves, 2nd Ed.,* IEEE Press, Piscataway, NJ, 1991.

[4] H. Uchida and Y. Mushiake, *VHF-Antenna,* Corona-sha, Inc., Tokyo, 1955.

[5] C. A. Balanis, *Antenna Theory, Analysis and Design,* Harper & Row, Publishers, Inc., New York, 1982.

[6] Y.T. Lo, D. Solomon and W.F. Richards, " Theory and Experiments on Microstrip Antennas," IEEE Trans. Antennas and Propagat., Vol. AP-27, pp. 137-145, 1979.

[7] I. J. Bahl and P. Bhartia, *Microstrip Antennas,* Artech House, Inc., Dedham, MA, 1980,

[8] R.J. Mailloux, " Phased Array Theory and Technology," Proc. IEEE, Vol. 70, No. 3, pp. 246-291, 1982.

[9] R.E. Collin, *Foundations for Microwave Engineering, 2nd Ed.,* McGraw-Hill, Inc., New York, 1992.

[10] R.E. Collin and F.J. Zucker, Ed., *Antenna Theory part1 and 2,* McGraw-Hill, Inc., New York, 1969.

[11] R. Courant and D. Hilbert, *Methods of Mathematical Physics,* Vol. 1 and 2, Wiley, New York, 1989.

[12] N. Amitay, V. Galindo and C.P. Wu, *Theory and Analysis of Phased Array Antennas,* Wiley-Interscience, New York, 1972.

[13] L. Stark, " Radiation Impedance of a Dipole in an Infinite Planar Phased Array," Radio Sci., Vol. 1, pp. 361-377, 1966.

[14] G.L. James, *Geometrical Theory of Diffraction for Electromagnetic Waves,* Peter Peregrinus Ltd., Southgate House, England, 1976.

[15] R.C. Hansen, Ed., *Geometric Theory of Diffraction,* IEEE Press, New York, 1981.

[16] J.J. Bowman, T.B.A. Senior and P.L.E. Uslenghi, Ed., *Electromagnetic and Acoustic Scattering by Simple Shapes,* North-Holland Publ., Amsterdam, 1969.

[17] H. Miyashita, H. Ohmine, K. Nishizawa, S. Makino and S. Urasaki, " Electromagnetically Coupled Coaxial Dipole Array Antenna," IEEE Trans. Antennas Propagat., Vol. 47, No. 11, pp. 1716-1726, Nov. 1999.

[18] H.A. Wheeler, " A vertical antenna made of transposed section of coaxial cable," IRE Conv. Rec., Vol. 4, pt. 1, pp. 160-164, 1956.

[19] T.J. Judasz, W.L. Ecklund and B.B. Balsley, "The coaxial collinear antenna : Current distribution from the cylindrical antenna equation," IEEE Trans. Antennas Propagat., vol. AP-35, pp. 327-331, 1987.

[20] T.J. Judasz and B.B. Balsley, "Improved theoretical and experimental models for the coaxial collinear antenna," IEEE Trans. Antennas Propagat., vol. 37 , pp. 289-296, 1989.

[21] A. Sakitani and S. Egashira, "Analysis of Coaxial Collinear Antenna : Recurrence Formula of Voltages and Admittances at Connections," IEEE Trans. Antennas Propagat., vol. 39, No. 1, pp. 15-20, 1991.

[22] M. Ono, T. Numazaki and M. Mizusawa, "A High-Gain Omnidirectional Antenna Made of a Printed Element," Trans. IECE (Japan), Vol. 63-B, No. 1, pp. 25-31, 1980.

[23] P. Volta, "Design and Development of an Omnidirectional Antenna With a Collinear Array of Slots," Microwave J., Vol. 25, No. 12, pp. 111-115, 1982.

[24] K. Cho, T. Hori, H. Tozawa and S. Kiya, "Bidirectional Collinear Antenna with Arc Parasitic Plates," 1995 IEEE AP-S Intern. Symp. Digt., pp. 1414-1417, 1995.

[25] B. Noble, *Methods Based on the Wiener-Hopf Technique,* Chelsea, New York, 1988.

[26] R. Mittra and S.W. Lee, *Analytical Techniques in the Theory of Guided Waves,* Macmillan, New York, 1971.

[27] K. Kobayashi, " Wiener-Hopf and modified residue calculus techniques," in *Analysis Methods for Electromagnetic Wave Problems,* Chap. 8, E. Yamashita, Ed., Artech House, Boston, 1990.

[28] K. Kobayashi, " The Wiener-Hopf technique with applications to scattering and diffraction problems," in *A Course of Applied Mathematics,* Chap. 9 (in Japanese), K. Horiuchi, Ed., Corona Publishing, Tokyo, 1989.

[29] N. Marcuvitz, *Waveguide Handbook,* Sec. 4-15, pp. 208-213, Peter Peregrinus Ltd., London, 1986.

[30] T.T. Wu, "Input Admittance of Infinitely Long Dipole Antennas Driven from Coaxial Lines, " J. Math. Phys., Vol. 3, No. 6, pp. 1298-1301, 1962.

[31] T.S. Bird, "Exact Solution of open-ended coaxial waveguide with centre conductor of infinite extent and applications, " IEE Proc. Pt. H., Vol. 134, No. 5, pp. 443-448, 1987.

[32] Y.M. Chen and J.B. Keller, "Current on and Input Impedance of a Cylindrical Antenna," J. Res. Nat. Bur. Stand., Vol. 66D, No. 1, pp. 15-21, 1962.

[33] S.W. Lee and R. Mittra, "Admittance of a solid cylindrical antenna," Can. J. Phys., Vol. 47, pp. 1959-1970, 1969.

[34] J.R. Wait, *Electromagnetic radiation from cylindrical structures,* Sec. 4, Peter Peregrinus Ltd., London, 1988.

[35] H. Jasik, Ed., *Antenna Engineering Handbook,* Chap. 9, McGraw-Hill, Inc., New York, 1961.

[36] H. Ohmine, T. Okuno, A. Inage, H. Miyashita and Y. Chatani, "Beamtilt Electromagnetically Coupled Coaxial Dipole Array Antenna," 1995 Comm. Soc. Conv. Rec. IEICE Japan, B-78, 1995 (in Japanese).

[37] H. Ohmine, H. Miyashita and Y. Chatani, "Broadening Bandwidth of Beamtilt Electromagnetically Coupled Coaxial Dipole Array Antenna," 1996 Comm. Soc. Conv. Rec. IEICE Japan, B-77, 1996 (in Japanese).

[38] H. Miyashita, I. Chiba, S. Urasaki and S. Fukao, " Equivalent Susceptance of Circular Iris in a Parallel Plate Waveguide," IEICE Trans. Comm., Vol. E82-B, No. 11, pp. 1844-1850, 1999.

[39] N. Marcuvitz, *Waveguide Handbook,* Peter Peregrinus Ltd., London, 1993.

[40] L. Levin, *Theory of Waveguides, – Techniques for the solution of waveguide problems –,* Newnes-Butterworths, London, 1975.

[41] A.G. Williamson, "Radial-line/coaxial-line junctions: analysis and equivalent circuits," Int. J. Electron., Vol.58, No.1, pp.91-104, 1985.

[42] H. Miyashita and T. Katagi, , " Radial Line Planar Monopulse Antenna," IEEE Trans. Antennas Propagat., Vol. 44, No. 8, pp.1158-1165, Aug. 1996.

[43] F.J. Goebels and K.C. Kelly, , " Arbitrary Polarization from Annular Slot Planar Antennas," IEEE Trans. Antennas Propagat., Vol. AP-9, pp.342-349, July 1961.

[44] N. Goto and M. Yamamoto," Circularly polarized radial line slot antennas," Tech. Rep. IECE Japan, AP80-57, Aug. 1980 (in Japanese).

[45] M. Ando, K. Sakurai, N. Goto, K. Arimura and Y. Ito, " A Radial line slot antennas for 12GHz band satellite TV reception," IEEE Trans. Antennas Propagat., vol. AP-33, pp. 1347-1353, Dec. 1985.

[46] H. Nakano, H. Takeda, Y. Kitamura, H. Mimaki and J. Yamauchi, "Low-Profile Helical Array Antenna Fed from a Radial Wave guide," IEEE Trans. Antennas Propagat., Vol. 40, No.3, pp.279-284, Mar. 1992.

[47] H. Nakano, S. Okuzawa, K. Ohishi, H. Mimaki and J. Yamauchi," A Curl Antenna," IEEE Trans. Antennas Propagat., Vol. 41, No.11, pp.1570-1575, Nov. 1993.

[48] O. Shibata, S. Saito and M. Haneishi, " Radiation Properties of Microstrip Array Antennas Fed by Radial Line," Trans. IEICE(Japan), Vol.J76-B-II, No.1, pp.20-27, Jan. 1993 (in Japanese).

[49] M. Takahashi, J. Takada, M. Ando and N. Goto, " A Slot Design for Uniform Aperture Field Distribution in Single-Layered Radial Line Slot Antennas," IEEE Trans. Antennas Propagat., vol. 39, No.7, pp.954-959, July 1991.

[50] J. Takada, M. Ando and N. Goto, " A Reflection Canceling Slot Set in a Linearly Polarized Radial Line Slot Antenna," IEEE Trans. Antennas Propagat., Vol.40, No.4, pp.433-438,1992.

[51] J. Takada, M. Takahashi, M. Ando, K. Ito and N. Goto, " The Optimum Aperture Illumination Design in Single-Layered Radial Line Slot Antennas," Proc. 1992 IEICE Fall Conf., B-73, Sept. 1992 (in Japanese).

[52] See for example [41] with references contained.

[53] B. Tomasic and A. Hessel, " Electric and magnetic current sources in the parallel plate waveguide," IEEE Trans. Antennas Propagat., vol.AP-35, pp.1307-1310, Nov.1987.

[54] H. Miyashita, Y. Sunahara, R. Ishii, T. Katagi and T. Hashimoto, "An Analysis of Antenna Coupling Between Arrays on a Polyhedron Structure," IEEE Trans. Antennas Propagat., vol.41, no.9, pp.1242-1248, Sept., 1993.

[55] M.C. Bailey, "Mutual Coupling Between Circular Waveguide-Fed Apertures in a Rectangular Ground Plane," IEEE Trans. Antennas and Propagat. vol.AP-22, pp.597-599, July 1974.

[56] K.C. Gupta and A. Benalla, *Microstrip Antenna Design*, Artech House, Norwood, 1988.

[57] H. Miyashita, K. Hariu, I. Chiba and S. Mano, "Approximate Formula for Mutual Coupling Between Linearly Polarized Circular Microstrip Antennas," 1990 Autum Natl. Conv. Rec. IEICE Japan, B-62, 1990 (in Japanese).

[58] T. Numazaki, S. Mano, T. Katagi and M. Mizusawa "An Improved Thinning Method for Density Tapering of Planer Array Antennas," IEEE Trans. Antennas and Propagat. vol.AP-35, No.9, pp.1066-1070, Sept. 1987.

[59] G.N. Watson, *A Treatise on the Theory of Bessel Functions*, Cambridge Univ. Press, London, 1966.

[60] H. Miyashita, I. Chiba, S. Urasaki and S. Fukao, " Simple Expression of Antenna Coupling by Using a Product of Radiation Patterns," IEICE Trans. Comm., Vol. E82-B, No. 11, pp. 1867-1873, 1999.

[61] H. T. Friis, "A Note on a Simple Transmission Formula," Proc. IRE, vol.34, pp.254-256, May. 1946.

[62] A. T. De Hoop and G. De Jong, "Power Reciprocity in Antenna Theory," Proc. IEE, vol.121, no.10, pp.1051-1056, Oct. 1974.

[63] A. D. Yaghjian, "Efficient Computation of Antenna Coupling and Fields Within the Near-Field Region," IEEE Trans. Antennas Propagat., vol.AP-30, no.1, pp.113-128, Jan. 1982.

[64] V. H. Rumsey, "Reaction Concept in Electromagnetic Theory," Phys. Rev., vol.94, no.6, pp.1483-1491, June 1954.

[65] J. H. Richmond, "A Reaction Theorem and Its Application to Antenna Impedance Calculations," IRE Trans. Antennas Propagat., vol.AP-9, pp.515-520, Nov. 1961.

Publication list

Refereed journals

Chapter 2

1. H. Miyashita, H. Ohmine, K. Nishizawa, S. Makino and S. Urasaki, "Electromagnetically Coupled Coaxial Dipole Array Antenna," IEEE Trans. Antennas Propagat., Vol. 47, No. 11, pp. 1716-1726, Nov. 1999.

Chapter 3

2. H. Miyashita, I. Chiba, S. Urasaki and S. Fukao, "Equivalent Susceptance of Circular Iris in a Parallel Plate Waveguide," IEICE Trans. Comm., Vol. E82-B, No. 11, pp. 1844-1850, 1999.

Chapter 4

3. H. Miyashita and T. Katagi, "Radial Line Planar Monopulse Antenna," IEEE Trans. Antennas Propagat., Vol. 44, No. 8, pp.1158-1165, Aug. 1996.

Chapter 5

4. H. Miyashita, Y. Sunahara, R. Ishii, T. Katagi and T. Hashimoto, "An Analysis of Antenna Coupling Between Arrays on a Polyhedron Structure," IEEE Trans. Antennas Propagat., Vol. 41, No. 9, pp.1242-1248, Sept. 1993.

Chapter 6

5. H. Miyashita, I. Chiba, S. Urasaki and S. Fukao, "Simple Expression of Antenna Coupling by Using a Product of Radiation Patterns," IEICE Trans. Comm., Vol. E82-B, No. 11, pp. 1867-1873, 1999.

Related articles

Chapter 2

1. H. Miyashita, H. Ohmine, Y. Chatani and S. Makino, "Electromagnetically coupled coaxial array antenna," IEICE Technical Report, vol.AP95-33, pp.19-26, July 1995 (in Japanese).

2. H. Miyashita, H. Ohmine, Y. Chatani and S. Makino, "Electromagnetically coupled coaxial dipole array antennas," IEICE Soc. Conf.'95, B-95, 1995 (in Japanese).

3. H. Ohmine, T. Okuno, A. Inage, H. Miyashita and Y. Chatani, "Beamtilt electromagnetically coupled coaxial dipole array antenna," IEICE Soc. Conf.'95, B-78, 1995 (in Japanese).

4. H. Ohmine, H. Miyashita and Y. Chatani, "Broadening bandwidth of beamtilt electromagnetically coupled coaxial dipole array antenna," IEICE Soc. Conf.'96, B-77, 1996 (in Japanese).

5. H. Miyashita and I. Chiba, "Improvement of an approximate formula for the TEM mode reflection coefficient of a semi-infinite coaxial cable," IEICE Technical Report, vol.AP97-63, pp.29-34, July 1997 (in Japanese).

6. K. Nishizawa, H. Miyashita and I. Chiba, "A method of matching input impedance of the electromagnetically coupled coaxial dipole array antenna," IEICE Soc. Conf.'97, B-1-76, 1997 (in Japanese).

7. H. Miyashita and I. Chiba, "Improvement of an approximate formula for TEM mode reflection coefficient of a semi-infinite coaxial cable," IEICE Gen. Conf.'97, B-1-99, 1997 (in Japanese).

8. H. Miyashita and I. Chiba, "Current distribution of the electromagnetically coupled coaxial dipole antenna," IEICE Soc. Conf.'98, B-1-136, 1998 (in Japanese).

Chapter 3

9. H. Miyashita and I. Chiba, "An approximate formula for an equivalent susceptance of a circular iris in a parallel plate waveguide," IEICE Technical Report, vol.AP98-77, pp.19-24, Oct. 1998 (in Japanese).

10. H. Miyashita and I. Chiba, "An approximate formula for equivalent susceptance of a circular iris in a parallel plate waveguide," IEICE Gen. Conf.'98, B-1-64, 1998 (in Japanese).

Chapter 4

11. H. Miyashita, S. Sato and T. Katagi, "An analysis of probes in a parallel plate waveguide by EMF method," Proc. IEICE Fall Conf.'92, B-25, 1992 (in Japanese).

12. H. Miyashita and T. Katagi, "Four-point Fed Radial Line Planar Antenna Array for Monopulse Tracking Operation," 1993 IEEE AP-S International Symp. Digt., pp.136-139, Michigan, Jul. 1993.

13. H. Miyashita and T. Katagi, "A design method of uniform aperture distribution for probe-feed type radial line planar antennas," Proc. IEICE Spring Conf.'93, B-55, 1993 (in Japanese).

14. H. Miyashita, S. Uchino, Y. Tsuda and T. Katagi, "Four-point fed radial line monopulse planar antennas," Proc. IEICE Fall Conf.'93, B-65, 1993 (in Japanese).

15. H. Miyashita and I. Chiba, "An approximate formula for equivalent impedance of a loaded probe in a parallel plate waveguide," IEICE Soc. Conf.'97, B-1-86, 1997 (in Japanese).

Chapter 5

16. H. Miyashita, Y. Sunahara, R. Ishii, I. Chiba and S. Mano, "Analysis of mutual coupling between microstrip antennas separated by a conducting wedge," IEICE Technical Report, vol.AP89-67, pp.23-27, Dec. 1989 (in Japanese).

17. H. Miyashita, Y. Sunahara, R. Ishii, I. Chiba and S. Mano, "An analysis of antenna isolation between arrays on a polyhedron structure," IEICE Technical Report, vol.AP90-62, pp.27-34, Sept. 1990 (in Japanese).

18. H. Miyashita, K. Hariu, I. Chiba and S. Mano, "Approximate formula for mutual coupling between linearly polarized circular microstrip antennas," 1990 Autum Nat. Conv. Rec. IEICE Japan, B-62, 1990 (in Japanese).

19. H. Miyashita, Y. Sunahara, R. Ishii, I. Chiba and T. Katagi, "An analysis of antenna isolation between arrays on a polyhedron structure," 1991 Spring Nat. Conv. Rec. IEICE Japan, B-52, 1991 (in Japanese).

Chapter 6

20. H. Miyashita, I. Chiba, H. Ohmine, Y. Sunahara and S. Mano, "Active-element pattern analysis of linearly polarized circular microstrip antenna arrays," 1989 Autum Nat. Conv. Rec. IEICE Japan, B-23, 1989 (in Japanese).

21. H. Miyashita, I. Chiba and T. Katagi, "approximate formula for mutual coupling between linearly polarized rectangular microstrip antennas," 1991 Autum Nat. Conv. Rec. IEICE Japan, B-29, 1991 (in Japanese).

22. H. Miyashita and M. Matsunaga, "A simple expression of antenna coupling by using a product of radiation patterns," Proc. IEICE Spring Conf.'94, B-110, 1994 (in Japanese).

23. K. Nishizawa, H. Miyashita and I. Chiba, "An analysis of active element pattern in log-periodic dipole antenna array," IEICE Gen. Conf.'97, B-1-100, 1997 (in Japanese).

Other articles

1. H. Ohmine, H. Miyashita, Y. Sunahara, M. Matsunaga and S. Mano, "Circular disk microstrip antenna with parasitic annular ring element," 1989 Spring Natl. Conv. Rec. IEICE Japan, B-78, 1989 (in Japanese).

2. Y. Chatani, Y. Itabashi and H. Miyashita, "Wideband microstrip array antenna with 120 degrees beamwidth," Proc. IEICE Spring Conf'92, B-58, 1992 (in Japanese).

3. K. Hariu, H. Miyashita, S. Sato and T. Katagi, "Estimation for null depth of difference pattern with amplitude and phase errors," Proc. IEICE Spring Conf'93, B-41, 1993 (in Japanese).

4. H. Miyashita and Y. Sunahara, "Electrostatic analysis of parallel lines with a cylindrical dielectric cover," IEICE Technical Report, vol.AP94-37, pp.17-20, Aug. 1994 (in Japanese).

5. H. Miyashita and Y. Sunahara, "On a construction method of dyadic Green's functions for plane-stratified regions," IEICE Technical Report, vol.AP94-57, pp.43-48, Oct. 1994 (in Japanese).

6. H. Miyashita and Y. Sunahara, "An approximate formula for effective dielectric constant of parallel lines with a cylindrical dielectric cover," Proc. IEICE Fall Conf.'94, B-43, 1994 (in Japanese).

7. S. Sato, H. Miyashita, Y. Konishi and T. Katagi, "Reduction of Mutual Coupling in Array Antennas with Parasitic Elements," Proceedings of PIERS 1995, Univ. of Washington, Seattle, 1995.

8. Y. Inasawa, H. Miyashita, and S. Makino, "Far region RCS extrapolation method using Fresnel region RCS," Tech. on EMT, IEE Japan, EMT-95-90, pp.1-10, Dec. 1995 (in Japanese).

9. Y. Inasawa, H. Miyashita and S. Makino, "Far field RCS extrapolation method using cylindrically scanned near field RCS data," IEICE Soc. Conf.'95, C-24, 1995 (in Japanese).

10. H. Miyashita, "A high frequency asymptotic analysis of wave propagation in plane-stratified regions," IEICE Gen. Conf.'95, C-39, 1995 (in Japanese).

11. H. Miyashita, "Path Integrals and Wedge Diffraction," Proceedings of ISAP'96., pp.965-968, Chiba Japan, 1996.

12. Y. Inasawa, H. Miyashita, and S. Makino, "Far-Field RCS Prediction Method Using Cylindrical or Planar Near-Field RCS Data," Proceedings of PIERS 1996, p. 467, Innsbruck, 1996.

13. H. Miyashita, "Path integrals and wedge diffraction," IEICE Gen. Conf.'96, C-5, 1996 (in Japanese).

14. Y. Yamaguchi, H. Miyashita and I. Chiba, "A dyadic Green's function for a rectangular waveguide filled with plane-stratified media," IEICE Soc. Conf.'96, B-164, 1996 (in Japanese).

15. Y. Yamaguchi, H. Miyashita, I. Chiba and S. Egashira, "A general construction method of dyadic Green's functions for plane-stratified media in uniform open or closed waveguide of separable cross-sections," IEICE Trans. B, Vol. J80-B-II,No. 5,pp.406-415, May 1997.

16. Y. Inasawa, H. Miyashita, I. Chiba, S. Makino and S. Urasaki, "Far-Field RCS Prediction Method Using Cylindrical or Planar Near-Field RCS Data," IEICE Trans. Electron., Vol. E80-C, No. 11, pp.1402-1406, Nov. 1997.

17. Y. Yamaguchi, H. Miyashita, I. Chiba and S. Egashira, "A high-frequency asymptotic analysis of electromagnetic wave propagation in plane-stratified media," IEICE Technical Report, vol.AP96-106, pp.1-8, Jan. 1997 (in Japanese).

18. Y. Inasawa, H. Miyashita, I. Chiba, T. Mizuno, M. Ichikawa and H. Saito, "Antenna pattern analysis under the crater on the moon", IEICE Technical Report, vol.AP97-10, pp.1-6, Apr. 1997 (in Japanese).

19. Y. Inasawa, H. Miyashita, I. Chiba, T. Mizuno, M. Ichikawa and H. Saito, "Antenna pattern analysis under the crater on the moon using SBR method," IEICE Gen. Conf.'97, B-1-42, 1997 (in Japanese).

20. T. Araki, M. Takabayashi, I. Naito, N. Miyahara, S. Makino, H. Miyashita and T. Katagi, "Reduction of interference in small angular region using pattern synthesis with two element antennas," IEICE Gen. Conf.'98, B-1-89, 1998 (in Japanese).

Appendix A

Factorization procedure for $L(\alpha)$ in Chapter 2

We decompose $L(\alpha)$ into two functions $L^{(1)}(\alpha)$ and $L^{(2)}(\alpha)$ as follows:

$$
\begin{aligned}
L(\alpha) &= L^{(1)}(\alpha)L^{(2)}(\alpha), \\
L^{(1)}(\alpha) &= I_0(\gamma b)K_0(\gamma a) - K_0(\gamma b)I_0(\gamma a), \\
&= \frac{\pi}{2}\{J_0(\kappa a)N_0(\kappa b) - N_0(\kappa a)J_0(\kappa b)\}, \\
L^{(2)}(\alpha) &= \frac{K_0(\gamma b)}{K_0(\gamma a)},
\end{aligned}
$$

As the integral function $L^{(1)}(\alpha)$ is even with respect to α, the following factorization into the infinite product form is possible [25]-[28]:

$$
\begin{aligned}
L^{(1)}(\alpha) &= L_+^{(1)}(\alpha)L_-^{(1)}(\alpha), \\
L_+^{(1)}(\alpha) &= L_-^{(1)}(-\alpha), \\
&= \{L^{(1)}(0)\}^{1/2}e^{-\chi^{(1)}(\alpha)}\prod_{n=1}^{\infty}\left(1+\frac{\alpha}{\alpha_n}\right)^{-\frac{\alpha(b-a)}{n\pi i}}, \\
\chi^{(1)}(\alpha) &= \frac{\alpha(b-a)}{\pi i}\left[1 - C_e - \ln\left\{\frac{\alpha(b-a)}{\pi i}\right\}\right],
\end{aligned}
$$

where, α_n is a zero point of $L^{(1)}(\alpha)$ in the upper-half α-plane, and it is located at $\alpha_n \sim n\pi i/(b-a)$ as $n \to \infty$. $\chi^{(1)}(\alpha)$ has been determined such that $L_+^{(1)}(\alpha)$ has an algebraic

growth as $|\alpha| \to \infty$ in $|\tau| < k_2$; in this case $L_+^{(1)}(\alpha) \sim \alpha^{-1/2}$. It can be also shown that $L_-^{(1)}(\alpha) \sim \alpha^{-1/2}$.

For $L^{(2)}(\alpha)$, the Bates and Mittra factorization formula for $K_0(\gamma a)$ [26] is applied,

$$K_0(\gamma a) = G(\alpha),$$

$$= G_+(\alpha)G_-(\alpha),$$

$$G_+(\alpha) = \left[\frac{\pi i}{2}H_0^{(1)}(ka)\right]^{1/2}\exp\left\{-\frac{ika}{2} + \frac{ia\gamma}{\pi}\ln\left(\frac{\alpha - \gamma}{k}\right) + q(\alpha, a)\right\},$$

$$q(\alpha, a) = \int_0^\infty f(\omega, \alpha, a)d\omega,$$

$$f(\omega, \alpha, a) = \frac{a}{\pi}\left[1 - \frac{2}{\pi\omega a}\cdot\frac{1}{\{J_0(\omega a)\}^2 + \{N_0(\omega a)\}^2}\right]\ln\left(1 + \frac{\alpha}{\sqrt{k^2 - \omega^2}}\right),$$

$$\sqrt{k^2 - \omega^2} = i\sqrt{\omega^2 - k^2},$$

$$G_+(\alpha) \sim \alpha^{-1/4}\exp\left\{\frac{i\alpha a}{\pi}\ln\left(\frac{2\alpha}{k}\right)\right\}, \qquad (|\sigma| \to \infty, \tau > -k_2).$$

From the above formulas, $L^{(2)}(\alpha)$ is factorized as follows:

$$L^{(2)}(\alpha) = L_+^{(2)}(\alpha)L_-^{(2)}(\alpha),$$

$$L_+^{(2)}(\alpha) = L_-^{(2)}(-\alpha),$$

$$= e^{-\chi^{(2)}(\alpha)}\left[\frac{H_0^{(1)}(kb)}{H_0^{(1)}(ka)}\right]^{1/2}\exp\left\{-\frac{ik(b - a)}{2} + \frac{i\gamma(b - a)}{\pi}\ln\left(\frac{\alpha - \gamma}{k}\right) + \xi(\alpha, a, b)\right\},$$

$$\xi(\alpha, a, b) = q(\alpha, b) - q(\alpha, a),$$

$$\chi^{(2)}(\alpha) = \frac{\alpha(b - a)}{\pi i}\ln\frac{2\alpha}{k},$$

where, $L_+^{(2)}(\alpha) \sim 1$ and $L_-^{(2)}(\alpha) \sim 1$ can be shown in $|\tau| < k_2$ as $|\alpha| \to \infty$.

Now we have $L_-(\alpha) = L_-^{(1)}(\alpha)L_-^{(2)}(\alpha) \sim \alpha^{-1/2}$ and $L_+(\alpha) = L_+^{(1)}(\alpha)L_+^{(2)}(\alpha) \sim \alpha^{-1/2}$, which prove (2.37).

Appendix B

Numerical evaluation of integral $q(k, x)$ in Chapter 2

By replacing integration variable ω with $t = \omega x$ in (2.47), the infinite integral $q(k, x)$ is arranged as follows:

$$q(k, x) = \frac{1}{\pi}\int_0^\infty dt\left[1 - \frac{2}{\pi t}\cdot\frac{1}{\{J_0(t)\}^2 + \{N_0(t)\}^2}\right]\ln\left(1 + \frac{kx}{\sqrt{(kx)^2 - t^2}}\right),$$

$$\equiv q(kx),$$

$$\equiv Q(x/\lambda),$$

where,

$$Q(x) = \frac{1}{\pi}\int_0^\infty dt\left[1 - \frac{2}{\pi t}\cdot\frac{1}{\{J_0(t)\}^2 + \{N_0(t)\}^2}\right]\ln\left(1 + \frac{2\pi x}{\sqrt{(2\pi x)^2 - t^2}}\right).$$

For convenience, we define the integral $I(x)$ as follows:

$$I(x) = q(x)$$

$$= \frac{1}{\pi}\int_0^\infty dt\left[1 - \frac{2}{\pi t}\cdot\frac{1}{\{J_0(t)\}^2 + \{N_0(t)\}^2}\right]\ln\left(1 + \frac{x}{\sqrt{x^2 - t^2}}\right).$$

In the following, numerical evaluation of $I(x)$ is investigated. The integrand has numerical singularities at $t = 0$ and x. The property of convergence is not clear when $t \to \infty$. We

divide the domain of integration as follows:

$$I(x) = \int_0^{\varepsilon_1} + \int_{\varepsilon_1}^K + \int_K^L + \int_L^{x-\varepsilon_2} + \int_{x-\varepsilon_2}^{x+\varepsilon_3} + \int_{x+\varepsilon_3}^M + \int_M^N + \int_N^\infty,$$

$$(0 < \varepsilon_1 < K < L < x - \varepsilon_2 < x < x + \varepsilon_3 < M < N),$$

where the meaning of the division will be understood later. By writing the integrations in the domains $(0, \varepsilon_1), (\varepsilon_1, K), \cdots, (N, \infty)$ as $I_1, I_2, \cdots, I_8$, respectively, numerical evaluations of them are investigated.

(i) Evaluation of I_1

I_1 is approximated as follows:

$$I_1 \simeq \frac{\ln 2}{\pi}\left[\varepsilon_1 - \frac{2}{\pi}\int_0^{\varepsilon_1}\frac{dt}{t}\frac{1}{1+(2/\pi)^2\{C_e + \ln(t/2)\}^2}\right],$$

$$= \frac{\ln 2}{\pi}\left[\varepsilon_1 + \tan^{-1}\left\{\frac{\pi}{2}\cdot\frac{1}{C_e + \ln(\varepsilon_1/2)}\right\}\right],$$

where the following approximations are made:

$$\ln\left(1 + \frac{x}{\sqrt{x^2-t^2}}\right) \simeq \ln 2, \qquad (0 < \varepsilon_1 \ll 1),$$

$$\{J_0(t)\}^2 + \{N_0(t)\}^2 \simeq 1 + \left(\frac{2}{\pi}\right)^2\left(C_e + \ln\frac{t}{2}\right)^2, \qquad (0 < t \ll 1).$$

Note that,

$$\lim_{\varepsilon_1 \to 0} I_1 = 0.$$

(ii) Evaluation of I_2

K shall be selected adequately so as to relax the singular property of the integrand around $t = 0$. In addition, change of integration variable $t = u^n + \varepsilon_1$ improves convergence characteristics with the following form of I_2:

$$I_2 = \frac{n}{\pi}\int_0^{(K-\varepsilon_1)^{1/n}} du\, u^{n-1}\ln\left(1 + \frac{x}{\sqrt{x^2-t^2}}\right)\left[1 - \frac{2}{\pi t}\frac{1}{\{J_0(t)\}^2 + \{N_0(t)\}^2}\right].$$

$$(t = u^n + \varepsilon_1)$$

(iii) Evaluation of I_3

L shall be selected adequately so as to relax the singular property of the integrand around $t = x$. The integral can be evaluated without particular caution in the domain (K, L).

(iv) Evaluation of I_4

I_4 corresponds to integration around the singularity of the integrand at $t = x$. Change of variable analogous to that of I_2 improves the convergence. In this case, we choose $t = x - \varepsilon_2 - u^n$ with the following resultant form of the integral:

$$I_4 = \frac{n}{\pi}\int_0^{(x-L-\varepsilon_2)^{1/n}} du\, u^{n-1}\ln\left(1 + \frac{x}{\sqrt{x^2-t^2}}\right)\left[1 - \frac{2}{\pi t}\frac{1}{\{J_0(t)\}^2 + \{N_0(t)\}^2}\right]$$

$$(t = x - \varepsilon_2 - u^n)$$

(v) Evaluation of I_5

I_5 corresponds to integration along the contour C_x^- in the complex t-plane, where C_x^- is a semicircle which surrounds the branch point $t = x$ in the lower half t-plane. If we choose ε as the radius of the semicircle, *i.e.* $0 < \varepsilon_2 = \varepsilon_3 = \varepsilon \ll 1$, the following formula is obtained:

$$I_5 \simeq \frac{1}{\pi}\left[1 - \frac{2}{\pi x}\frac{1}{\{J_0(x)\}^2 + \{N_0(x)\}^2}\right]A(\varepsilon, x),$$

$$A(\varepsilon, x) = \int_{C_x^-} dt \ln\left(1 + \frac{x}{\sqrt{x^2-t^2}}\right),$$

$$= -i\varepsilon\int_0^\pi d\theta e^{i\theta}\ln\left(1 + \frac{x}{\sqrt{\varepsilon}e^{i(\theta/2)}\sqrt{2x + \varepsilon e^{i\theta}}}\right),$$

From the above formula, the following relation is obtained:

$$|A(\varepsilon, x)| \sim \frac{\pi\varepsilon}{2}\ln\frac{1}{\varepsilon} \to 0, \quad (\varepsilon \to 0).$$

Then we have the following estimate for I_5:

$$|I_5| \sim \left| \left[1 - \frac{2}{\pi x} \frac{1}{\{J_0(x)\}^2 + \{N_0(x)\}^2} \right] \frac{\varepsilon}{2} \ln \frac{1}{\varepsilon} \right| \to 0, \qquad (\varepsilon \to 0).$$

(vi) Evaluation of I_6

Analogous operation applies as those of I_2 and I_4. Change of integration variable to $t = x + \varepsilon_3 + u^n$ gives the following, where M shall be chosen so as to relax the singularity of the integrand at $t = x$:

$$I_6 = \frac{n}{\pi} \int_0^{(M-x-\varepsilon_3)^{1/n}} du\, u^{n-1} \ln \left(1 - \frac{ix}{\sqrt{t^2 - x^2}} \right) \left[1 - \frac{2}{\pi t} \cdot \frac{1}{\{J_0(t)\}^2 + \{N_0(t)\}^2} \right],$$
$$(t = x - \varepsilon_2 - u^n).$$

(vii) Evaluation of I_7

N shall be chosen so as to accommodate the asymptotic estimate of the integrand as described in (viii). The integral can be evaluated without particular caution in the domain (M, N).

(viii) Evaluation of I_8

I_8 is estimated by asymptotic expansions. With the help of the following formula:

$$H_0^{(1)}(t) \sim \sqrt{\frac{2}{\pi t}} e^{i(t - \pi/4)} \left\{ 1 - \frac{i}{8t} + O\left(\frac{1}{t^3}\right) \right\}, \qquad (t \to \infty),$$

parts of the integrand are approximated as follows:

$$\{J_0(t)\}^2 + \{N_0(t)\}^2 = H_0^{(1)}(t) H_0^{(2)}(t),$$
$$\simeq \frac{2}{\pi t} \left\{ 1 + \frac{1}{64t^2} + O\left(\frac{1}{t^3}\right) \right\}, \qquad (t \to \infty),$$
$$\ln \left(1 - \frac{ix}{\sqrt{t^2 - x^2}} \right) \sim -\frac{ix}{t} + O\left\{ \left(\frac{x}{t}\right)^2 \right\}, \qquad (x/t \to 0).$$

From the above formula, I_8 is estimated as follows:

$$I_8 \sim \frac{1}{\pi} \int_N^\infty dt \left\{ \frac{x}{64 i t^3} + O\left(\frac{1}{t^4}\right) \right\}, \qquad (x \ll N \to \infty),$$
$$= \frac{x}{128 \pi i} \cdot \frac{1}{N^2} + O\left(\frac{1}{N^3}\right), \qquad (x \ll N \to \infty).$$

By using the results of (i) to (viii), $I(x)$ can be evaluated with the desired accuracy.

Appendix C

Derivation of (4.9) in Chapter 4

The summation part X of (4.6) is as follows:

$$X = \sum_{n=1}^{\infty} I_0(\gamma_n a_i) K_0(\gamma_n a_i) \frac{\{\cos kl_i - \cos(n\pi l_i/h)\}^2}{\gamma_n^2 \sin^2 kl_i}, \tag{C.1}$$

$$\gamma_n = \sqrt{(n\pi/h)^2 - k^2}.$$

The following approximations are made by using the large argument asymptotic expansions of cylindrical functions:

$$I_0(\gamma_n a_i) K_0(\gamma_n a_i) \sim \frac{h}{2\pi a_i n}, \tag{C.2}$$

$$\gamma_n \sim n\pi/h. \tag{C.3}$$

Substituting (C.2) and (C.3) into (C.1), then X becomes,

$$X \simeq \frac{h^3}{2\pi^3 a_i} \sum_{n=1}^{\infty} \frac{\{\cos kl_i - \cos(n\pi l_i/h)\}^2}{n^3 \sin^2 kl_i}.$$

Straightforward calculations using some identities of the trigonometric functions and the following sum formula [3] give the final expressions in (4.9) and (4.10):

$$\sum_{n=1}^{\infty} \frac{\cos nx}{n^3} = \zeta(3) + \frac{1}{2}x^2 \ln x - \frac{3}{4}x^2 - \frac{1}{288}x^4 - \frac{1}{86400}x^6 + \dots , \qquad (0 \le x \le 2\pi).$$

Appendix D

Table of integrals for Chapter 5

The integrals in Section 5.2 have been carried out by the following formulas [59]:

$$\int_{-\pi}^{\pi} dx \cos x \cdot \cos(x-y) \cdot e^{jz\cos x} = \pi\{J_0(z) - J_2(z)\}\cos y,$$

$$\int_{-\pi}^{\pi} dx \sin x \cdot \cos(x-y) \cdot e^{jz\cos x} = \pi\{J_0(z) + J_2(z)\}\sin y,$$

$$\int_{-\pi}^{\pi} dx \cos^2 x \cdot \cos(x-y) \cdot e^{jz\cos x} = \pi z j \left\{ J_0(z) + \left(1 - \frac{2}{z^2}\right) J_2(z) \right\} \cos y,$$

$$\int_{-\pi}^{\pi} dx \sin^2 x \cdot \cos(x-y) \cdot e^{jz\cos x} = 2\pi j \frac{J_2(z)}{z} \cos y,$$

$$\int_{-\pi}^{\pi} dx \cos x \cdot \sin x \cdot \cos(x-y) \cdot e^{jz\cos x} = 2\pi j \frac{J_2(z)}{z} \sin y,$$

$$\int_{-\pi}^{\pi} dx \cos x \cdot \sin^2 x \cdot \cos(x-y) \cdot e^{jz\cos x} = \pi \left\{ J_0(z) + \left(1 - \frac{6}{z^2}\right) J_2(z) \right\} \cos y.$$